Engineering Journal

Third Quarter 2023 | Volume 60, No. 3

Smarter. Stronger. Steel.

Closure:

123 Design for Local Member Shear at Brace and Diagonal-Member Connections: Full-Height and Chevron Gussets
Rafael Sabelli and Brandt Saxey

129 Component Modeling for Fire Behavior of Shear Tab Connections
James A. Gordon and Erica C. Fischer

155 Application of AISC *Specification* Requirements for Second-Order Analysis and Stability Design
Rafael Sabelli, Allen Adams, and David Landis

175 Construction Cost Premiums for Risk Category IV SMF Buildings
Paul W. Richards and Amy J. McCall

Engineering Journal

American Institute of Steel Construction

Dedicated to the development and improvement of steel construction, through the interchange of ideas, experiences, and data.

Engineering Journal (ISSN 0013-8029) is published quarterly. Published by the American Institute of Steel Construction at 130 E Randolph Street, Suite 2000, Chicago, IL 60601.

Archives: Search at **aisc.org/ej**. Article downloads are free for current members and are available for a nominal fee for non-members.

Closure:

Design for Local Member Shear at Brace and Diagonal-Member Connections: Full-Height and Chevron Gussets

Original Paper by Rafael Sabelli and Brandt Saxey
Discussion by Paul W. Richards
Closure by Rafael Sabelli and Brandt Saxey

INTRODUCTION

The authors would like to thank Dr. Richards for the work he has performed and the light that work has shed on the behavior of these connections. Dr. Richards' analyses inform the understanding of the forces and displacements corresponding to the progression from elastic behavior, to the design limit state, and to the complete shear-yielding mechanism. Additionally, the analyses also explore the inelastic behavior of the beam after the web-yield mechanism is developed, shedding light on the possible behavior of conditions in which the local web shear was not considered in design.

Both the original paper (Sabelli and Saxey, 2021) and the closure (Richards, 2023) address the "concentrated stress method" (CSM) for design of chevron connections (center beam-brace connections in V-braced, inverted-V-braced, and two-story, X-braced frames). The CSM builds on the work of Fortney and Thornton (2015 and 2017) and Hadad and Fortney (2020). The CSM was developed specifically as an alternative to the "uniform stress method" (USM), the term Sabelli and Saxey apply to the Fortney-Thornton model for clarity. Both the USM and CSM are methods of determining local shear demand corresponding to the application of a moment at the member flange; this moment is the result of the brace forces and the eccentricity of the flange from the work point. Similar to panel-zone shear, the force couple delivering this moment creates a shear corresponding to the moment and the moment arm. The USM uses a set moment arm based on the gusset-plate plastic section modulus across a horizontal section at the beam flange, which results in the design strength being limited by the onset of beam shear yielding at the midpoint of the connection region. By contrast, the CSM allows the beam shear yielding to progress outward from the beam midpoint along the connection length such that the stresses at the gusset-flange interface corresponding to the moment are redistributed, concentrating at each end. In the CSM, the design strength is defined by a combination limit state: shear yielding of the beam over the majority of the connection length and inelastic action (gusset yielding, web local yielding, or web crippling) in the remaining regions at each end. The length of those end zones is the minimum required such that a force equal to the beam shear strength can be transferred without exceeding any of the three limit states (gusset yielding, web local yielding, or web crippling). By minimizing the length required to deliver the force couple, the moment arm is increased, and thus, the required shear strength of the beam is reduced for a given set of brace forces, permitting designers to reduce or eliminate the calculated need for web reinforcement.

In practice the CSM has been used to demonstrate that beams in typical V-braced or inverted-V-braced frames generally do not require reinforcement and that beams in two-story, X-braced frames may require modest adjustment to gusset length to avoid the calculated need for reinforcement. While chevron gussets are an important case for application of the method, the CSM is applicable to other cases in which a gusset or bracket is utilized to deliver a moment to the strong axis of a W-shape.

We are encouraged that Dr. Richards' work appears to confirm that the CSM is reliable for the chevron connections studied and that the CSM does not appear to be excessively conservative. As such, it can be considered as a piece with our work in the effort to provide economy as well as reliability for the design of these connections. Additionally, his work provides sufficient basis to refine the model of stress distribution at the gusset-flange interface in order to simplify some of the equations presented in our paper.

This closure explores the implications of adopting a stress distribution inferred from Dr. Richards' discussion

Rafael Sabelli, Senior Principal, Director of Seismic Design, Walter P Moore, San Francisco, Calif. Email: rsabelli@walterpmoore.com (corresponding)

Brandt Saxey, Technical Director, CoreBrace, West Jordan, Utah. Email: brandt.saxey@corebrace.com

Paper No. 2020-01C

and other implications of the work on design of these connections and discusses the implications of his findings for design of chevron connections.

RICHARDS' FINITE ELEMENT ANALYSIS EXAMINATION OF DESIGN EXAMPLE

Dr. Richards analyzed a finite element model (FEM) based on the design example from the original paper, comparing the horizontal force in the lower gusset used in the design example to the value at different stages of the FEM analysis. Direct comparison of analysis to design may be complicated by numerous factors, including the differences between design strength and expected strength. In this case, however, the FEM utilized the specified yield strength rather than expected yield strength and included only 1% strain hardening. The FEM was also configured such that the proportion of story shears (the sum of the horizontal components of the braces) between the levels above and below the chevron connection closely match those used in our design example. Additionally, in the case of the CSM, the behavior is defined by shear yielding of the beam, for which a resistance factor of 1.0 is used. Thus, the forces in the FEM analysis can be compared to those in the design example.

The FEM analysis shows that the CSM has a reasonable level of conservatism. Dr. Richards identifies the formation of the mechanism as corresponding to 815 kips of lateral force 4% over the corresponding value in the design example (782 kips).

Although not presented directly in our paper or noted in Richards' discussion, the lateral force corresponding to the USM indicating shear yield is 456 kips, 74% of the force at which the FEM shows von Mises stress exceeding 50 ksi in a localized region of the beam web (616 kips). This indicates that engineers wishing to avoid any yielding in the connection region under design loads may utilize the USM conservatively, with significant margin.

STRESS DISTRIBUTION INFERRED FROM FINITE ELEMENT ANALYSIS

While Dr. Richards' finite element analyses generally validate the CSM design method, the stress distributions apparent in his analyses differ slightly from that assumed in the original paper [Figure 15 in Sabelli and Saxey (2021)]. Dr. Richards observes that the shear between the gusset and the flange appears essentially to be confined to the center region of the gusset, shear stresses in the end regions being low and in the opposite direction (Figure 8 in the Richards discussion). That is, the shear appears to be transferred between the regions we identified as the "z" regions (the end regions of the gusset that transfer moment by means of a force couple), and it appears that the force transferred between the gusset and beam in the z regions essentially corresponds to normal stress. The CSM as presented in Sabelli and Saxey (2021), by contrast, assumes the shear is uniform along the entire gusset length. It is worth noting that the z regions posited in the CSM are evident in the Richards analyses (Figure 9 of the Richards discussion). While it is not possible to determine a precise length of these regions from the FEM analysis, the larger-than-design lateral forces resisted suggest that an effective moment arm larger than assumed in design, and thus that the stresses are more concentrated.

Based on these observations, the CSM stress distribution can be adjusted to simplify the design method. Figure 1 shows the stress distribution assumed in our paper (CSM1, adapted from Figure 15 in Sabelli and Saxey) alongside a modified stress distribution inferred from Figure 8 in the Richards discussion (CSM2). The subscript "1" indicates that the quantities are with respect to gusset 1, the lower gusset. (Sabelli and Saxey present a method of apportioning the available beam shear strength in two-story, X-braced frames such that each gusset can be designed independently.) The figure shows forces $F_{1,1}$ and $F_{1,2}$ acting on gusset 1; the gusset length (L_{g1}) and z region lengths (z_1) are also shown. The difference in the z region lengths between CSM1 and CSM2 is exaggerated for clarity.

The CSM2 stress distribution suggests refinement of certain aspects of the design method developed using the CSM1. Nevertheless, either stress distribution, CSM1 or CSM2, may be employed in the CSM method, with only modest differences in the calculated design strength.

Using the CSM2 model, the minimum length of the z region (based on the limit state of gusset yielding) is the length required to deliver a normal force equal to the effective beam shear strength:

$$z_1 \geq \frac{V_{ef1}}{\phi_t F_y t_{g1}} \tag{1}$$

where

F_y = specified minimum yield stress, ksi (MPa)
V_{ef1} = effective member shear strength, kips (N)
t_{g1} = gusset thickness, in. (mm)
z_1 = length of concentrated stress region at ends of gusset, in. (mm)
ϕ_t = resistance factor for tension (0.90)

The equations in Sabelli and Saxey (2021) that are different for CSM2 from the original equation using CSM1 are presented in an Appendix to this closure.

CSM2 STRESS DISTRIBUTION: EXAMINATION OF DESIGN EXAMPLE

To assess the implications of the refinements suggested by Dr. Richards' work, the modified equations in this discussion based on the CSM2 model are applied to the design example. [The reader is referred to the original paper (Sabelli and Saxey, 2021) for a complete description of the condition and for determination of values shown.] Values are compared to those in Sabelli and Saxey (2021), which were determined using the CSM1 model. Whereas the CSM in Sabelli and Saxey is presented as a design method that can be used to establish the required gusset length and thickness, in this closure, those quantities are given. For comparison to the FEM analysis, equations are developed to determine the lateral force that, given the gusset length and thickness present, results in shear yielding of the beam.

The minimum length of the z region is:

$$z_1 \geq \frac{V_{ef}}{\phi_t F_y t_g} \tag{1}$$
$$= \frac{196 \text{ kips}}{(0.90)(50 \text{ ksi})(0.75 \text{ in.})}$$
$$= 5.81 \text{ in.}$$

A value of 7.31 in. was calculated using the CSM1 model in Sabelli and Saxey. In both cases, this value governs over those corresponding to local web yielding (Equation 40 in Sabelli and Saxey) and local web crippling (Equation 42 in Sabelli and Saxey).

This length z_1 can be used to establish the moment arm for the flexural force couple, and thus the maximum moment that the gusset can deliver corresponding to gusset yielding in the z regions and beam shear yielding in the remainder of the connection length. Equation 26 in Sabelli and Saxey gives the required beam shear strength corresponding to a given moment at the gusset interface; here that equation is adapted to solve for the interface moment:

$$M_{f1} = V_{ef}(L_{g1} - z_1)$$
$$= (196 \text{ kips})\left[(56 \text{ in.}) - (5.81 \text{ in.})\right]$$
$$= 9{,}840 \text{ kip-in.}$$

where

L_{g1} = gusset length, in. (mm)
M_{f1} = moment at gusset-to-flange-interface due to brace forces, kip-in. (N-mm)

The lateral force corresponding to this moment is determined using the eccentricity of the gusset-to-flange interface to the beam centerline, adapting Equation 7 in Sabelli and Saxey (with the total moment on the gusset interface in the case of chevron beams being M_{f1}):

$$M_{f1} = \frac{F_{V1} d_m}{2} \tag{2}$$

where

F_{V1} = gusset shear component parallel to member axis at interface with flange, kips (N)
d_m = member depth, in. (mm)

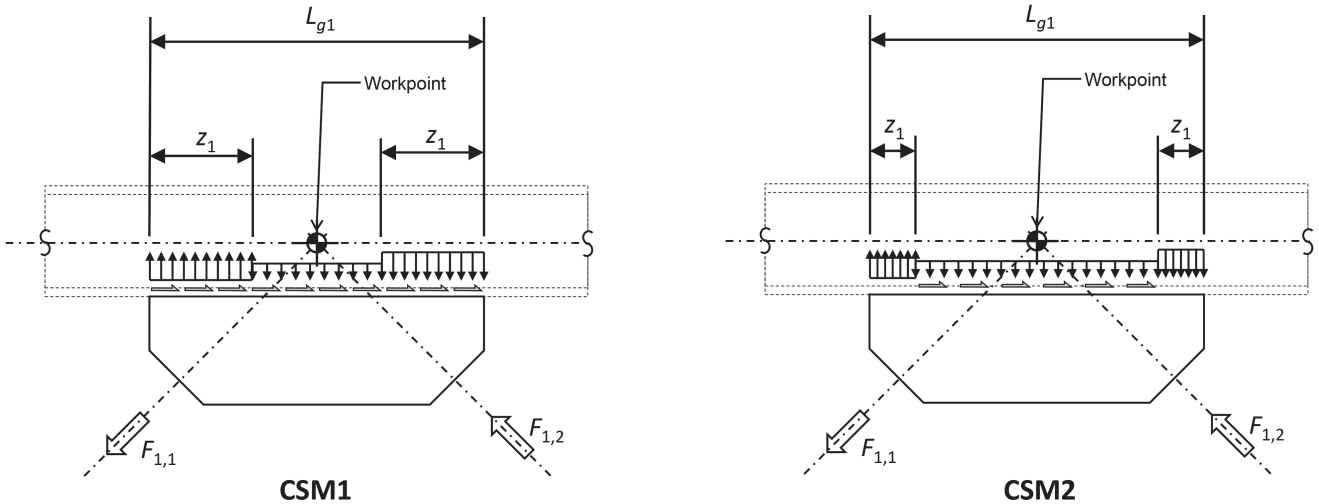

Fig. 1. CSM1 and CSM2 stress distributions.

Thus

$$F_{V1} = \frac{2M_{f1}}{d_m}$$
$$= \frac{2(9{,}840 \text{ kip-in.})}{24.3 \text{ in.}}$$
$$= 810 \text{ kips}$$

The corresponding value using CSM1 is 782 kips. The CSM2 value is closer to the mechanism-formation value identified by Dr. Richards, with only 1% conservatism rather than 4% using CSM1. Recognizing that the determination of the condition that represents the limit state is somewhat arbitrary, the CSM2 does not represent a significant increase in accuracy in the connection design strength. The modified equation for z-region length (Equation 1), however, is simpler than the original method and provides for a better understanding of the local behavior.

For completeness, the gusset should be checked for both the combined shear and normal forces in the center region between z regions, and for the combined normal, shear, and flexural forces on a critical section (Figure 19 in Sabelli and Saxey). For brevity, these calculations are not presented here. However, the authors note that, in both cases, the demand-to-capacity ratios calculated using CSM2 are slightly lower than those determined using CSM1.

APPLICATION

Dr. Richards' FEM analyses specifically address the behavior of chevron connections in which the local beam shear may exceed the beam shear capacity. Previous work suggests that, if the CSM is used, this condition is largely confined to beams in two-story, X-braced frames. Due to design for axial forces, beams in V-braced and inverted-V-braced frames with typical gusset lengths generally have sufficient shear capacity for shear demand calculated using the CSM. (If the USM is used, it is more likely that beams in such frames will be determined to have insufficient shear capacity.) The FEM analyses specifically examine the behavior of conditions limited by gusset yielding in the z regions. The behavior of conditions limited by web local yielding or web crippling may differ for beam deformations beyond those corresponding to CSM limit state.

Dr. Richards' findings, and the implications for refining the stress distribution model, appear to be applicable across the entire range of the CSM. That is, the authors believe the CSM2 model can be used to determine the design strength for other cases in which a gusset or bracket delivers a moment to the strong axis of a W-shape.

CONCLUSIONS

Dr. Richards' work appears to validate the use of the CSM for establishing the adequacy of chevron connections. Additionally, the analyses inform a refined stress-distribution model that can be used to simplify equations for the design of these connections.

APPENDIX: REVISED CSM DESIGN EQUATIONS BASED ON CSM2 STRESS DISTRIBUTION

To aid the designer employing the CSM, Table A.1 provides the CSM equations that can be modified based on the CSM2 stress distribution shown in Figure 1. Table A.1 shows the original equation (based on the CSM1 model), the revised equation (based on the CSM2 model), and the reference equation number from Sabelli and Saxey (2021). Refer to Sabelli and Saxey for the definition of symbols.

REFERENCES

Fortney, P.J. and Thornton, W.A. (2015), "The Chevron Effect—Not an Isolated Problem," *Engineering Journal*, AISC, Vol. 52, No. 2, pp. 125–164.

Fortney, P.J. and Thornton, W.A. (2017), "The Chevron Effect and Analysis of Chevron Beams—A Paradigm Shift," *Engineering Journal*, AISC, Vol. 54, No. 4, pp. 263–296.

Hadad, A.A. and Fortney, P.J. (2020), "Investigation on the Performance of a Mathematical Model to Analyze Concentrically Braced Frame Beams with V-Type Bracing Configurations," *Engineering Journal*, AISC, Vol. 57, No. 2, pp. 91–108.

Richards, P.W. (2023), "Discussion: Design for Local Member Shear at Brace and Diagonal-Member Connections: Full-Height and Chevron Gussets," *Engineering Journal*, AISC, Vol. 60, No. 2, pp. 61–71.

Sabelli, R. and Saxey, B., (2021), "Design for Local Member Shear at Brace Connections: Full-Height and Chevron Gussets," *Engineering Journal*, AISC, Vol. 58, No. 1, pp. 45–78.

Table A.1. Modified Equations Utilizing CSM2 Stress Distribution			
Quantity	**Equation Number**	**Original Equation (Based on the CSM1 Model)**	**Modified Equation (Based on the CSM2 Model)**
Minimum gusset thickness based on stress in *z* region	35	$t_{g1} \geq \sqrt{\left(\frac{F_{V1}}{\phi_v 0.6 F_y L_{g1}}\right)^2 + \left(\frac{R_{z1}}{\phi_t F_y (L_{g1} - e_{z1})}\right)^2}$	$t_{g1} \geq \frac{R_{z1}}{\phi_t F_y (L_{g1} - e_{z1})}$
	36	$t_{g1} \geq \sqrt{\left(\frac{F_{V1}}{\phi_v 0.6 F_y L_{g1}}\right)^2 + \left[\frac{R_{z1}}{\phi_t F_y \left(L_{g1} - \frac{M_{f1}}{R_{z1}}\right)}\right]^2}$	$t_{g1} \geq \frac{R_{z1}}{\phi_t F_y \left(L_{g1} - \frac{M_{f1}}{R_{z1}}\right)}$
Minimum gusset thickness based on stress in center region	37	$t_{g1} \geq \sqrt{\left(\frac{F_{V1}}{\phi_v 0.6 F_y L_{g1}}\right)^2 + \left(\frac{F_{N1}}{\phi_t F_y (L_{g1} - 2z_1)}\right)^2}$	$t_{g1} \geq \frac{\sqrt{\left(\frac{F_{V1}}{\phi_v 0.6}\right)^2 + \left(\frac{F_{N1}}{\phi_t}\right)^2}}{F_y (L_{g1} - 2z_1)}$
	38	$t_{g1} \geq \sqrt{\left(\frac{F_{V1}}{\phi_v 0.6 F_y L_{g1}}\right)^2 + \left[\frac{F_{N1}}{\phi_t F_y \left(\frac{2M_{f1}}{R_{z1}} - L_{g1}\right)}\right]^2}$	$t_{g1} \geq \frac{\sqrt{\left(\frac{F_{V1}}{\phi_v 0.6}\right)^2 + \left(\frac{F_{N1}}{\phi_t}\right)^2}}{F_y \left(\frac{2M_{f1}}{R_{z1}} - L_{g1}\right)}$
Minimum gusset length based on stress in *z* region	39	$L_{g1} > \frac{M_{f1}}{V_{ef1}} + \frac{V_{ef1}}{t_{g1}\phi_t F_y}$ (approximate)	$L_{g1} \geq \frac{M_{f1}}{V_{ef1}} + \frac{V_{ef1}}{t_{g1}\phi_t F_y}$ (exact)
Minimum *z* region length based on stress in *z* region	41	$z_1 \geq \frac{L_{g1}}{2} - \sqrt{\frac{L_{g1}^2}{4} - \frac{M_{f1}/\phi_t}{\sqrt{(F_y t_g)^2 - \left(\frac{F_{V1}}{\phi_v 0.6 L_{g1}}\right)^2}}}$	$z_1 \geq \frac{L_{g1}}{2} - \sqrt{\frac{L_{g1}^2}{4} - \frac{M_{f1}}{\phi_t F_y t_g}}$
Maximum *z* region length based on stress in center region	45	$z_1 \leq \frac{1}{2}\left[L_{g1} - \frac{F_{N1}/\phi_t F_y t_{g1}}{\sqrt{1 - \left(\frac{F_{V1}}{\phi_v 0.6 F_y t_{g1} L_{g1}}\right)^2}}\right]$	$z_1 \leq \frac{L_{g1}}{2} - \frac{\sqrt{\left(\frac{F_{V1}}{\phi_v 0.6}\right)^2 + \left(\frac{F_{N1}}{\phi_t}\right)^2}}{2F_y t_{g1}}$
Horizontal force in critical region	77	$F_{X\,crit} = \frac{X_{crit}}{L_g} F_V$	$F_{X\,crit} = \frac{X_{crit} - z}{L_g - 2z} F_V$

Component Modeling for Fire Behavior of Shear Tab Connections

James A. Gordon and Erica C. Fischer

ABSTRACT

During a building fire scenario, the behavior and capacity of gravity connections can significantly contribute to the integrity of steel-framed building structures. Because gravity connections are subjected to axial and flexural force demands and have a limited rotational capacity due to large beam rotations during a fire scenario, a connection model is needed to simulate their behavior when using analytical models to simulate the behavior of a steel structure in fire. This study develops a component model for shear tab connections at ambient and elevated temperatures in the opensource finite element program, OpenSees, to further enable the use of OpenSees for simulating steel structures in fire, although the developed component model is not limited to implementation within OpenSees. The developed component model is benchmarked against experimental tests of isolated connections and a structural assembly with shear tab connections subjected to mechanical and thermal loads. Through benchmarking, it is shown that (1) the developed component model could be used to simulate connection behavior during a fire scenario and (2) simulating the ductility of connections and connecting components due to damage is critical when simulating the behavior of shear tab connections exposed to fire.

Keywords: component model, connections, OpenSees, steel structures in fire.

INTRODUCTION

Previous research and building fires have demonstrated the critical role of gravity connections in the stability of steel-frame structures during a fire. Gravity frame connections are susceptible to failure during a fire due to the effects of elevated temperatures, fire-induced load demands, or a combination of the two. Because floor beams provide bracing to gravity columns, the failure of beam-to-column connections can lead to column buckling during a fire, which in turn can lead to the partial or full collapse of a building.

During a fire, the increasing temperatures of structural steel components lead to the reduction of material strength and stiffness and imposed forces and deformations due to thermal expansion (Figure 1) (Burgess et al., 2012; Liu et al., 2002; Liu et al., 2019). Structural steel mechanical properties (strength and stiffness) degrade with increasing temperatures. In addition, as structural steel floor beams are heated, the thermal expansion coefficient increases (CEN, 2005a). Heated steel structural components of a building are also restrained by the surrounding cooler structure. This restraint imposes thermal deformations and axial forces in the beams (Burgess et al., 2012; Liu et al., 2002). Subsequently, the restraint will impose flexural and axial force demands in the connections (Liu et al., 2019). However, gravity connections are typically only designed for shear forces at ambient temperatures. Therefore, simulations that exclude the ability to quantify the flexural and axial force demands can underestimate the demands imposed on beams and connections throughout a fire.

Figure 1 shows the fire behavior of typical gravity connections. When gravity connections are operating at service conditions, the only significant load demands on the connection are shear forces due to gravity loading of the beams [Figure 1(a)]. During a fire, the beam expands due to thermal elongation/expansion. Thermal expansion of the beam is resisted by the surrounding structural elements, and compressive axial force develops in the connections [Figure 1(b)]. It is important to note that thermal elongation in the beam and the development of compressive axial forces in gravity connections typically occur at temperatures less than 750°F, before the mechanical properties of steel begin to degrade substantially (Burgess et al., 2012). When temperatures of the steel components exceed 750°F, the material properties (elastic modulus, Yield stress, and the proportional limit) begin to decrease. As shown in Figure 1(c), when the strength and stiffness of the beam are reduced by elevated temperatures, the beam may have large deflections and end rotations. Rotation of the beam ends can cause the bottom flange of the beam to have contact with the flange of the column it is connected to. Contact of the bottom beam flange and the column flange limits the rotational capacity of the connection, imposing large flexural

James A. Gordon, Graduate Research Assistant, School of Civil and Construction Engineering, Oregon State University, Corvallis, Ore. Email: j9882gordon@gmail.com

Erica C. Fischer, John and Jean Loosley Faculty Fellow, School of Civil and Construction Engineering, Oregon State University, Corvallis, Ore. Email: erica.fischer@oregonstate.edu (corresponding)

Paper No. 2022-06R

demands on the connection and increasing compressive forces in the beam (Hajjar et al., 2019). At this point during the fire, the gravity connection designed for only shear force demand does not behave as an idealized pin. As the gas temperatures in the compartment decrease in the cooling phase of the fire, the temperatures of the steel components also decrease, and axial tension demands develop in the connections [Figure 1(d)]. Due to these behaviors, gravity connections can be subjected to axial force (compressive and tensile), shear force, and flexural demands during a fire and allow only limited rotation of the beam ends.

This research focused on simulating the behavior of shear tab connections during a fire using a component model in OpenSees (Mazzoni et al., 2006). Specifically, the goal of this study was to develop a component model for shear tab connections at ambient and elevated temperatures through (1) reviewing previous literature on the development of component models for shear tab connections and comparing and discussing previously developed component models for the application of simulating shear tab connections subjected to fire scenarios; (2) identifying appropriate component models to use to simulate shear tab connection behavior in fire and develop the component models within the open-sourced FE program, OpenSees; and (3) benchmarking the developed component models at ambient and elevated temperatures against experimental data. While these objectives are accomplished through the use of the FE program, OpenSees, the results of this research can be applied to other FE programs.

BACKGROUND ON USING COMPONENT MODELS TO SIMULATE SHEAR TAB CONNECTIONS

General Overview of Previous Work

Rex and Easterling (2003) developed an analytical method that could approximate the force-deformation (F-δ) behavior of bolt bearing at ambient temperature based on experimental data and finite element (FE) models. However, the empirical parameters used by Rex and Easterling are only applicable at ambient temperatures; therefore, their component model was not directly evaluated in this study.

Sarraj (2007) further developed the work of Rex and Easterling (2003), resulting in a component model for shear tab connections at elevated temperatures. The bolt bearing component of the Sarraj model used the same analytical expressions for initial stiffness and F-δ behavior as Rex and Easterling but calibrated some of the equation constants to be temperature-dependent variables. The analytical expression and the temperature-dependent variables used

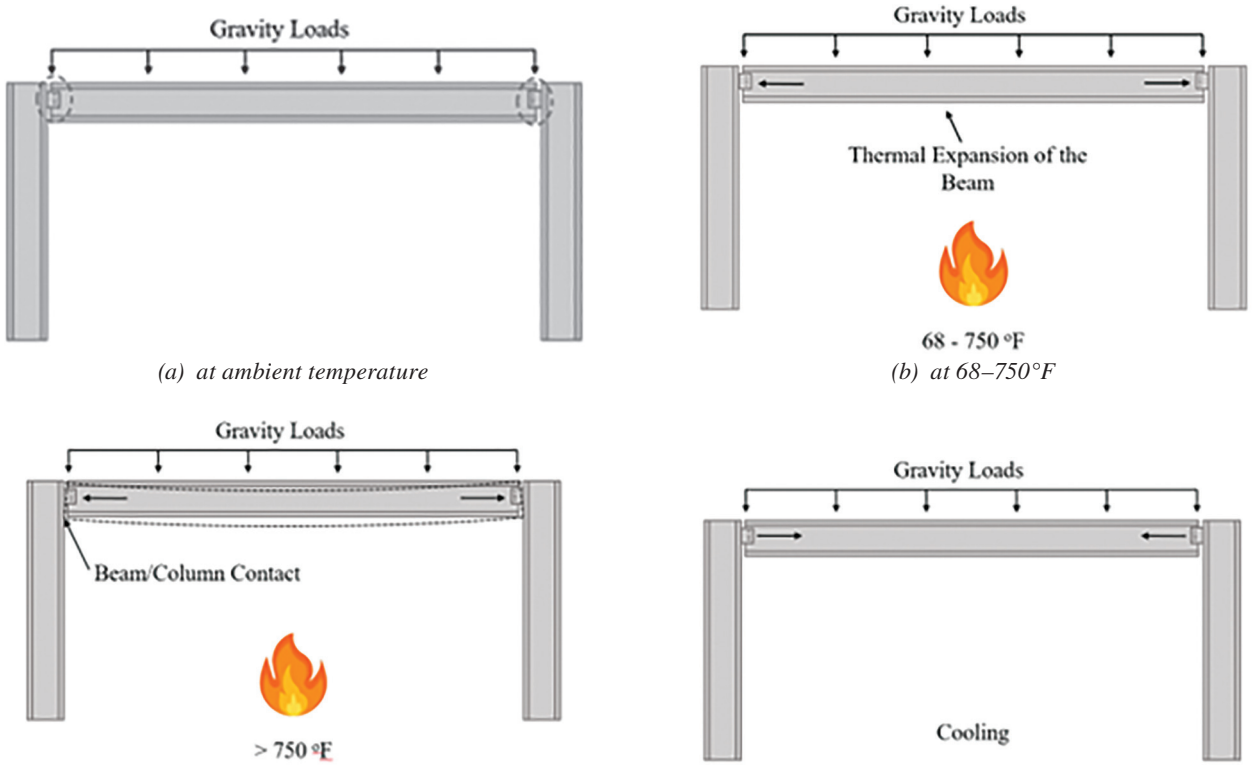

(a) at ambient temperature

(b) at 68–750°F

(c) at a temperature greater than 750°F

(d) cooling from elevated temperatures

Fig. 1. Demands and behavior of gravity connections during a fire scenario.

by Sarraj to approximate bolt shear behavior consisted of a modified Ramberg-Osgood expression that was fitted to data obtained by a series of FE analyses. After assembling the components into a component model within ABAQUS (Smith, 2009), the component model was benchmarked against a detailed FE model and test data from Wald et al. (2006).

Sadek et al. (2008) developed a component model for shear tab connections to simulate a steel beam with a composite metal deck. The component model developed by Sadek et al. (2008) consisted of bolt components and a concrete contact component. The stiffness for the bolt components was derived from the definition of rotational stiffness given by FEMA 355D (2000). While Sadek et al. calculate the limit states of the bolt components based on the observed capacities of the connecting elements, component stiffness is dependent on assumed connection stiffness instead of the observed stiffness of the connecting elements. Because the component model developed by Sadek et al. does not develop F-δ relationships based on observed behavior of the individual connecting elements, it will not be explored further in this study.

The load-deformation response for bolt bearing, bolt shear, and friction developed by Sarraj (2007) were used, validated, or modified by several researchers in subsequent studies. Yu et al. (2009) validated the bolt shear portion of the component model developed by Sarraj against a series of experimental tests. The results of the experiments were used to modify the post-peak behavior of the bolts in shear to simulate the appropriate ductility of bolts in shear at elevated temperatures.

Taib and Burgess (2011) implemented the component F-δ relationships developed by Sarraj (2007) with modified post-peak behavior representing the ductility in bolt shear failure observed by Yu et al. (2009). Taib and Burgess simplified the component F-δ curves into trilinear curves and incorporated nonsymmetrical tension and compression behavior to the bolt bearing component to account for the lack of tearout failure when the bearing components are loaded in compression.

Agarwal and Varma (2014) modified the bolt bearing and bolt shear component definitions developed by Sarraj (2007) to include post-peak behavior and account for component ductility at elevated temperatures. In addition, Agarwal and Varma added a gap element to the component model to account for the axial and rotational stiffness of the connection when the gap between the beam and column closes and the bottom flange of the beam is in bearing against the column. However, the modifications in post-peak behavior made by Agarwal and Varma assumed ductile failure of bolt shear and bolt bearing components to be initiated at a deformation of one-half the bolt diameter, regardless of the temperature. At temperatures less than 750°F, bolt shear fracture has been exhibited as a brittle failure mode.

Koduru and Driver (2014) added vertical spring components representing plate yielding and plate fracture to a component model that combined the bolt shear component developed by Sarraj (2007) and the bolt bearing component developed by Rex and Easterling (2003). In the bearing component developed by Koduru and Driver, the compressive capacity of the component is increased to account for bolt bearing failure instead of edge tearout, and the tensile capacity of the component is governed by the edge tearout. The model developed by Koduru and Driver assumes that ductile failure is initiated when the deformation is equal to half of the edge distance such that the resistance of the bearing component decreases linearly until it has zero resistance at a deformation equal to the end distance. Additionally, Koduru and Driver noted that ignoring bolt slip in the connection resulted in a 67% overestimate of peak tensile force.

Weigand (2017) developed a component model for a single plate shear tab connection with pretensioned bolts at ambient temperature for use under cyclic loading. To incorporate damage during cyclic loading, Weigand included bolt hole damage due to bearing into the component model. Because the connections considered in this study do not have pretensioned bolts, the analytical expressions developed by Weigand for component behavior are not directly compared against the other component constitutive models presented in this study. However, the consideration of bolt hole damage during load reversal is applicable to shear tab connections subjected to fire scenarios.

Weigand et al. (2018) developed a bolt shear component model using experimental testing and analytical models. Analytical models were fit to experimental data using the methodologies described in Peixoto et al. (2017). Because the constitutive model developed by Weigand et al. is highly empirical, it is limited to the range of specimen types and temperatures considered in the experimental investigation performed by Peixoto.

Xie et al. (2018a, 2018b) used detailed FE models to perform a parametric study on bolt bearing and bolt shear components to derive F-δ relationships that considered the effects of different geometric variabilities of connections. From the findings of the parametric FE study on bolt shear behavior, Xie et al. (2018b) developed a modification to the Eurocode 3 (CEN, 2005a) equation for bolt shear capacity and implemented this change into the bolt shear component model. The bolt bearing, bolt shear, and friction components were then combined to create a component model that was validated against the experimental tests performed by Yu et al. (2009).

Hajjar et al. (2019) developed a single analytical expression derived by mathematically combining component stiffnesses to calculate the response of the connection at different "stages" throughout the fire. A component representing the contact between the bottom flange of the beam

and the flange of the column was developed with a stiffness equal to the axial stiffness of the bottom flange of the beam. Because Hajjar et al. considered only a linear stiffness and did not incorporate considerations for component failure, the component definitions for bearing and bolt shear are not compared with other component models presented in this study.

Additional research has been performed to validate the component modeling approach for flexible end-plate connections. Some of the individual components and methodologies used in the flexible end-plate connection models are relevant to shear tab connection models. Silva (2001) proposed an analytical component-based procedure for modeling steel end-plate connections where the F-δ curves of the components are simplified to be bilinear. Silva classified components as either very ductile, moderately ductile, or brittle. Consequently, the post-peak F-δ behavior assigned to the components was based on the ductility category in which they are placed. Hu et al. (2009) developed a component model for flexible end-plate connections that incorporated a component to represent the contribution of a fillet weld in tension to the overall connection behavior. Hu and Engelhardt (2014) and Fischer et al. (2018) performed isolated connection tests to experimentally quantify the F-δ behavior of connections at steady-state temperatures. The tests performed by Hu and Engelhardt included a beam section and shear tab connection, while the tests performed by Fischer et al. used lap spliced joints.

Kurikova et al. (2022) developed a component model for fillet welds to aid in the design of welded joints using a component-based finite element method (CBFEM). Kurikova et al. defined the welds to have a bilinear F-δ and a plastic strain limit of 5% of the effective throat thickness of the weld. Through comparison of the analytical model developed by Kurikova et al. to data from experimentally tested longitudinal and transverse welds, it was shown that a plastic strain limit of 5% of the weld thickness is conservative for design. However, a plastic strain limit may be used to reflect the deformation recorded at weld failure during experimental tests.

Comparison of Component Models Developed

Analytical Models for Bolt-Shear Components

The bolt shear capacity within bolt shear component F-δ models developed by previous researchers is consistent between constitutive models and matches the bolt shear strength per the AISC *Specification* (2016). However, the amount of incorporated ductility varied among the available models (Figure 2) compared using a ¾-in.-diameter ASTM F3125/3125M, Gr. A325 bolt. Sarraj (2007), Weigand et al. (2018), and Xie et al. (2018b) considered the bolt in shear to fail suddenly when the force was equal to the ultimate bolt shear capacity. The models developed by Xie et al. (2018b) and Sarraj reached the ultimate bolt shear capacity before ¼ in. (6 mm) of deformation (approximately

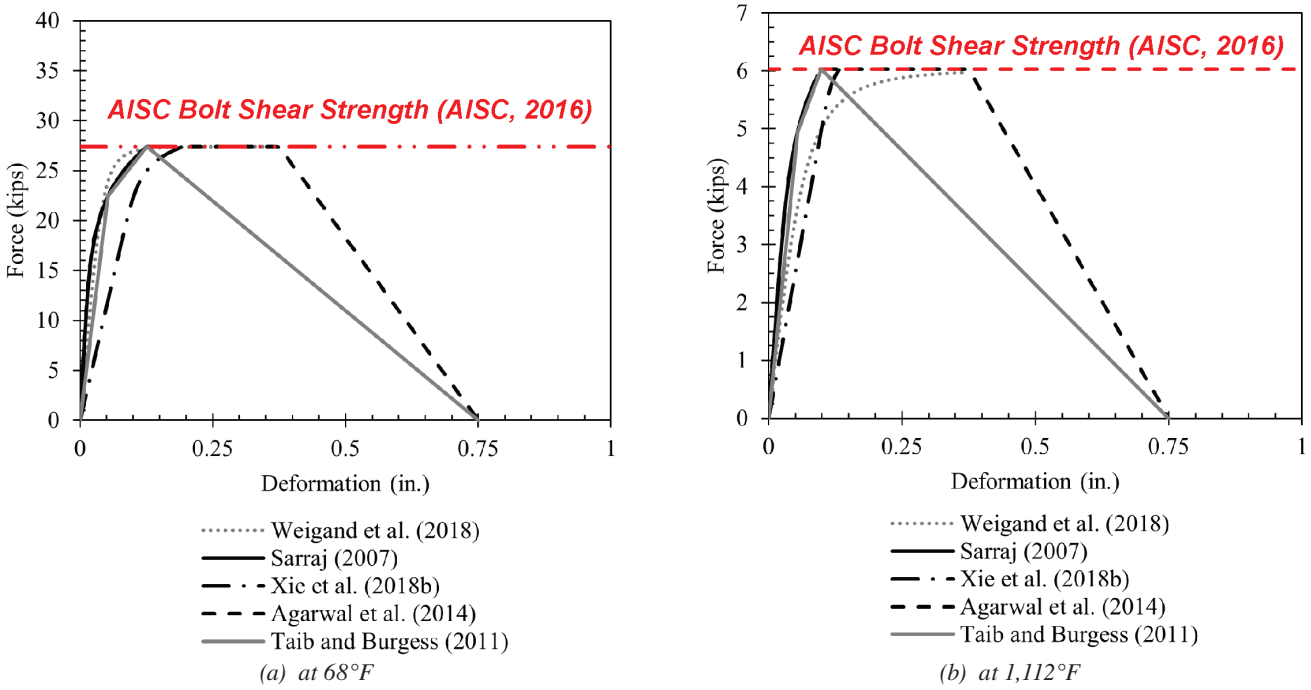

Fig. 2. Comparison of bolt shear models for a ¾-in.-diameter bolt with an ultimate stress of 140 ksi.

one-third of the bolt diameter, d_b) at ambient and elevated temperatures. However, the model developed by Weigand et al. demonstrated that larger deformations (about ⅜ in. or $d_b/2$) are achieved before the bolt shear capacity is reached and failure occurs. The model developed by Taib and Burgess (2011) considered the bolt to fail when it reaches its ultimate capacity such that the axial force capacity linearly decreases until there is zero resistance once the deformation is equal to the bolt diameter. Agarwal and Varma (2014) specified that the bolt resisted a force equal to the ultimate bolt shear capacity until the deformation was equal to half of the bolt diameter. At this point, the resisting force of the bolt in shear decreased linearly until it reached a value of zero at a deformation equal to the diameter of the bolt. In this way, Agarwal and Varma accounted for the ductility during the peak and post-peak portions of the F-δ relationship, and Taib and Burgess only accounted for ductility in the post-peak region of the F-δ relationship.

Experimental investigations (Yu et al., 2006; Peixoto et al., 2017), have shown that at temperatures greater than approximately 750°F, bolts in shear have additional ductility before and after they reach their ultimate deformation capacity. However, at ambient temperature, bolts in shear are less ductile and exhibit sudden failure (Yu et al., 2006; Peixoto et al., 2017). The ductility incorporated into the bolt shear components developed by Agarwal and Varma (2014) and Taib and Burgess (2011) is consistent with findings from experimental studies of bolts in shear at elevated temperatures but does not represent observed bolt behavior at temperatures less than 750°F. In contrast, the component models that did not consider ductility (Xie et al., 2018b; Sarraj, 2007) are consistent with observed bolt behavior at lower temperatures but do not well represent observed bolt behavior at temperatures greater than 750°F.

Analytical Models for Bolt Bearing Components

Bolt bearing component definitions were inconsistent in considering failure criteria and post-peak behavior. Although there is agreement in the literature that bolt bearing is a ductile failure mechanism, the amount of ductility incorporated within bolt bearing component models varies. Some bolt bearing components (Hajjar et al., 2019; Rex and Easterling, 2017; Sadek et al., 2008; Sarraj, 2007; Taib and Burgess, 2011; Weigand, 2017; Xie et al., 2018a, 2018b; Yu et al., 2009) had infinite ductility. For others (Agarwal and Varma, 2014; Koduru and Driver, 2014; Sadek et al., 2008), ductile failure was assumed to be initiated after a specific deformation of the bolt holes. Additionally, some researchers have developed bolt bearing components with different post-peak behaviors in tension and compression (Sadek et al., 2008). Specifically, Koduru and Driver (2014) developed these different behaviors to account for tearout versus bearing failures.

Temperature-dependent bolt bearing component models (Xie et al., 2018a; Sarraj, 2007; Agarwal and Varma, 2014), shown in Figure 3, are compared against edge tearout capacity per the AISC *Specification* (2016) at 68°F and 1,112°F, respectively (red dashed lines). The bolt bearing component derived by Xie et al. (2018b) was approximately 17% and 19% less than the strength calculated using the AISC *Specification* at 68°F and 1,112°F, respectively. The ultimate resistance approximated by the analytical model for bolt bearing derived by Sarraj (2007) was within 3% of the calculated edge tearout capacity.

The bolt bearing models proposed by Sarraj (2007) and Xie et al. (2018a) incorporated ductile post-peak behavior that gradually decreased after the ultimate capacity of the bolt bearing component was reached. The bolt bearing model proposed by Sarraj had a load resistance of 0 at approximately $9d_b$. The bolt bearing model proposed by Xie et al. (2018a) had a load resistance of 0 at approximately $21d_b$. Agarwal and Varma (2014) had failure initiated at a deformation of $½d_b$, corresponding to the failure criteria given for the bolt shear component. After the initiation of failure, the resisting force of the bolt bearing component decreased linearly until it was zero at a deformation of d_b.

Analytical Models for Gap/Contact Components

Researchers have incorporated a variety of different stiffnesses and capacities for the gap/contact between the bottom flange of the beam and the flange of the column (Yu et al., 2009; Hajjar et al., 2019; Agarwal and Varma, 2014; Hu et al., 2009; Taib and Burgess, 2011). Some researchers (Yu et al., 2009; Agarwal and Varma, 2014; Taib and Burgess, 2011) defined the gap/contact component to initially have no stiffness (simulating the gap between beam flange and column) and extremely high stiffness with unlimited capacity (simulating contact of the beam flange with the column) when the deformation was equal to the distance of the gap. This approach simulates the very high rotational stiffness that is achieved when the gap closes. However, this method does not consider deformation that may occur due to local buckling of the beam bottom flange.

Hajjar et al. (2019) defined the stiffness of the contact component to be equal to the axial stiffness of the bottom flange of the beam. Hajjar et al. also reduced the area of the bottom flange of the beam by a factor of 0.7 because only 70% of the beam flange was assumed to be in contact with the column flange. Hu et al. (2009) defined the gap/contact component to have a contact initial stiffness defined by the yielding of the column web instead of the beam flange. As shown in Figure 4, for a 42 ft W18×35 beam attached to a W12×106 column, the stiffness of the gap component approximated by the Hu et al. model is 777 kip/in., and the stiffness approximated by the Hajjar et al. model is 215 kip/in.

The stiffnesses obtained from using the Hu et al. (2009) and Hajjar et al. (2019) models for the same beam and column sizes are significantly different as shown in Figure 4. The Hu et al. model produces a relatively high stiffness (slope of the line in Figure 4), which may overestimate the stiffness of the contact between the beam flange and column stiffness if applied in a model that does not already consider damage, such as yielding, of the connected beam. Conversely, the Hajjar et al. model may overestimate the ductility of beam-to-column contact by only considering a portion of the beam cross section to be contributing to axial stiffness when contact occurs because of the lower stiffness the model produces (slope of the line in Figure 4).

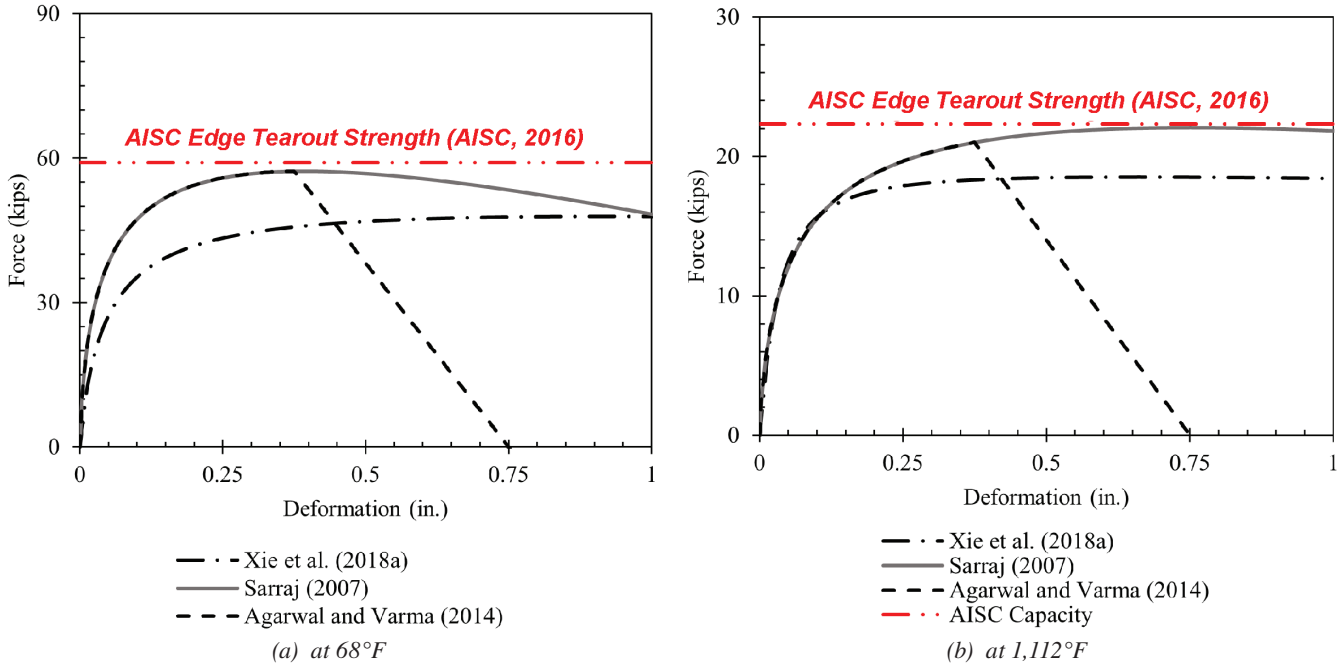

(a) at 68°F (b) at 1,112°F

Fig. 3. Comparison of bolt bearing models for a ¾-in.-bolt bearing on a 7/16-in.-thick plate with a yield stress of 50 ksi and ultimate stress of 70 ksi.

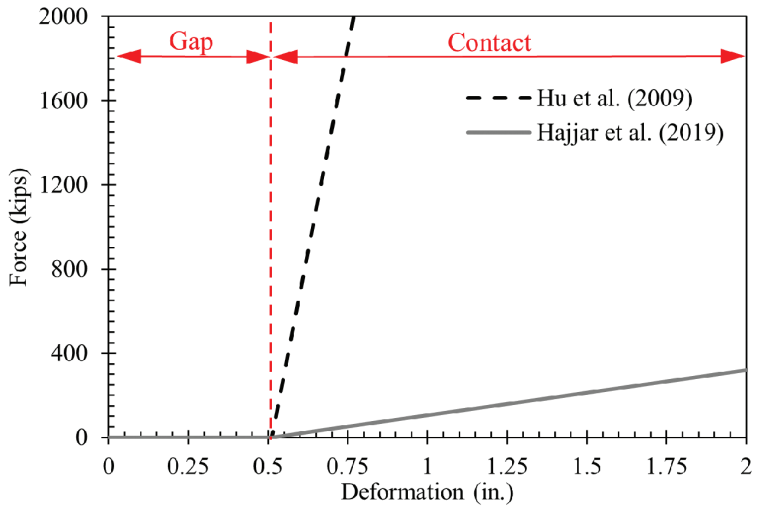

Fig. 4. Comparison of gap/contact components.

Analytical Models for Weld Components

Because the fillet welds attaching the shear tab to the column are extremely stiff and are typically designed to have a higher capacity than the other connecting elements, the weld component was often ignored in component models for shear connections. Although some researchers included weld components in their component models, very little validation has been done to test the weld component behavior. Koduru and Driver (2014) defined a weld component with a F-δ relationship defined by Lesik and Kennedy (1988). Hu et al. (2009) defined a weld component to have a maximum capacity and retention factors defined by Eurocode 3 (CEN, 2005a) with an ultimate deformation equal to 20% of the effective throat thickness of the weld, resulting in a linear F-δ relationship. Sadek et al. (2008) considered only the capacity, defined by the AISC *Specification* (2016), of the weld in the formulation of the component model and assumed it has infinite stiffness so that the deformation of the welds did not contribute to the component behavior. Kurikova et al. (2022) developed a weld component for use in design that conservatively estimated the plastic strain limit of the component to be 5% of the thickness of the weld.

Component Model Development

Component models have been utilized in many different scenarios where the behavior of gravity connections is of interest. Although the individual components of the connections are defined similarly because they represent the behavior of similar physical components, the development of a component model is dependent on its desired application. One method used by previous researchers to assemble a component model was to combine the individual springs into a single analytical expression or spring to represent the connection behavior (Hajjar et al., 2019; Taib and Burgess, 2011). This method was useful when a component model was used to account for connection stiffness and strength, but the performance of each individual component was not considered. Another method used to assemble the component model was to define each component as an individual spring that is located at the location of the connecting element that they represented (Agarwal and Varma, 2014; Hu et al., 2009; Koduru and Driver, 2014; Sadek et al., 2008; Sarraj, 2007; Weigand, 2017; Xie et al., 2018a, 2018b; Yu et al. 2009). This method resulted in a model that could be easily updated to reflect changes in geometric and material parameters and allowed the researchers to track individual component behavior. Researchers also developed component models of connections that have a combination of combined springs and single springs that represented the components. Weigand (2017) combined components located at the bolt hole (bolt bearing on the beam web, bolt bearing on the plate, and bolt shear) in series and then located a combined spring at the location of each bolt.

MODELING METHODOLOGIES FOR THE DEVELOPMENT OF A COMPONENT MODEL IN OPENSEES

This section summarizes the modeling methodologies for the development of a component model to simulate the behavior of shear tab connections subjected to fire scenarios. The component models in this study were developed in OpenSees (Mazzoni et al., 2006), but the methodologies utilized are applicable for use with other finite element programs. Individual component constitutive models were developed to represent the behavior of each active component in the connection assembly and the associated damage or failure modes. The components were then assembled into a component model in OpenSees. The developed component model was benchmarked against experimental data.

Identification of Active Components

Active components refer to the individual components of the connection whose deformation, resistance, and/or strength contributes to the behavior of the connection. As shown in Figure 5, for a typical shear tab connection, the active components include the shear behavior of the bolts, the bolt bearing on the beam web, the bolt bearing on the shear tab, the gap/contact between the bottom flange of the beam and the flange of the column, and the weld connecting the shear tab to the column flange. Friction between the components can be considered as an active component, but its effects are often considered to be minor. Therefore, friction was ignored in this study.

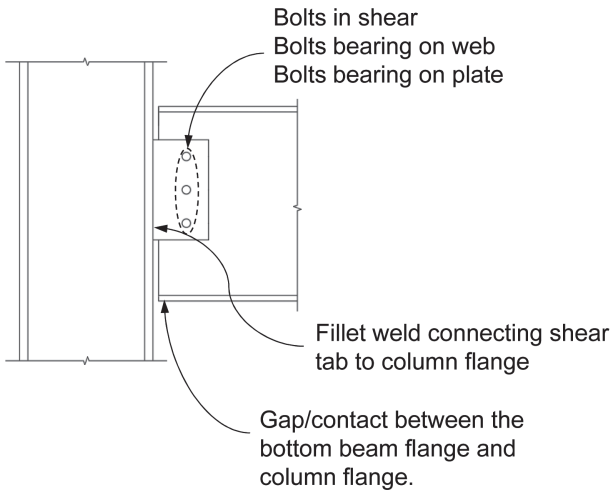

Fig. 5. Active components for a typical shear tab connection.

Component Constitutive Models

The behavior of the individual component springs was developed using the previous research presented earlier. Modifications were made to the component models developed by previous researchers to reflect observations reported from experimental investigations. The following sections provide an overview of force-deformation component models for each of the active components of the connections. The force-deformation plots shown in Figures 6 through 9 were developed for specific connection geometries provided within the captions of the figures. These plots will change with varying connection geometries.

Bolt Shear Component

Bolt shear behavior was modeled using the F-δ relationship proposed by Sarraj (2007). This component model for bolt shear was selected to simulate bolt shear behavior for a temperature range of 68°F to 1,472°F and any bolt type where F_u, E, and F_y were known. The F-δ relationship of the bolt component defined by Sarraj (2007) was calculated through four equations:

$$\Delta = \frac{F}{k_{v,b}} + \Omega\left(\frac{F}{F_{v,rd}}\right)^6 \tag{1}$$

$$F_{v,rd} = R_{f,v,b} f_{u,b} A \tag{2}$$

$$k_{v,b} = \frac{kGA}{d_b} \tag{3}$$

$$G = \frac{E}{2(1+\nu)} \tag{4}$$

where Δ is the relative bolt deformation, F is the force in the connection corresponding to Δ, $F_{v,rd}$ is the bolt shear strength (Equation 2), $f_{u,b}$ is the ultimate stress of the bolt material, $k_{v,b}$ is the bolt shearing stiffness (Equation 3), $R_{f,v,b}$ is a temperature-dependent strength reduction factor, Ω is a temperature-dependent curve fitting parameter, G is the shear modulus (Equation 4), ν is Poissons ratio, E is the elastic modulus, d_b is the diameter of the bolt, and A is the cross-sectional area of the bolt. Values for $R_{f,v,b}$ and Ω are tabulated in Sarraj (2007).

The Agarwal and Varma (2014) modifications were adopted to account for additional ductility, post-peak behavior of the bolts in shear, and bolt slip. Although Agarwal and Varma proposed modifications to account for post-peak ductility for all temperatures (including ambient temperature), bolt shear failure is brittle at ambient temperature. To account for brittle bolt shear failure at ambient temperature, the bolt shear component developed in this study loses all force resistance after reaching a deformation of half the bolt diameter (d_b/2) when the temperature is less than 750°F (Piexoto et al., 2017; Yu et al., 2009). The proposed model by the authors used a modified deformation at which the maximum resistance of the bolt occurred from d_b to ¾ d_b to reflect the post-peak behavior observed during experimental testing by others (Hu and Engelhardt, 2014; Fischer et al., 2018). The resulting F-δ relationship for bolt shear is presented in Figure 6 for temperatures of

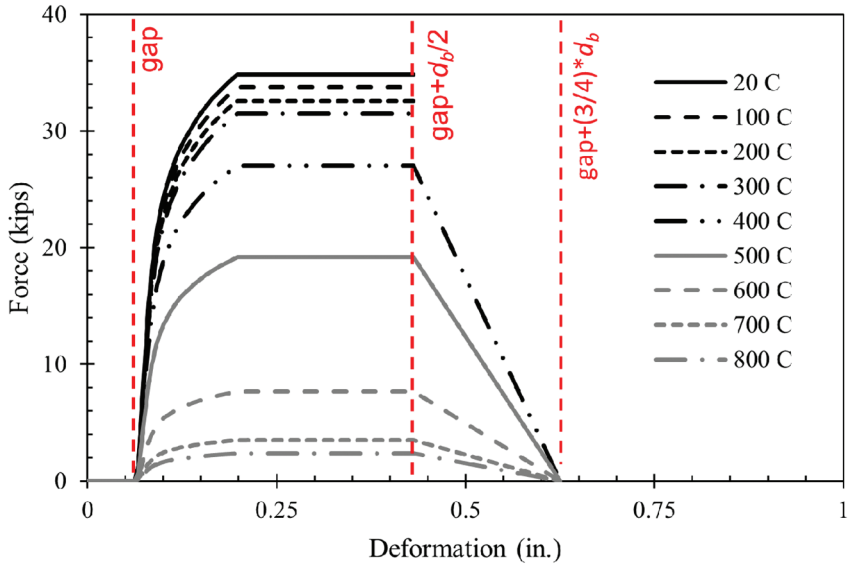

Fig. 6. Bolt shear component F-δ *relationship, for a ¾-in.-diameter bolt with an ultimate stress of 140 ksi, from Sarraj (2007) with modifications from Agarwal and Varma (2014) and experimental data.*

68°F to 1,472°F. The modification used by Agarwal and Varma specifies that the bolts retain their maximum shear capacity until the bolt reaches a deformation $d_b/2$. After the bolt reaches a deformation of $d_b/2$, the resistance of the bolt decreases linearly so that the capacity of the bolt is zero when the deformation is equal to $¾d_b$.

The bolt shear component model proposed by Sarraj (2007) was also modified to account for bolt slip. Bolt slip can occur in the connection when clear distance exists between the bolt and the edge of the bolt hole when the connection is constructed. To account for bolt slip, the connection was assumed to have deformation without any applied force for a deformation equal to the difference between the radius of the bolt hole and the radius of the bolt (assumed to be 1/16 in). In OpenSees, a small amount of stiffness was added to the portion of the F-δ curve representing this behavior to avoid singularity.

Bolt Bearing Components

Bolt bearing behavior was modeled using the F-δ relationship proposed by Sarraj (2007) with modifications for failure initiation and post-peak ductility. The F-δ relationship of the bolt bearing component defined by Sarraj was calculated through Equations 5 through 11.

$$K_i = \frac{1}{\frac{1}{K_{br}} + \frac{1}{K_b} + \frac{1}{K_v}} \tag{5}$$

$$K_{br} = \Omega t F_y \left(\frac{d_b}{25.4}\right)^{0.8} \tag{6}$$

$$K_b = 32Et\left(\frac{e_2}{d_b} - 0.5\right)^3 \tag{7}$$

$$K_v = 6.67Gt\left(\frac{e_2}{d_b} - 0.5\right) \tag{8}$$

$$\frac{F}{F_{b,rd}} = \frac{\psi\Delta'}{\left(1+\Delta'^{0.5}\right)^2} - \phi\Delta' \tag{9}$$

$$\Delta' = \Delta\beta\frac{K_i}{F_{b,rd}} \tag{10}$$

$$F_{b,rd} = \frac{e_2}{d_b} f_u d_b t \tag{11}$$

where K_i is the initial stiffness of the bolt bearing component; K_{br} is the bearing stiffness; K_b is the bending stiffness; K_v is the shearing stiffness; Ω, ψ, and ϕ are temperature-dependent curve fitting parameters; e_2 is the distance from the edge of the bolt hole to the edge of the plate in bearing; Δ' is the normalized deformation; Δ is the hole elongation; F is the bearing force; $F_{b,rd}$ is the bearing capacity of the plate; f_u is the ultimate stress of the bearing material; and β is a steel correction factor (taken as 1.0 for typical steels).

The modifications proposed by Agarwal and Varma (2014) were adopted to account for failure due to tearout in tension. The ductile post-peak behavior of the bolt bearing component developed by Agarwal and Varma corresponded to the bolt shear post-peak behavior. Therefore, the bolt bearing component developed in this study was defined to have a deformation of $¾d_b$ instead of d_b when there is zero resistance to conservatively reflect the post-peak ductility of the bolt shear component. This proposed component model used within the work summarized in this paper did not consider different F-δ relationships in tension and compression. This was a conservative approach for bolt bearing components loaded in compression and allowed for easier implementation into OpenSees. As shown by the F-δ relationship of bolt bearing components presented in Figure 7, the bolt bearing component model proposed by Sarraj (2007) was employed until the bolt bearing component reached a deformation of $d_b/2$. Afterward, the resistance of the bolt bearing component decreases linearly such that at a deformation of $¾d_b$, the resistance of the bolt bearing component is zero. Temperature-dependent retention factors for plate and web mechanical properties were utilized (CEN, 2005a; AISC, 2016).

Gap/Contact Component

The proposed gap/contact component F-δ relationship shown in Figure 8 has zero stiffness when deformation is less than the distance between the bottom beam flange and the column flange. After the gap/contact component has a deformation equal to the distance of the gap, the gap/contact component has a very high stiffness representing the beam flange in contact with the column flange. The stiffness during contact proposed by Hu et al. (2009) was adopted to give a high level of contact stiffness and because the axial stiffness of the beam, which is captured by the Hajjar et al. (2019) gap/contact component, is considered within the formulation of the beam element in this study. In addition to the gap/contact component developed by Hu et al., a modified definition of the gap/contact component model will be evaluated for cases where there is potential for local buckling of the supported beam. As shown in Figure 8, the modified gap/contact component defines the behavior of the component after contact to be elastoplastic. The yielding behavior of the modified gap/contact component accounts for damage to the beam by limiting the amount of force that can be transferred through the beam-to-column contact to the yield strength of the bottom flange of the beam (AF_y), where the yield strength is temperature-dependent.

Weld Component

The weld component was defined to incorporate a load capacity corresponding to the capacity of the weld as calculated by the AISC *Specification* (2016) and a deformation capacity consistent with the findings from Kurikova et al. (2022). The *F*-δ relationship increased linearly until the force was equal to the capacity of the weld as calculated by the AISC *Specification*. The maximum deformation of the weld was assumed to be 10% of the effective throat thickness of the weld. The deformation capacity of the weld component was chosen to reflect the deformation at failure of experimentally tested, transversely loaded fillet welds while still incorporating the conservatism employed by Kurikova et al. Welds are very stiff and brittle with little deformation before failure and no post-peak ductility. Therefore, welds can be considered active components when they are at risk of failure, but if the welds have sufficient capacity to resist the load demands placed on the connection, they contribute very little to the overall connection behavior and need not be included.

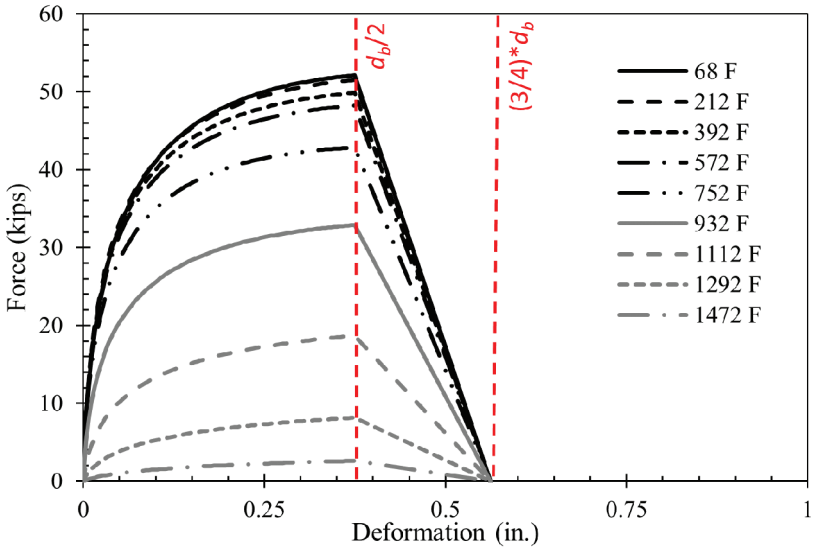

Fig. 7. Bolt bearing component F-δ *relationship for a ¾-in.-diameter bolt with an ultimate stress of 140 ksi.*

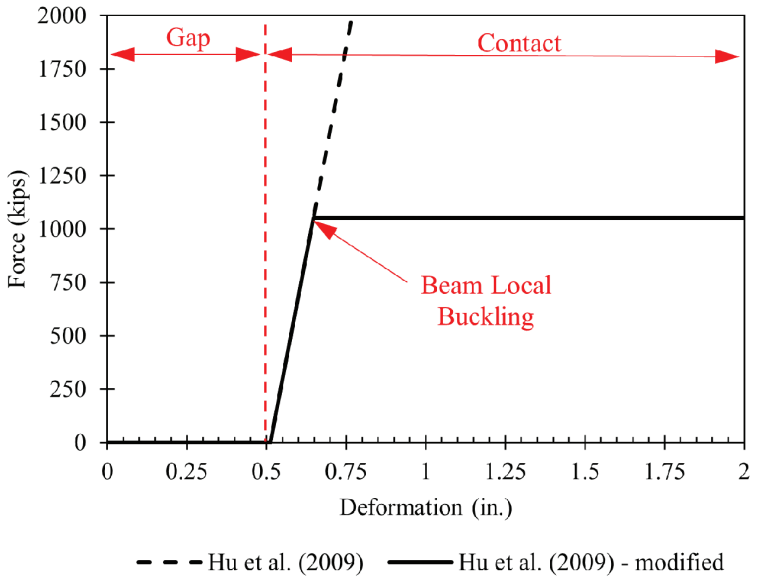

Fig. 8. Proposed gap/contact component F-δ *relationship for a W18×35 beam with a yield strength of 50 ksi.*

Assembly of OpenSees Component Model

The components were assembled into a component model within OpenSees. One node was created to represent the top of the column, and another node was created at the same location to represent the end of a beam. Nodes were then created such that each component could be placed at a vertical location corresponding to the location of the component they represented. A representation of the component model is presented in Figure 9. The F-δ relationships for the connection components at each bolt (bolt shear, bolt bearing on the shear tab, and bolt bearing on the beam web) were placed in series and combined prior to inputting the data into OpenSees, such that a single component could be defined at the location of each bolt (Figure 9 in blue). The resulting component used to simulate bolt shear, bolt bearing on the shear tab, and bolt bearing on the beam web will now be referred to as the bolt component. The gap/contact component F-δ curve was assigned at the bottom of the bottom flange (Figure 9 in purple). The weld component was discretized into a set of eight components where each component represented approximately 1 linear in. of the weld. As shown in Figure 9, the components were connected with rigid elements to the beam or column node. The components have only axial stiffness, and the end node for the beam is restrained to have the same vertical translation as the corresponding column node. In this way, the component model developed in this study only considers failure of the connection due to imposed axial force and moment demands and assumes loading in shear will not cause failure or damage within the connection throughout the fire.

In OpenSees, multilinear and hysteretic uniaxial materials were used to define the F-δ relationship for the bolt component. A multilinear material was used to create a backbone curve that more closely aligned with the nonlinearity of the calculated backbone curve. The hysteretic material is used to account for load reversal in the bolt component and allowed for the updating of temperature-dependent mechanical properties when fire loading is transient. As shown in Figure 10, seven points were used to capture material nonlinearity when a multilinear material was used in OpenSees. When a multilinear material was used to define the bolt component, a *MinMax* material was used to prevent reloading after the load-carrying capacity of the bolt component was zero at a deformation of $¾d_b$. A hysteretic material limited the definition of the backbone curve to three points. When a hysteretic material was used to model the bolt component, the first point on the backbone curve was selected to be at a location corresponding to two-thirds of the effective yield stress and one-fifth of the effective yield strain to simulate the initial stiffness of the bolt component. The next two points on the hysteretic backbone curve were the effective yield point and the point of failure initiation as depicted in Figure 10. A *MinMax* material was used to define failure for the hysteretic backbone curve after the maximum strain was reached. The gap/contact component was created using a multilinear uniaxial material with a very small initial stiffness until the deformation is equal to the distance of the gap. The weld component F-δ relationship was created in OpenSees using a *MinMax* material that referenced an elastic uniaxial material so that the weld components had a constant stiffness and a maximum strain that was 20% the effective throat thickness of the weld; the strength is calculated using the AISC *Specification* (2016), including the strength reduction factor of 0.75.

Two methods for modeling steel structures exposed to fire are available in OpenSees: (1) using preexisting OpenSees objects that were designed specifically for thermal applications, referred to herein as *OpenSeesThermal* (Jiang and Usmani, 2013; Khorsani et al., 2015; Maddalozzo et al., 2020; Walls et al., 2018), and (2) using OpenSees parameter objects to update material properties of steel in each step of the analysis to account for temperature-dependent mechanical property degradation and thermal expansion, referred to herein as *OpenSeesParameter* (Whyte et al., 2016). When

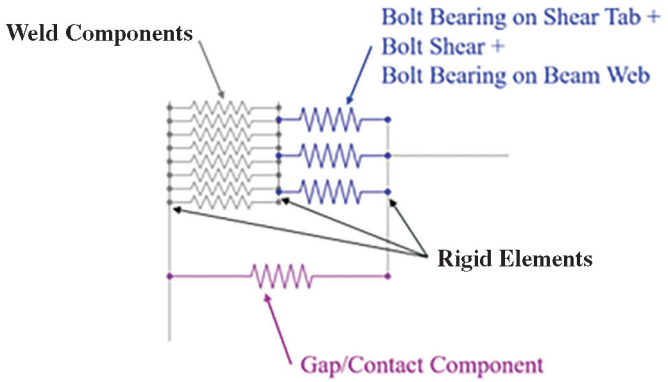

Fig. 9. Pictorial representation of the component model developed in OpenSees.

using OpenSeesThermal to simulate the behavior of an axially unrestrained beam exposed to elevated temperatures, a large axial force is developed; however, this axial force is correctly approximated to be zero when using OpenSeesParameter. The authors observed that when thermal elongation is increasing or decreasing between time steps within OpenSees, large axial forces are developed, even for axially unrestrained beams. These observations suggest that the methods of simulating a change in thermal elongation used by OpenSeesThermal results in the development of large axial forces. A more in-depth investigation is required to determine the exact origin of axial force development when using OpenSeesThermal to simulate a laterally unrestrained beam subjected to heating, which is outside the scope of this research. However, because the performance of gravity connections is sensitive to large axial loads during a fire scenario, OpenSeesParameter is used in this research in lieu of OpenSeesThermal to simulate the effects of temperature on steel connections and framing systems. A more in-depth discussion of this behavior is found in Gordon (2022).

BENCHMARKING COMPONENT MODELS AGAINST EXPERIMENTAL DATA

The OpenSees component model was benchmarked against two sets of experimental data that consisted of isolated connections tested at elevated temperatures. The component model was then used to simulate a long-span composite beam during a fire scenario to evaluate the contribution of simulating the connection behavior on the fire performance of the beam. The experimental study performed by Hu and Engelhardt (2014) was selected for benchmarking to evaluate the behavior of the components located at each bolt under pure axial load and elevated temperatures. The experimental study performed by Yu et al. (2009) was selected for benchmarking to evaluate the behavior of the gap/contact component and the entire component model when a combination of shear force, axial force, and bending moment is applied at ambient and elevated temperatures. The component model was then applied to simulate the behavior of a two-dimensional (2D) frame with a long-span composite beam and shear tab connections exposed to a fire scenario (Choe et al., 2019).

Isolated Connection Benchmarking: Hu and Engelhardt

Hu and Engelhardt (2014) performed a series of experimental tests to quantify the behavior of shear tab connections at elevated temperatures when subjected to pure tensile axial loading. In these tests, the connections were heated to a target temperature and then loaded monotonically until failure. The geometry of the shear tab connections tested by Hu and Engelhardt is presented in Figure 11.

The mode of failure for the specimens heated to 68°F and 750°F was bolt bearing failure of the shear tab, and the specimens heated to 932°F, 1,022°F, and 1292°F failed due to bolt shear. As the temperature increased, the capacity of the connection decreased, and larger deformations within the connection occurred. Although the specimen tested at ambient temperature had the largest ultimate deformation, very little post-peak ductility was present for specimens heated to 68°F and 750°F. However, post-peak ductility was observed for specimens heated to 932°F, 1,022°F, and 1,292°F.

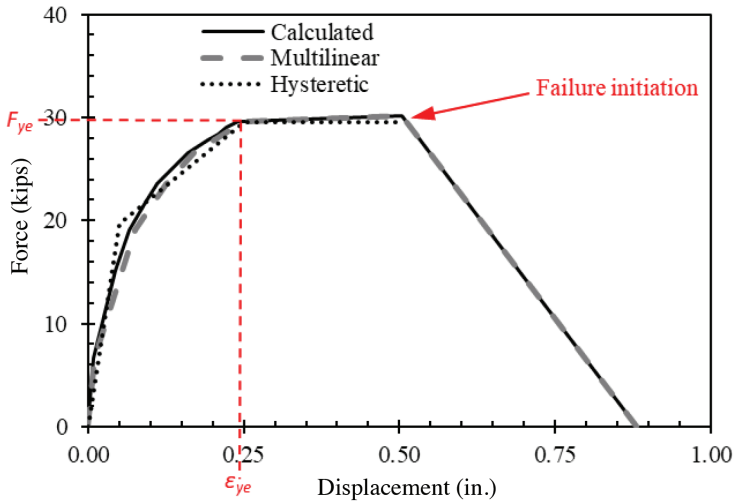

Fig. 10. Example of the simplified F-δ *relationships of the bolt component with a ¾-in.-diameter bolt with a yield strength of 116 ksi bearing on a ⅜-in.-thick plate and a ¼-in.-thick web with yield strengths of 52.2 ksi.*

The component model developed to simulate the experimental tests only included the active components. Because the Hu and Engelhardt (2014) tests only subjected the specimens to pure axial loading, the connection does not rotate, and the gap/contact between the stub beam and the column was not considered to be an active component. The weld had a larger capacity than the other connecting elements, and the stiffness of the weld was extremely high. Therefore, the weld was also not considered as an active component. The bolt component used the bolt retention factors calculated by Hu and Engelhardt from the experimental data.

Results: Hu and Engelhardt

The results from the OpenSees component model are compared with the experimental results from Hu and Engelhardt (2014) graphically in Figure 12. Table 1 compares the load capacities (denoted maximum load) and the deformation recorded before the connection fails (denoted maximum deformation) observed from experimental testing and predicted by OpenSees. In the result comparisons, load capacity refers to the maximum load that was resisted by the connection, and failure is signified by a sudden loss of load-carrying capacity. The F-δ curves presented in Figure 16 show that overall, the OpenSees component model simulated the behavior of the connections tested by Hu and Engelhardt. Although there were some differences between the experimental and analytical results, the general nonlinear shape of the F-δ relationship was accurately predicted by the component model. As shown in Table 1, the error in connection capacity predicted by the component model was less than 10% for all temperatures. The errors in ultimate deformation predicted by the component model were greatest for temperatures of 68°F and 750°F (28% and 61%, respectively). While these errors demonstrate that the model was unable to predict the ultimate deformation, in both of these simulations, the ultimate load was calculated by the OpenSees model within 10% of the experimentally measured ultimate load. In addition, both of these experiments failed in bolt tearout. The errors in ultimate deformation predicted for temperatures of 932°F, 1,022°F, and 1,292°F were less than 15%.

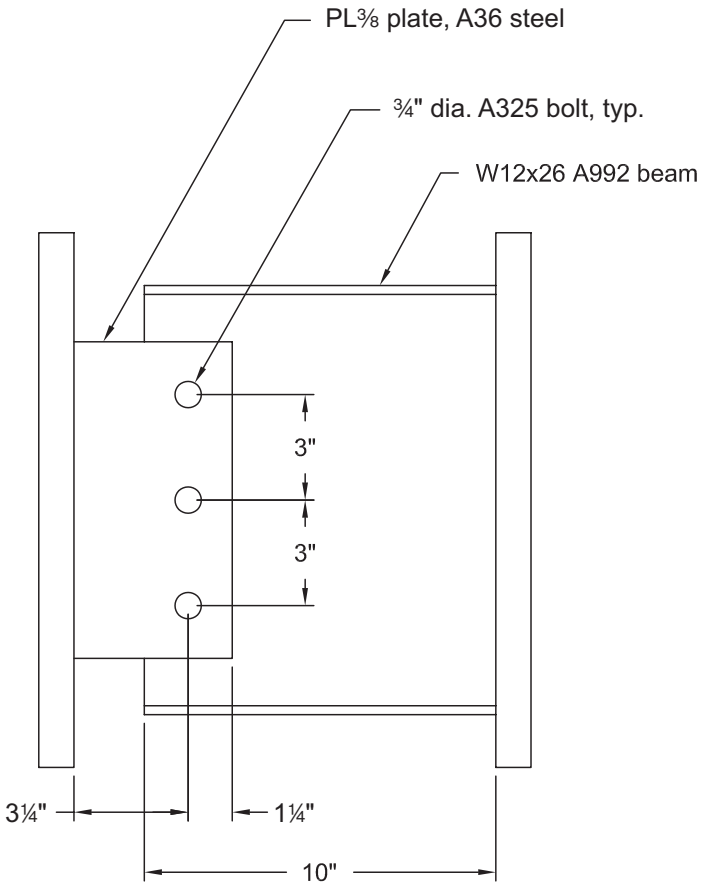

Fig. 11. Hu and Engelhardt (2014) test specimen geometry.

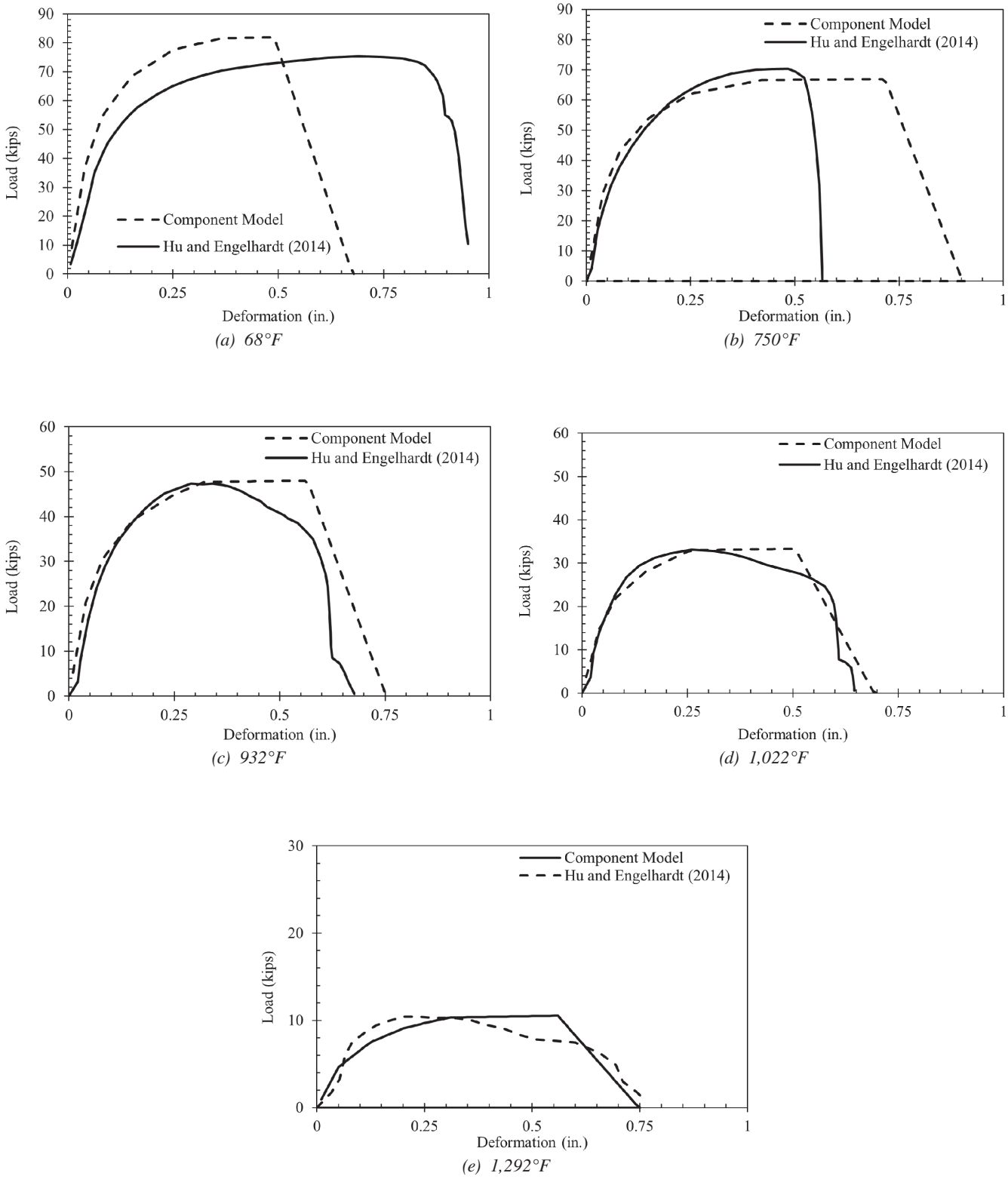

Fig. 12. Result comparison for Hu and Engelhardt (2014) tests.

Table 1. Comparison of Results Gathered from the OpenSees Component Model and Hu and Engelhardt Tests						
	Hu and Engelhardt (2014)		Component Model (OpenSees)			
Temperature (°F)	Maximum Load (kips)	Maximum Deformation (in.)	Maximum Load (kips)	Maximum Deformation (in.)	% Error Load	% Error Deformation
68	75.3	0.951	81.9	0.680	9%	28%
750	70.4	0.567	66.9	0.910	5%	61%
932	47.4	0.677	48.0	0.760	1%	12%
1022	33.1	0.646	33.3	0.700	1%	8%
1292	10.4	0.764	10.5	0.750	1%	2%

Isolated Connection Benchmarking: Yu et al.

The experimental program performed by Yu et al. (2009) evaluated the behavior of a shear tab connection subjected to elevated temperatures and a combination of axial force, shear force, and bending moment. To achieve a combination of axial force, shear force, and bending moment demands on the connection, Yu et al. applied load to the test specimens at angles of 35° and 55°. The test specimen geometry is presented in Figure 13. The force-rotation behavior recorded by Yu et al. showed that the connection has a decreasing load capacity and increasing rotational ductility as the temperature increases. All connections tests performed by Yu et al. that are used for benchmarking failed in bolt shear.

As previously described, Yu et al. (2009) developed a component model based on the component definitions proposed by Sarraj (2007). The active components included in the component model were bolt shear, bolt bearing on the plate and web, and friction between the plate and the web. To account for ductility of the bolts in shear, Yu et al. assumed the bolt component to either maintain its load-carrying capacity until a deformation equal to half of the bolt diameter ($d_b/2$) and then fail suddenly or have infinite ductility.

The retention factors for bolt shear calculated by Hu and Engelhardt (2014) were developed to simulate the experiments performed by Yu et al. (2009). Additionally, Yu et al. suggests that the bolt shear strength, F_{vrd}, be calculated as $0.692F_{ub}A_s$ instead of $0.6F_{ub}A_s$ to reflect the actual material properties of the bolt. Therefore, in the study described in this paper, the authors calculated the bolt shear strength as $0.692F_{ub}A_s$ in the proposed component model when benchmarking the proposed component model against the Yu et al. experimental tests.

Isolated Connection Benchmarking Results: Yu et al.

Figures 14 and 15 compare the test data from Yu et al. (2009) (black solid lines) with the proposed component model implemented in OpenSees (black dashed lines) developed by the authors. The results using the component model developed by Yu et al. are presented as gray dashed lines. The gray x's in Figures 14 and 15 show where failure occurs in the Yu et al. component model when the bolt component is considered to fail suddenly at a deformation of $d_b/2$; however, as seen from the testing data, that point does not always correspond with the peak load. In Table 2, the load capacities (denoted maximum load) and the deformation that occurred at the load capacity (denoted maximum rotation) are recorded.

At the beginning of the experimental tests, the bolts were not bearing against the shear tab or the beam web, allowing for rotation to occur with little resistance. Because the starting distance between the bolts and the shear tab and web edges are unknown and vary between experimental tests, the initial bolt slip was estimated for each test based on the experimental data. The estimated bolt slip was incorporated into the results of the simulation performed by the authors consistent with the methodologies used for the component model benchmarking performed by Yu et al. (2009). As the bolts came into contact with the beam web and shear tab, the stiffness of the connection increased until failure occurred. In the experimental tests and each simulation, the connection began to lose load-carrying capacity after the top bolt or the top and middle bolt failed (Yu et al. 2009). In the ambient tests, bolt shear failure resulted in a sudden loss of load-carrying capacity, after which some load transfer was regained as the middle bolt reached its maximum capacity and failed. However, the connections tested at elevated

temperatures exhibited a more gradual loss of load-carrying capacity. The component model implemented in OpenSees (developed by the authors) simulated the change from brittle to ductile failure as temperature increased; however, the component model developed by Yu et al. did not account for post-peak behavior and, therefore, could not simulate the ductile failure at elevated temperatures.

The numerical results presented in Table 2 show that the error in maximum load predicted by the component model implemented in OpenSees (developed by the authors) was equal to or less than 20%, except for the case where the load angle was 35° and the connection was heated to 1202°F (the error for this case was 31%). The errors in maximum connection rotation were less than 20% when temperatures exceeded 68°F. The close correlation between experimental and component model results demonstrated the accuracy of the OpenSees component model in predicting connection behavior.

Discussion on Benchmarking against Isolated Connection Experimental Studies

The results from benchmarking the component model against isolated connection tests show that the component model developed in OpenSees can simulate connection behavior and predict connection capacity at ambient and elevated temperatures. The agreement of results for the Hu and Engelhardt (2014) tests demonstrated the behavior of the components located at each bolt (bolt shear, bolt bearing on the beam web, and bolt bearing on the shear tab) when subjected to a purely axial load. The agreement of results for the Yu et al. (2009) test demonstrated the behavior of the gap/contact component and the overall connection behavior when subject to a combination of shear force, axial force, and bending moment at elevated temperatures. The comparison of results obtained from the component model developed by Yu et al. and the component model

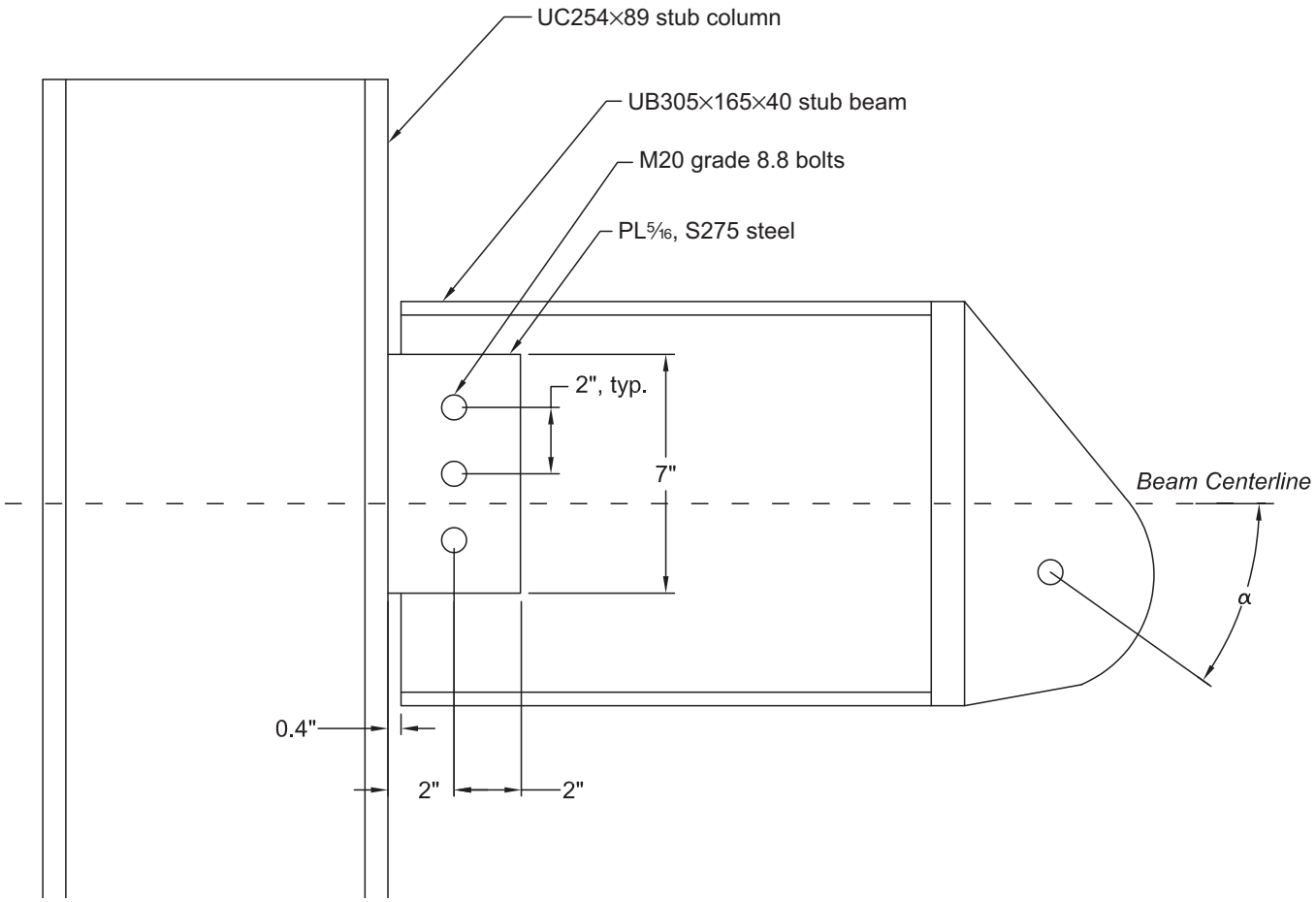

Fig. 13. Yu et al. (2009) test specimen geometry.

Table 2. Comparison of Results Gathered from the OpenSees Component Model and Yu et al. (2009) Tests						
Load Angle = 35°						
	Experimental Results		**Component Model (OpenSees)**			
Temperature (°F)	**Maximum Load (kips)**	**Maximum Rotation (deg)**	**Maximum Load (kips)**	**Maximum Rotation (deg)**	**% Error Load**	**% Error Rotation**
68	41.44	7.85	40.64	6.76	2%	14%
842	18.96	5.99	17.53	6.02	8%	1%
1022	8.66	7.02	9.11	5.79	5%	18%
1202	4.32	7.31	5.66	5.96	31%	18%
Load Angle = 55°						
	Experimental Results		**Component Model (OpenSees)**			
Temperature (°F)	**Maximum Load (kips)**	**Maximum Rotation (deg)**	**Maximum Load (kips)**	**Maximum Rotation (deg)**	**% Error Load**	**% Error Rotation**
68	32.89	11.09	29.19	9.26	11%	16%
842	15.93	6.30	14.76	6.02	7%	4%
1022	7.77	6.56	7.73	5.79	1%	12%
1202	4.03	6.27	4.74	5.96	18%	5%

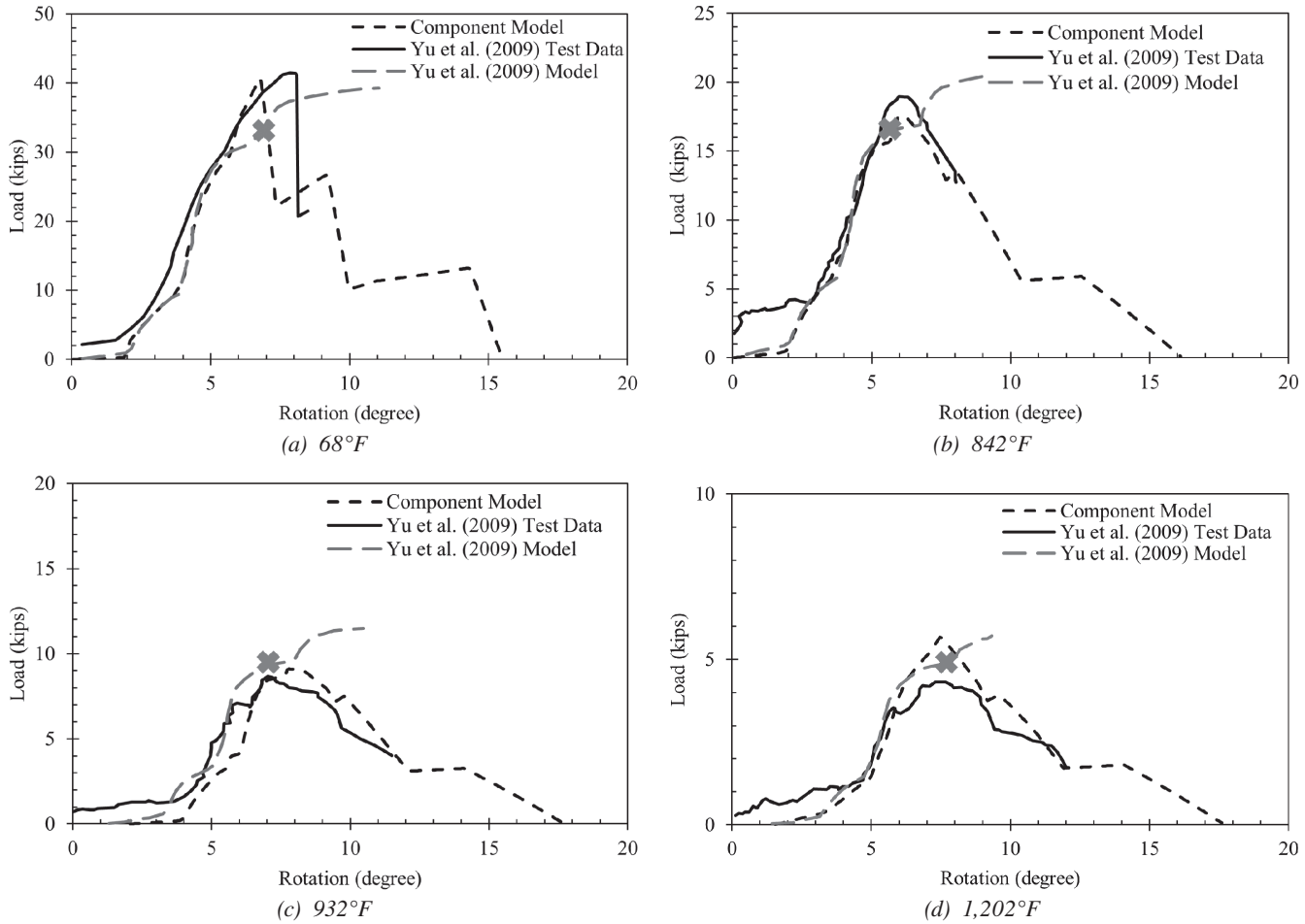

Fig. 14. Result comparison for Yu et al. (2009) tests with a load angle of 35°.

implemented in OpenSees highlights the importance of defining failure criteria for individual components when simulating the post-peak behavior of connections in fire.

The significant errors (greater than 20%) in maximum deformation at temperatures of 68°F and 760°F that were present when simulating the Hu and Engelhardt (2014) experiments indicate that the model did not accurately simulate the ductility of the connection when bolt tearout occurred. Percent errors were also high when predicting the maximum load in the Yu et al. (2009) experiments when the temperature was 1,202°F. To mitigate these errors and improve the developed component model, additional research is necessary to develop and incorporate an analytical model for bolt tearout failure that better represents observed bolt tearout failure in shear tab connections.

NIST Composite Beam Tests: Choe et al.

The component model implemented in OpenSees and benchmarked again Hu and Engelhardt (2014) and Yu et al. (2009) was then used to simulate a 2D frame consisting of a composite beam with shear tab connections (Choe et al., 2019). The test assembly consisted of a W18×35 steel beam with 6.25-in.-deep concrete on metal deck that included a 3-in.-deep metal deck (Figure 16). The beams were connected to W12×106 columns that were fixed to the strong floor in the National Fire Research Laboratory (NFRL) at the National Institute of Standards and Technology (NIST). To provide lateral support and restraint during testing, a support lattice was constructed which braced the columns at their height and mid-height (Choe et al., 2019).

Spray-applied fire-resistive material (SFRM) was used to provide a 2 hr fire resistance rating (FRR) for the steel beam (⅝ in.) and a 3 hr FRR for the columns (1 in.). The thickness of fire protection on the connections matched that of the columns (1 in.).

This composite beam test was part of a larger investigation to examine the influence of varying simple (shear) connections used in U.S. construction practices on the

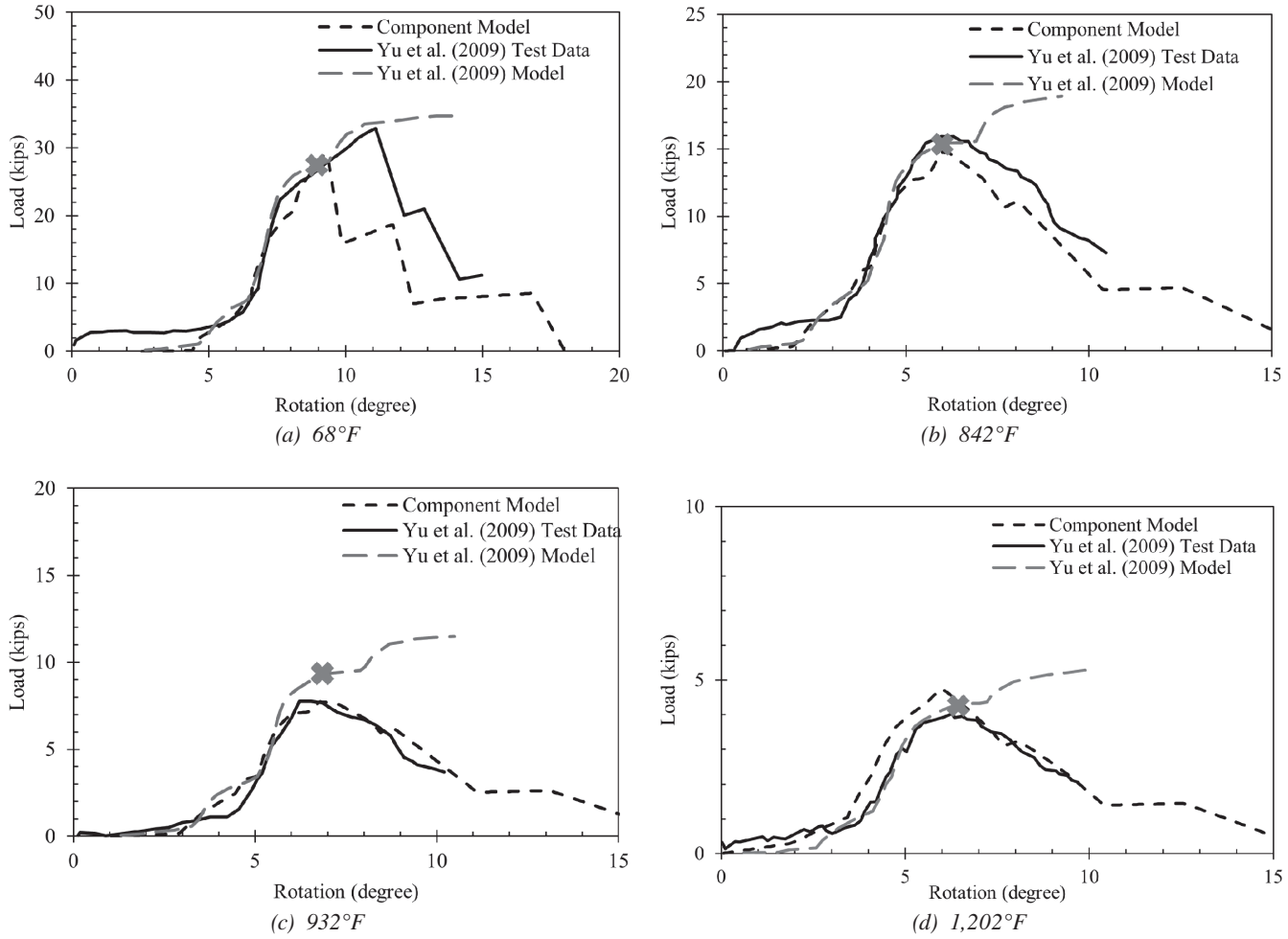

Fig. 15. Result comparison for Yu et al. (2009) tests with a load angle of 55°.

behavior of composite beams in fires (Choe et al., 2019). This research only benchmarked against the specimen that used a shear tab connection (referred to as test CB-SP in the NIST publications). This connection consisted of a 7/16-in.-thick ASTM A36/A36M shear tab connected to the column through a 5/16 in. fillet weld and connected to the beam web through three 3/4-in.-diameter ASTM F3125/3125M Gr. A325 bolts (Figure 17).

The specimens tested by Choe et al (2019) were subject to a static mechanical load and a transient thermal load. Mechanical loading was first applied to the system using hydraulic actuators that loaded the composite beam through a load truss. The method for mechanical loading resulted in 6 point loads along the length of the beam. A total of 24 kips was applied (6 point loads, 4 kips each) followed by heating until the beam failed.

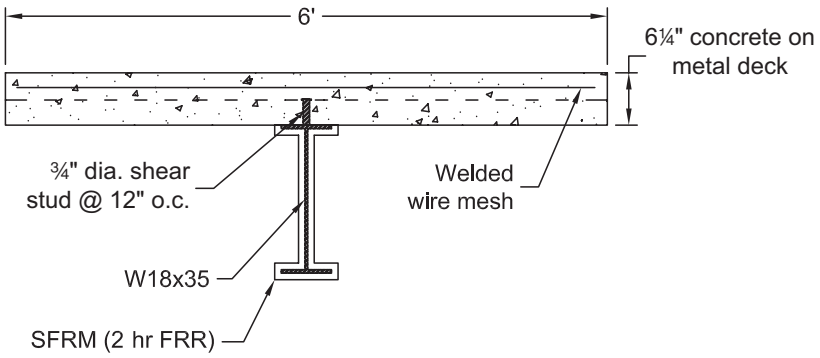

Fig. 16. NIST composite beam section.

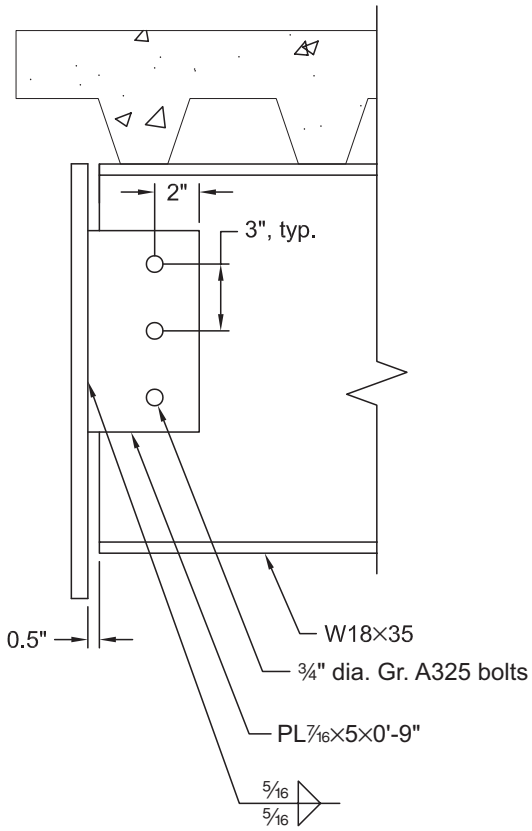

Fig. 17. Shear tab connection used in CB-SP NIST composite beam test.

After the mechanical loads were applied, thermal loading was applied to the assembly during the test by natural gas-fueled burners. The burners were used to simulate a compartment fire that was representative of a realistic yet potentially threatening fire event (Choe et al., 2019). During the heated test, the burners were set to operate at an average heat release rate of approximately 3791 BTU/s (4 MW). Once the composite beam assembly failed, the mechanical load was removed, the burners were turned off, and the compartment was allowed to cool naturally. During the test, the east beam-to-column connection failed due to weld unzipping at approximately 65 min after the beginning of the fire test, causing the collapse of the east end of the composite beam.

The locations of recording equipment used by NIST that are relevant to this study include the end rotations and the downward deflection of the beam recorded at approximately 3 ft from midspan. Temperatures were recorded during the test using Type K thermocouples at five locations along the depth of the W18×35 beam, four locations on the shear tab connection, and five locations throughout the depth of the slab. The temperatures recorded during the NIST test were input into the analytical model to determine the degraded mechanical properties of the steel beam and columns during the simulation.

To simulate the NIST assembly in OpenSees, the composite beam section was modeled using a fiber discretized section with concrete and steel material properties assigned to the appropriate fibers. This modeling approach inherently assumes that the beam is fully composite. The steel W-shape was assigned five temperature regions (one for each flange and three equally spaced in the web) corresponding to the number and location of thermocouples used in the NIST experiment. The experimentally measured temperatures of the slab were relatively low (below 392°F); therefore, the concrete slab and steel reinforcing were assumed to be unheated, and the slab was assigned a single temperature region. The columns were also modeled using a fiber discretized section that consisted of five temperature regions (one for each flange and three equally spaced in the web).

Eight connection model variations (V1–V8) were evaluated, as outlined in Table 3. V1 consisted of a purely pinned connection, which represented the behavior of the assembly when a component model is not considered. V2 included only bolt and weld components to evaluate the stiffness and overall behavior of the component model without the inclusion of a gap/contact component. V3 evaluated the forces developed in the connection when a gap/contact component is included in the component model. V4 and V5 included welds with gap/contact components and bolts with gap/contact components, respectively, to evaluate the failure behavior of the bolts and welds when modeled in combination with a gap/contact component. V6 and V7 compared the differences resulting from using a hysteretic and multilinear bolt component model and evaluated the effects of using a component model when all connection components that contribute to connection behavior are simulated. V8 demonstrated the impact of considering beam damage by including such considerations within the gap/contact component constitutive model. In all component model variations, the component force-deformation relationships were not temperature dependent because the maximum temperature recorded in the connection during the test did not exceed 513°F. At this temperature (513°F), the weld material is assumed to have no reduction in strength (CEN, 2005a), and the bolts are assumed to retain 90% of their original strength (AISC, 2016).

The test and model results that are used to define the assembly behavior are deflection near midspan (denoted VD3), connection rotation at both ends, and the axial force at the beam ends. While deflections and connection rotations were directly measured during the experiment, the axial forces at the beam ends were calculated based on the recorded strains in the bracing system (Choe et al., 2019). In the simulations, the axial forces developed at the ends of the beams and the axial forces transferred through only the connecting elements (weld and bolt components) are recorded.

During the test, the composite beam is loaded at ambient temperature. While the load is sustained, the beam is exposed to a fire scenario. Deflections began to increase as the temperature increased. During heating, local buckling occurred at the beam ends at a time of approximately 40 min. Beam buckling resulted in strain reversal and a loss of compressive axial load at the beam ends. At a time of 65 min, the beam deflected approximately 21.6 in., and weld failure occurred at the west connection. At this time, there was some additional midspan beam deflection (approximately 5.5 in.), and the west connection rotation increased significantly. After connection failure, the beam was allowed to cool naturally, the load was removed, and there was some deflection and connection rotation recovery.

Effects of Component Model Implementation into NIST Composite Beam Simulation

The benchmarked component model was implemented within a 2D frame to simulate the behavior of a composite beam with shear tab connections during a fire scenario. The beam deflection, the connection rotations, sum of forces through connecting components, and lateral force reactions at the end of the beam were recorded when using different variations of the component model (Figure 18). The midspan deflections approximated by using V1 (a pinned connection) in the analytical model are 29% lower than those recorded during the experimental test (Choe et al., 2019)

Table 3. Connection Model Variations for Benchmarking against the NIST (Choe et al., 2019) Composite Beam Test						
Connection Model Variation	Included Components				Bolt Material Type	
	Pin	Welds	Bolts	Gap/ Contact	Multilinear	Hysteretic
V1	√					
V2		√	√		√	
V3	√			√		
V4		√		√		
V5			√	√	√	
V6		√	√	√	√	
V7		√	√	√		√
V8		√	√	√*		√
* gap/contact component includes beam damage considerations						

when the west connection fails at 65 min. Initially, a tensile axial force of 36 kips is present in the beam when using V1. As the beam expands due to thermal elongation, the tensile force at the ends of the beams decreases. At approximately 35 min, tensile forces begin to increase due to the flexural yielding of the beam [Figure 18(c)]. After the mechanically applied gravity loads are removed from the beam at a time of 65 min, an axial force of less than 11 kips is developed.

The deflections and connection rotations changed by less than 20% during the duration of the test when bolt and weld components are incorporated into the proposed component model to simulate the shear tab connections (V2) as compared to a purely pinned connection (V1). Including bolt components when simulating the connection (V2) resulted in slightly larger midspan deflections (less than 1 in.) between times of 50 and 65 min as compared to a purely pinned connection (V1). Connection rotations approximated when using V2 remained within ±0.017 rad of those approximated by V1. Additionally, using a component model that considers the initial gap between the bolt and the edge of the bolt holes (V2, V5, V6) simulated the initially unrestrained displacement of the bolt components, and axial forces were not initially developed as they were when the bolt hole gap is not considered (V1, V3, V4, V7).

When a gap/contact component was included in V3 (purely pinned connection with gap/contact component) and V4 (only weld and gap/contact component), the gap between the beam and column flanges closed at approximately 35 min, and large axial forces began to develop [Figures 18(c) and 18(d)]. In V3, gap closure resulted in reduced midspan deflections, and the maximum deflection was 39% less than the experimentally measured just before connection failure. As the assembly cooled, connection rotation was recovered in the analytical model, and the gap opened at a time of approximately 117 min. When the gap closed at approximately 35 min in V4, large bending moments began to develop at the beam ends as large compressive forces were transferred through gap/contact component and large tensile forces were transferred through the weld components. At a time of 44 min, the tensile force transferred through the weld components exceeded the weld strength (190 kips calculated using the AISC *Specification*) and the welds failed. Weld failure caused nonconvergence of the analytical model signifying the loss of stability of the composite beam assembly, which is highlighted by red circles in Figure 18.

When a bolt component was used in combination with a gap/contact component with infinite stiffness (V5–V7), bolt shear failure occurred after the gap closed. The midspan deflection and connection rotation when using V5–V7 to simulate connection behavior were within 3% of one another. This indicated that the behavior of the composite beam and connection failure simulated by the component model was not sensitive to the inclusion of weld components or the different material types used in V6 (bolt material simulated as multilinear) and V7 (bolt material simulated as hysteretic). Failure of the bolts resulted in an increased rotational capacity of the connections and increased deflections compared to simulations that did not include bolt components (V1–V4). The maximum deflections of V5–V7 were within 10% of the deflection recorded right before failure during the experimental tests.

The axial forces developed in the beam ends when using V5–V7 were almost 60% greater than those approximated by Choe et al. (2019). However, when damage to the beam (i.e., local buckling at beam ends) is accounted for by limiting the amount of force transferred through the gap/contact component (V8), the axial forces are within 10% of those

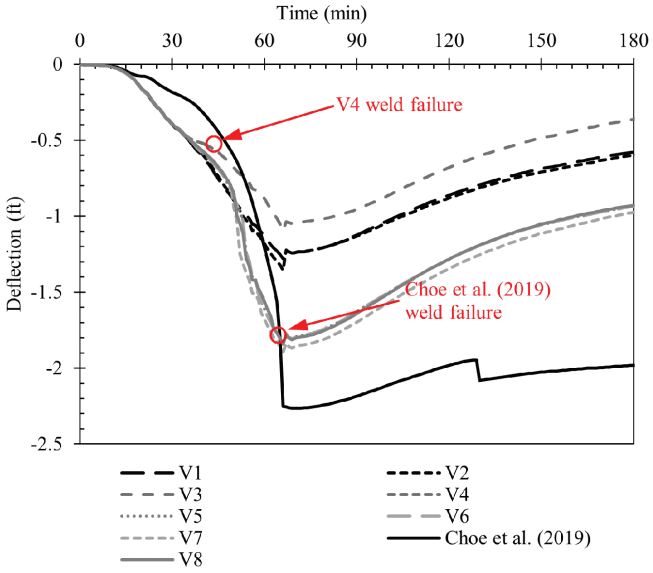

(a) VD3 deflection

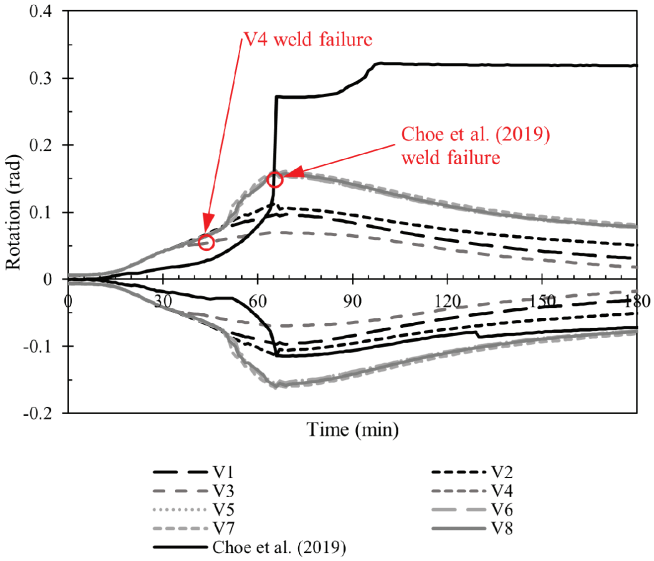

(b) connection rotations

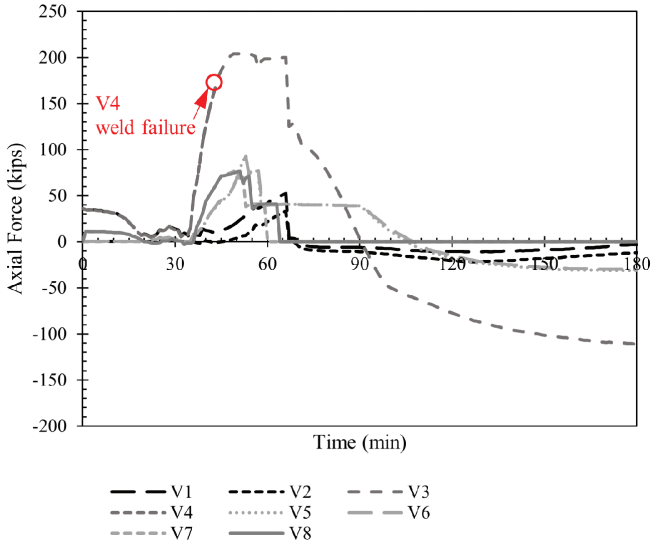

(c) sum of axial forces transferred through connecting components

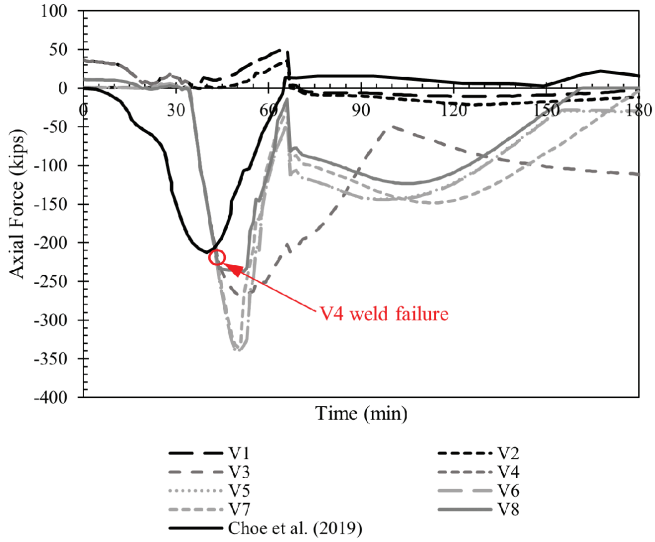

(d) axial forces at the ends of the beams

Fig. 18. Results comparison for NIST composite beam test (Choe et al., 2019).

Table 4. Summary of Results from the Simulation of the NIST Composite Beam Test (Choe et al., 2019)							
Connection Variation	Maximum Deflection (ft)	% Error Maximum Deflection	Maximum P_m (kips)	% Error Maximum P_m	Maximum P_{ce} (kips)	Maximum Connection Rotation (rad)	% Error Maximum Connection Rotation
Experimental data	–1.79	–	214	–	–	0.114	–
V1	–1.28	29%	11.0	95%	52	0.097	15%
V2	–1.36	24%	21.6	90%	33	0.114	0%
V3	–1.10	39%	267	25%	204	0.097	15%
V4	–0.55	69%	227	6%	167	0.054	52%
V5	–1.84	2%	341	59%	94	0.157	38%
V6	–1.84	3%	342	59%	92	0.157	38%
V7	–1.89	6%	335	56%	79	0.164	44%
V8	–1.84	3%	237	10%	77	0.161	41%

approximated by Choe et al. Additionally, when V8 is used, the maximum connection rotation was 40% greater than the maximum rotation recorded during experimental testing.

Discussion on Using the Component Model to Simulate Connection Behavior in a 2D Frame

Including a gap/contact component in the component model resulted in the development of large axial forces and bending moments due to beam-to-column contact. Accounting for beam damage by limiting the amount of force transferred through the gap/contact component, the component model predicted the gap/contact component to yield at a time of 44 min (4 min after local beam buckling occurred in the experimental test) and limited axial forces at the beam ends to 237 kips (10% greater than those approximated by Choe et al., 2019). Whereas, when this gap/contact component was not included, the simulation did not predict the development of compressive axial forces at the beam ends during the heating phase of the experiment (Table 4). This behavior demonstrates the importance of including the gap/contact element to simulate the fire behavior of shear tab connections and gravity beams.

Large deflections of the composite beam were able to be simulated by accounting for the ductility of the bolt components. The maximum deflections obtained when the bolt component was included in V5–V7 were within 10% of those recorded during the test. Whereas, when the bolt component was not included (V1–V4), the maximum beam deflections were within 40% of the experimental data (Table 4). However, additional research on the weld components should be performed as the OpenSees model predicted bolt shear fracture as the controlling failure mode in V2 and V5–V8, which is not consistent with the weld unzipping failure that was observed during physical testing (Choe et al., 2019). When the bolt component was not included within the component model, the OpenSees model did not predict failure of the specimen, although in cases where a weld component was included, weld fracture did occur.

SUMMARY AND CONCLUSIONS

In this study, a review of existing component models is presented and a component model for shear tab connections is developed in OpenSees. The component model is benchmarked against physical tests of isolated connections at elevated temperatures and a full-scale fire test of a long-span composite-beam assembly. Through this process, the definition of individual component behaviors, the behavior of the component model alone, and the behavior of the component model in a larger structural model were evaluated.

When modeling experimental testing of isolated connections where bolt shear was the governing failure mode, the proposed component model predicted the maximum capacity and corresponding level of ductility within 20% of the test data. When bolt tearout failure controlled, the deformations corresponding with maximum capacity were significantly higher (28% and 61%) than those recorded during experimental testing. Thus, the component model developed in OpenSees is considered to accurately approximate isolated connection behavior at elevated temperatures when subjected to axial force or a combination of axial force, shear force, and bending moment. However, additional research may be helpful in reducing modeling errors when bolt tearout is the controlling failure mode.

Using the component connection model to simulate the behavior of shear tab connections in the NIST composite

beam test (Choe et al., 2019) enabled the analytical model to simulate the development of large axial forces during the heating and cooling phases of the fire. Incorporating considerations for the ductility and damage of the connection components and structural elements was important when simulating the NIST composite beam test (Choe et al., 2019). Accounting for damage to the bolt components enabled the analytical model to simulate large beam deflections and changes in connection rotation that occurred at elevated temperatures. However, future work is necessary to account for the different failure mechanisms and associated damages of connection components loaded in tension versus compression within the model developed in this paper.

Modifications to include different compression and tension behavior would help mitigate the simulation of premature failure of connections loaded in compression. Accounting for damage to structural elements was shown to be important in approximating component failure and axial force generation. The gap/contact component definition developed in this study to account for damage to the steel beam limited forces to be within 10% of those approximated by Choe et al. (2019). Incorporating more detailed damage considerations when modeling the composite floor system may limit discrepancies between analytical and experimental results. The developed numerical modeling methodology for connections can more accurately predict isolated connection behavior at elevated temperatures when bolt shear is the governing failure mode. When simulating connection failure in the isolated connection tests (Hu and Engelhardt, 2014; Yu et al., 2009) it was shown that defining components to fail suddenly ignored the ductile failure observed at elevated temperatures (>750°F). Furthermore, to simulate the ductile failure of shear tab connections in fire it is important to define the post-peak behavior of individual components to reflect the post-peak behavior of the components observed during physical testing. Eurocode 3, Part 1-8 (CEN, 2005b) states that the deformation capacity of welds should not be considered; however, the test results of Choe et al. (2019) demonstrate that importance of weld deformation capacity throughout a fire condition as the weld deformation capacity is potentially exceeded prior to the force capacity of the welds, initiating unzipping of the weld. Further research and development of weld component models are suggested such that this damage and failure can be simulated throughout a fire scenario.

ACKNOWLEDGMENTS

This research was funded by the Pacific Earthquake Engineering Research (PEER) Center and the American Institute of Steel Construction (AISC). Any opinions, findings, and conclusions are those of the author and do not necessarily reflect the views of the sponsors. Special thanks and acknowledgement to Dr. Kevin Mackie, professor at the University of Central Florida, and Dr. Michael Scott, professor at Oregon State University, for their support of this research.

REFERENCES

Agarwal, A. (2011), "Stability Behavior of Steel Building Structures in Fire Conditions," Ph.D. dissertation, Purdue University, West Lafayette, Ind.

Agarwal, A. and Varma, A.H. (2014), "Fire Induced Progressive Collapse of Steel Building Structures: The Role of Interior Gravity Columns," *Engineering Structures*, Vol. 58, pp. 129–140.

AISC (2016), *Specification for Structural Steel Buildings,* ANSI/AISC 360-16, American Institute for Steel Construction, Chicago, Ill.

Burgess, I., Davison, J.B., Dong, G., and Huang, S. (2012), "The Role of Connections in the Response of Steel Frames to Fire," *Structural Engineering International,* Vol. 22, No. 4, pp. 449–461.

CEN (2005a), *Eurocode 3: Design of Steel Structures—Part 1–2: General Rules—Structural Fire Design*, European Committee of Standardization, Brussels.

CEN (2005b), *Eurocode 3: Design of Steel Structures—Part 1–8: Design of Joints,* European Committee of Standardization, Brussels.

Choe, L., Ramesh S., Grosshandler, W., Hoehler, M., Seif, M.S., Gross, J., and Bundy, M. (2019), "Behavior and Limit States of Long-Span Composite Floor Beams with Simple Shear Connections Subject to Compartment Fires: Experimental Evaluation," *Journal of Structural Engineering,* Vol. 146, No. 6.

FEMA (2000), "State of the Art Report on Connection Performance," FEMA-355D*,* Federal Emergency Management Agency, Washington, D.C.

Fischer, E.C., Varma, A.H., and Qiaqia Z. (2018), "Experimental Evaluation of Single-Bolted Lap Splice Joints at Elevated Temperatures," *Journal of Structural Engineering*, Vol. 144, No. 1.

Gordon, J.A. (2022), "Advancements Toward the Simulation of Steel Structures in Fire in OpenSees," Master's Thesis, Oregon State University, Corvallis, Ore.

Hajjar, M., Hantouche E.G., and El Ghor, A.H. (2019), "Shear Tab Connection with Composite Beam Subjected to Transient-State Fire Temperatures: A Rational Model for Design," *Journal of Structural Fire Engineering.* Ahead-of-print.

Hu, G. and Engelhardt, M.D. (2014), "Experimental Investigation of Steel Single Plate Beam End Connections at Elevated Temperatures," *Engineering Structures*, Vol. 58, pp. 141–151.

Hu, Y., Davison, B., and Burgess, I. (2009), "Component Modelling of Flexible End-Plate Connections in Fire," *International Journal of Steel Structures*, Vol. 9, No. 1, pp. 1–15.

Jiang, J. and Usmani, A. (2013), "Modeling of Steel Frame Structures in Fire Using OpenSees." *Computer and Structures*, Vol. 118, pp. 90–99.

Khorsani, N.E., Garlock M.E.M., and Quiel, S.E. (2015), "Modeling Steel Structures in OpenSees: Enhancements for Fire and Multi-Hazard Probabilistic Analyses," *Computers and Structures*, Vol. 157, pp. 218–231.

Koduru, S.D. and Driver, R.G. (2014), "Generalized Component-Based Model for Shear Tab Connections," *Journal of Structural Engineering*, Vol. 140, No. 2.

Kurikova, M., Vild, M., Frantisek W., Jehlicka, P., Kabelac, J., and Taras, A. (2022), "Fillet Weld Model for Component-Based Finite Element Method," AISC–EECS Workshop on Connections in Steel Structures, Coimbra, Portugal.

Lesik, D.F. and Kennedy, D.J.L. (1988), "Ultimate Strength of Eccentrically Loaded Fillet Welded Connections," *Structural Engineering,* Report 159, University of Alberta, Edmonton, AB, Canada.

Liu T.C.H., Fahad, M.K., and Davies, J.M. (2002), "Experimental Investigation of Behaviour of Axially Restrained Steel Beams in Fire," *Journal of Constructional Steel Research*, Vol. 58, pp. 1,211–1,230.

Liu Y., Huang S., and Burgess, I. (2019), "Investigation of a Steel Connection to Accommodate Ductility Demand of Beams in Fire," *Journal of Constructional Steel Research*, Vol. 157, pp. 182–197.

Maddalozzo, W. and Fischer, E.C. (2020), "Post-Earthquake Fire Performance of Steel Buildings," *17th World Conference on Earthquake Engineering*, Sendai, Japan, September 13–18.

Mazzoni, S., McKenna, F., Scott, M.H., and Fenves, G.L. (2006), *OpenSees Command Language Manual*, University of California, Berkeley, http://opensees.berkeley.edu/manuals/usermanual.

Peixoto, R.M., Seif, M.S., and Viera, L.C. (2017), "Double-Shear Tests of High-Strength Structural Bolts at Elevated Temperatures," *Fire Safety Journal*, Vol. 94, No. 8-21.

Rex, C.O. and Easterling, S.W. (2003), "Behavior and Modeling of a Bolt Bearing on a Single Plate," *Journal of Structural Engineering*, Vol. 129, No. 6, pp. 792–800.

Richard, R.M. and Abbot, B.J. (1975), "Versatile Elastic-Plastic Stress-Strain Formulation," *Journal of Structural Engineering*, Vol. 101, pp. 511–515.

Sadek, F., El-Tawil, S., and Lew, H.S. (2008), "Robustness of Composite Floor Systems with Shear Connections: Modeling, Simulation, and Evaluation," *Journal of Structural Engineering*, Vol. 134, No. 11, pp. 1,717–1,725.

Sarraj, M. (2007), "The Behavior of Steel Fin Plate Connections in Fire," Ph.D. dissertation, The University of Sheffield, Sheffield, United Kingdom.

Seif, M., Weigand, J., Main, J., Peixoto R., and Vieira L. (2018), "Shear Behavior of High-Strength Bolts at Elevated Temperatures: Testing and Formulation of Reduced-Order Model," NIST Technical Note 1978.

Silva, L.S., Santiago, A., and Real, P.V. (2001), "A Component Model for the Behavior of Steel Joints at Elevated Temperatures," *Journal of Constructional Steel Research,* Vol. 57, pp. 1,169–1,195.

Smith, M. (2009), ABAQUS/Standard User's Manual, Version 6.9.

Taib, M. and Burgess I.W. (2011), "A Component-Based Model for Fin-Plate Connections in Fire," *Application of Structural Fire Engineering*, Vol. 4, pp. 113–122.

Wald, F., Strejcek, M., and Ticha A. (2006), "On Bolted Connection with Intumescent Coatings," *Proceedings of the Fourth International Workshop "Structures in Fire—SiF*, Aveiro, Portugal, pp. 371–322.

Walls, R.S., Vilijoen, C., and Clereq, H. (2018), "Analysis of Structures in Fire as Simplified Skeletal Frames Using Customized Beam Finite Element," *Fire Technology*, Vol. 54, No. 6, pp. 1,655–1,682.

Weigand, J.M. (2017), "Component-Based Model for Single-Plate Shear Connections with Pretension and Pinched Hysteresis," *Journal of Structural Engineering*, Vol. 143, No. 2.

Weigand, J.M., Peixoto, R., Vieira Jr., L.C.M., Main, J.A., and Seif, M. (2018), "An Empirical Component-Based Model for High-Strength Bolts at Elevated Temperatures," *Journal of Constructional Steel Research*, Vol. 147, pp. 87–102.

Whyte, C.A., Mackie, K.R., and Stojadinovic (2016), "Hybrid Simulation of Thermomechanical Structural Response," *Journal of Structural Engineering*, Vol. 142, No. 2.

Xie, B., Hou, J., Xu, Z., and Dan, M. (2018a), "Component-Based Model of Fin Plate Connections Exposed to Fire—Part I: Plate in Bearing Component," *Journal of Constructional Steel Research*, Vol. 149, pp. 1–13.

Xie, B., Hou, J., Xu, Z., and Dan, M. (2018b), "Component-Based Model of Fin Plate Connections Exposed to Fire—Part II: Establishing of the Component-Based Model," *Journal of Constructional Steel Research*, Vol. 149, pp. 218–231.

Yu, H., Burgess, I.W., Davison, J.B., and Plank, R.J. (2009), "Experimental Investigation of the Behavior of Fin Plate Connections in Fire," *Journal of Constructional Steel Research*, Vol. 65, pp. 723–736.

Application of AISC *Specification* Requirements for Second-Order Analysis and Stability Design

Rafael Sabelli, Allen Adams, and David Landis

ABSTRACT

Design for stability is inherent in the proper design of every steel structure. As such, every engineer using the AISC *Specification* (2022) must understand the requirements for stability design and how their own methods (including computer analyses) address the relevant considerations. This discussion provides specific, concise guidance on the application of AISC *Specification* requirements for stability design and second-order analysis for the practicing engineer.

Keywords: stability, direct analysis method, effective length, first-order analysis.

INTRODUCTION

This paper provides the practicing engineer a specific yet concise guide to the relationship between design for stability and second-order analysis as presented in the AISC *Specification for Structural Steel Buildings* (AISC, 2022), hereafter referred to as the AISC *Specification*. In their work on AISC committees and in practice, the authors have observed that the current guidance in Part 2 of the AISC *Steel Construction Manual* (AISC, 2023) does not provide specific guidance on the AISC *Specification* requirements for second-order analysis. While there is a very detailed treatment in AISC Design Guide 28, *Stability Design of Steel Buildings* (Griffis and White, 2013), this goes beyond the needs of most practicing engineers and typical projects. Accordingly, the authors have prepared a discussion of design for stability with specific guidance on the application of second-order analysis, expanding on the treatment in the AISC *Steel Construction Manual*.

The paper includes a discussion of design for stability and of second-order analysis, as well as tables for approximate second-order analysis for P-Δ effects. Additionally, there is a glossary of terms, a diagrammatic presentation of methods of second-order analysis, and a design example.

Rafael Sabelli, Senior Principal, Director of Seismic Design, Walter P Moore, San Francisco, Calif. Email: rsabelli@walterpmoore.com (corresponding)

Allen Adams, Chief Structural Engineer, Bentley Systems, Oceanside, Calif. Email: allen.adams@bentley.com

David Landis, Managing Principal, Walter P Moore, Kansas City, Mo. Email: dlandis@walterpmoore.com

Paper No. 2022-08

REQUIRED STRENGTH, DESIGN FOR STABILITY, EFFECTIVE LENGTH, AND SECOND-ORDER EFFECTS

In the AISC *Specification*, reliable performance is achieved by ensuring that the available strength of members and connections equals or exceeds the required strength. As discussed in Chapter C of the AISC *Specification*, it is essential to this method that stability be provided for the structure as a whole and each of its elements. Stability considerations can affect either the required strength (demand) or the available strength (capacity), or both, depending on the method of design for stability.

While many computer analysis programs have the capability to implement relevant stability-design requirements (including second-order analysis), it is imperative that the engineer understand which requirements are implemented (and how), as well as the limits of applicability of each method, to ensure that the design is appropriate. This paper includes tables that provide specific guidance on applicability limits and requirements for different methods of stability design and second-order analysis. This information can guide effective design for stability using either computer or hand analysis. Additionally, tables provided in this paper can be used in approximate manual calculations of second-order effects to provide higher confidence that a computer program's second-order analysis has been properly implemented.

Design for Stability

The five general considerations for stability design are listed in AISC *Specification* Section C1. These are consideration of:

- Flexural, shear, and axial member deformations, and all other component and connection deformations that contribute to the displacements of the structure.

Table 1. Methods of Addressing Stability-Design Considerations				
Stability-Design Consideration		**Direct Analysis Method**	**Effective Length Method**	**First-Order Method**
(a) All deformations that contribute to the displacements of the structure		Analysis of model that includes all significant sources of flexibility		
(b) Second-order effects	System P-Δ effects (including *P*-δ effect on P-Δ)	Second-order analysis		Additional lateral load
	Member *P*-δ effects	B_1 amplifier or inclusion of member *P*-δ effect in second-order analysis		B_1 amplifier
(c) Geometric imperfections (system)	Effect on structural response	Minimum notional load or modeling of imperfections	Minimum notional load	
(c) Geometric imperfections (member),	Effect on structural response	Stiffness reduction	Effective length factor	Additional lateral load
(d) Stiffness reduction due to inelasticity, and		Member strength formulae		
(e) Uncertainty in strength and stiffness	Effect on member strength			

- Second-order effects (including both *P*-Δ and *P*-δ effects).
- Geometric imperfections.
- Stiffness reductions due to inelasticity—including the effect of partial yielding of the cross section, which may be accentuated by the presence of residual stresses.
- Uncertainty in system, member, and connection strength and stiffness.

The AISC *Specification* allows any rational method to address these stability considerations, including advanced analysis per Appendix 1. The AISC *Specification* also provides three simpler approaches: the direct analysis method, the effective length method, and the first-order analysis method. Table 1 shows how the direct analysis method, the effective length method, and the first-order method address each of the five general considerations for stability design. (Detailed requirements are presented in Table 2.)

The differences in how each of the three methods addresses stability considerations are as follows:

- The *direct analysis method*, presented in AISC *Specification* Chapter C (Section C2), is the most comprehensive and versatile of the three methods in incorporating the stability-design considerations into determination of required strength. This is achieved using notional loads (or modeling system imperfections), reduced stiffness, and a second-order analysis. The effects of member out-of-straightness and residual stresses on member strength are addressed in the determination of the available strength, through the column design strength formulas using an effective length equal to the unbraced length (i.e., $K = 1.0$) for all framing systems; lesser values of K can be justified by analysis.
- The *effective length method*, presented in AISC *Specification* Appendix 7 (Section 7.2), incorporates most of the stability considerations (such as system imperfections and second-order effects) into the determination of required strength. The effects of member out-of-straightness and residual stresses on member strength, and the effects of member out-of-straightness and residual stresses on structure stiffness, are dealt with in the determination of available strength through the column design strength formulas using effective lengths that may exceed member lengths (i.e., $K \geq 1.0$). Engineers should note that the use of reduced column available strength addresses these effects on the column (as opposed to the use of increased column required strengths in the direct analysis method) but does not address the corresponding load effects on beams and connections. The AISC *Specification* permits $K = 1.0$ for braced-frame and shear-wall structures. For moment-frame structures and mixed systems, $K = 1.0$ may be used when the ratio of second-order drift to first-order drift is less than or equal to 1.1. For moment-frame structures and mixed systems in which the second-order to first-order drift ratio exceeds 1.1, K is determined in accordance with AISC *Specification* Section 7.2. Effective length factors are determined by elastic buckling analysis, effective-length equations, or, more commonly, use of

alignment charts such as Figures C-A-7.1 and C-A-7.2 in the Commentary to the AISC *Specification* (provided that the associated assumptions are satisfied). Effective length factors, K, must be modified to K_2 to address the effect of gravity-only columns (often referred to as leaning columns), as described in Geschwindner (2002) and the Commentary to AISC *Specification* Section 7.2. Use of the effective length factor K_2 is distinct from consideration of the effects of leaning-column loads in a second-order analysis: the former addresses the vertical load being stabilized against sidesway buckling, and the latter addresses lateral-load amplification due to P-Δ stiffness reduction. Stability in gravity-only load combinations is addressed by means of a minimum lateral load.

- The *first-order analysis method*, presented in AISC *Specification* Appendix 7 (Section 7.3), is a conservative simplification of the direct analysis method, incorporating the stability-design considerations into determination of required strength. In lieu of a second-order analysis with reduced stiffness, however, this method utilizes a first-order analysis, with system-level stability-design requirements addressed through the application of an additional lateral load proportional to the story gravity load and corresponding either to the lateral story drift or to a minimum based on initial imperfections. (For convenience, the drift limit for each load combination may be used to conservatively determine the required additional lateral load in lieu of a calculated lateral drift.) This additional lateral load corresponds to the combined effects of the second-order story-drift (P-Δ) and member imperfections for the most severe condition possible within the limitations for this method (Griffis and White, 2013). There are significant limits on application of this method: a limit on moment-frame column axial stress to preclude any effect of column inelasticity on stability and a limit on axial forces in moment-frame beams to preclude conditions where beam P-δ effects could affect the column. (Both of these limits are evaluated with LRFD loads or with ASD loads amplified by $\alpha = 1.6$.) While a second-order analysis is not required, the procedure is only permitted if the second-order story-drift amplification does not exceed 1.5; this may be demonstrated using an approximate second-order analysis such as determining the B_2 factor per AISC *Specification* Appendix 8 (and tabulated in Tables 4 and 5). As only a first-order analysis is required, the effect of gravity sway is not addressed, and therefore, nominally vertical columns are required. A limit on B_2 lower than 1.5 should be considered for systems with significant gravity sway. Additionally, member P-δ effects must be addressed by applying the amplification factor B_1 to total moments per Appendix 7, Section 7.3.2(b). The required strengths are taken as the forces and moments obtained from the analysis and the effective length factor is $K = 1.0$.

With higher second-order effects, there is increased sensitivity of the response to small changes or uncertainties in vertical loading or lateral stiffness, amplifying the inaccuracies resulting from simplifications inherent in each stability-design method. For this reason, the effective length method and the first-order analysis method are limited to systems in which the magnitude of second-order story-drift amplification does not exceed 1.5. Higher second-order story-drift amplification is permitted for the direct analysis method; the commentary to Section C1 suggests a limit of 2.5 (determined with reduced stiffness, corresponding to a value of 1.9 determined with nominal properties).

Table 2 presents a comparison of the requirements and limitations for the direct analysis method, the effective length method, and the first-order analysis method, including the "simplified method" (an adaptation of the effective-length method addressed later in this discussion).

Methods of Second-Order Analysis

Second-order effects are the additional forces and displacements due to applied loads as the structure transitions from the undeformed to the deformed geometry such that there is equilibrium between internal forces and external loads acting in their displaced positions. These effects can be categorized as P-Δ effects on the structure lateral displacement and corresponding internal forces, P-δ effects on member flexural forces, and P-δ influence on structure P-Δ. See AISC *Specification* Commentary to Section C2.1 and AISC Design Guide 28 Appendix Section A.2.1 for more discussion of P-Δ and P-δ effects.

Each of the stability-design methods in Table 2 requires a determination of second-order effects: The direct analysis method and the effective length method both require a second-order analysis, and the first-order analysis method requires determination that the magnitude of second-order amplification does not exceed 1.5. The Commentary to AISC *Specification* Chapter C provides guidance on methods of second-order analysis and presents second-order analysis results for several benchmark problems to facilitate checking the adequacy of analysis methods and computer programs. Ziemian and Ziemian provide multiple benchmark frames (2021). See Griffis and White for guidance on the use of benchmark problems (2013).

Table 3 summarizes AISC *Specification* requirements and recommendations for three methods of second-order analysis: general second-order analysis that captures both P-Δ and P-δ effects, P-Δ-only second-order analysis, and an approximate method of second-order analysis by means of amplified first-order analysis, as described in the following.

Table 2. Summary Comparison of Methods for Elastic Stability Design

	Direct Analysis Method		Effective Length Method		First-Order Analysis Method
	General	Limited	General	Simplified	
Limitations on Use	None[a], [b]	Nominally Vertical columns[a]	Nominally vertical columns $\Delta_{2nd}/\Delta_{1st} \le 1.5$[c]	Nominally vertical columns $\Delta_{2nd}/\Delta_{1st} \le 1.5$[c] $B_1 \le B_2$[d]	Nominally vertical columns $\Delta_{2nd}/\Delta_{1st} \le 1.5$[c] $\alpha P_r/P_{ns} \le 0.5$[e] Beam $\alpha P_r/P_e \le 0.08$[e]
Analysis Type	Second-order elastic	Second-order elastic or amplified first-order elastic[f]		Amplified first-order elastic[f]	First-order elastic[g]
Geometry of Structure	Initial imperfections	Undeformed geometry (with notional loads) or initial imperfections[h]		Undeformed geometry	
Minimum or Additional Lateral Loads	None	Minimum[i]; a times 0.2% of the story gravity load[e], [h]			Additive; greater of 0.42% or $2.1\alpha(\Delta_{1st}/L) \times$ story gravity load[e], [j]
Member Stiffnesses	0.8*EA* and $0.8\tau_b EI$[k]		Nominal *EA* and *EI*		
Column Available Strength[l]	K = 1 for all frames		*K* = 1 for braced frames and shear-wall structures. *K* determined from sidesway buckling analysis, from effective-length equations, or from nomograph and adjusted to K_2 for moment frames[m]		*K* = 1 for all frames
AISC *Specification* Reference	Chapter C		Appendix 7, Section 7.2		Appendix 7, Section 7.3

[a] The commentary to AISC *Specification* Section C1 recommends that $\Delta_{2nd}/\Delta_{1st} \le 2.5$ using reduced stiffness.

[b] AISC *Specification* Section C2.2b requires that system imperfections be modeled explicitly for systems with sloped columns.

[c] $\Delta_{2nd}/\Delta_{1st}$ is the ratio of maximum second-order story drift to maximum first-order story drift, which can be taken equal to B_2 per AISC *Specification* Appendix 8. (The B_2 factor may be determined using Table 4 or Table 5.) $\Delta_{2nd}/\Delta_{1st}$ is determined using LRFD load combinations or a multiple of 1.6 times ASD load combinations for the vertical load.

[d] The Simplified Method is limited to systems for which the value of the B_1 amplifier never exceeds that of the B_2 amplifier.

[e] For ASD, $\alpha = 1.6$. Amplification by α and determination of appropriate ASD-level member-design forces are discussed under "Methods of Second-Order Analysis."

[f] See Table 3 for methods of second-order analysis and associated requirements.

[g] Amplification of non-sway moments due to member curvature is required; this is achieved by applying the amplification factor B_1 to total moments per Appendix 7, Section 7.3.2(b).

[h] Notional loads are computed with appropriate load factors for the combinations being considered. Direct modeling of imperfections may be used in lieu of notional loads for the direct analysis method per AISC Specification Section C2.2a.

[i] For the direct analysis method, the notional load is additive if $\Delta_{2nd}/\Delta_{1st} > 1.7$ using reduced stiffness or $\Delta_{2nd}/\Delta_{1st} > 1.5$ using nominal properties.

[j] The maximum value of the drift ratio Δ/L for all stories shall be used. Δ is the first-order interstory drift due to the LRFD or ASD load combination, as applicable. Where Δ varies over the plan area of the structure, Δ shall be the average drift weighted in proportion to vertical load or, conservatively, the maximum drift.

[k] The stiffness-reduction factor τ_b is a function of $\alpha P_r/P_{ns}$; see AISC *Specification* Equation C2-2b.

[l] Available strength is calculated in accordance with the provisions of Chapters D through K, as applicable, with the effective length based on the value of *K* listed in the table.

[m] $K = 1$ is permitted if $\Delta_{2nd}/\Delta_{1st} \le 1.1$.

- A *general second-order analysis* is an analysis that establishes equilibrium between internal and external forces in the deformed state and meets the requirements of AISC *Specification* Section C2.1 to capture both *P*-Δ and *P*-δ effects. Such analyses are typically iterative incremental analyses that employ either stability functions or geometric stiffness matrices that update coordinate locations with each loading increment. Each load combination therefore requires its own iterative analysis and superposition is not appropriate. Most computer structural analysis programs that support iterative analysis are capable of capturing *P*-δ effects by subdividing members into segments such that the deformed shape is reasonably well represented (White

and Hajjar, 1991). If this subdivision is not automated, the engineer must explicitly divide these elements into segments when creating the analytical model. White et al. (2021) provide specific guidance for the number of elements required to accurately capture P-δ effects for various conditions, including for both prismatic and non-prismatic members (see also Griffis and White, 2013). If such segmentation is not employed, member P-δ effects may be addressed outside of the analysis by amplifying member moments as discussed below, subject to the limitations in AISC *Specification* Section C2.1(b) for a P-Δ-only analysis.

- A *P-Δ-only second-order analysis* is permitted by AISC *Specification* Section C2.1(b), which allows neglecting the influence of P-δ on P-Δ in the analysis subject to certain limitations.[1] (See Table 3.) Within these limits, the influence of P-δ on P-Δ is negligible, increasing forces no more than 1.0% and displacements by no more than 3.2% (Sabelli and Griffis, 2021). However, P-δ effects on member moments must still be considered; this is typically done by means of the B_1 amplifier from Appendix 8 on the member moments from the P-Δ-only second-order analysis. Although the iterative method may be used in a P-Δ-only second-order analysis, the noniterative geometric stiffness method is more common and more convenient. In the non-iterative method, the geometric stiffness matrix is modified based on a single defined vertical-load combination, permitting superposition of the results from analyses of separate load cases in factored load combinations. Some error may result from the difference between the vertical load combination used for stiffness modification and the vertical load combination used in superposition. Greater vertical loads results in lower stiffness, and thus greater second-order effects, so the largest vertical load combination should be used to determine the stiffness when used for a group of load combinations handled by superposition. For example, the engineer may establish one geometric-stiffness model to be used for all load combinations using the largest vertical load combination, or the engineer may establish one geometric-stiffness model to be used for gravity-only load combinations using the largest vertical load combination, and a different geometric-stiffness model to be used with lateral load combinations, for which the factors on the gravity loads are smaller and hence the magnitude of the vertical load is smaller.
- An *approximate second-order analysis* addresses P-Δ and P-δ effects by means of amplifiers on first-order analysis forces, as defined in AISC *Specification* Appendix 8. The B_1 amplifier addresses P-δ effects on member non-sway moments. The B_2 amplifier addresses P-Δ effects on members and the system, including the influence of P-δ on P-Δ amplification. B_2 is therefore applicable to all member and connection forces resulting from lateral loading or translation (including member shear and connection forces). The influence of P-δ on P-Δ amplification is typically addressed by means of a coefficient R_M in AISC *Specification* Equation A-8-7 for B_2; where AISC *Specification* Section C2.1(b) allows neglecting such effects, this coefficient may be taken as 1.0. Superposition of the results of analyses may utilize the B_2 amplifier specific to each vertical load combination, or a single B_2 factor corresponding to the largest vertical load combination of a group of load combinations may be applied for convenience. For example, the engineer may calculate one B_2 amplifier to be used with gravity-only load combinations and a (lower) B_2 amplifier to be used with lateral-load combinations. The B_2 amplifier may also be applied to the first-order displacement to approximate the second-order displacement; this has less than 2% error for $B_2 \leq 1.5$ (Sabelli and Griffis, 2021).

Additional discussion of these three methods can be found in Appendix A.

For asymmetrical geometry or loading, gravity forces may induce lateral sway. This gravity-induced lateral sway is subject to the same amplification due to second-order effects as is the sway from lateral loads. While this effect is captured directly in second-order analyses that include the gravity load, amplified first-order analyses require separation of translation and no-translation forces to correctly capture this effect, as discussed in the Commentary to AISC *Specification* Appendix 8. Such separation of forces is unnecessary when the gravity-induced sway is negligible compared to the lateral-load-induced sway, such as for the common case of a symmetrical structure with symmetrical vertical loading.

The full-story gravity load must always be included in the determination of P-Δ effects. This includes all forces coming from levels above and from floor and cladding loads at the current level, supported by both the gravity system (the so-called leaning gravity columns and walls, including laterally supported cladding) and the lateral force-resisting system. (The vertical seismic load effect

[1] ASCE/SEI 7 (2022), Section 12.8.7, provides a method of accounting for P-Δ effects that consists of amplifying forces and displacements by $1/(1-\theta)$, where θ is the stability coefficient. (Using AISC symbols, $\theta = P_{story}\Delta_H/HL$.) This method does not account for P-δ influence on P-Δ, and, as such, it only satisfies the requirements of the AISC *Specification* within the range for which AISC *Specification* Section C2.1(b) allows P-Δ-only second-order analysis. Furthermore, θ in ASCE/SEI 7 utilizes a different vertical load than the strength load combinations. The amplifier $1/(1-\theta)$ is identical to the B_2 amplifier for conditions in which there is no P-δ influence on P-Δ (i.e, $R_M = 1.0$) if the same vertical loads are used for both amplifiers.

Table 3. Summary Comparison of Methods for Second-Order Analysis for *P*-Δ and *P*-δ Effects			
Type	**Second-Order Analysis**		**Approximate Second-Order Analysis**
Description	**General Second-Order Analysis**	***P*-Δ-Only Second-Order Analysis**	**Amplified First-Order Analysis**
Limitations on use in AISC *Specification*	None	Nominally vertical columns $\Delta_{2nd}/\Delta_{1st} \le 1.5$[a], [b] $P_{mf}/P_{story} \le 1/3$[c]	Nominally vertical columns
Recommended limit	None	$B_1 \le 1.2$ for members having significant effect on overall structural response[d]	
P-δ effect on members	Addressed within analysis by subdividing members	Addressed through B_1 amplifier on member moment	
P-δ influence on *P*-Δ	Addressed within analysis by subdividing members	Not directly addressed[d]	Addressed by the R_M factor or sidesway buckling analysis[d]
Method[e]	Incremental iterative analysis[e]	Noniterative geometric stiffness	B_1 amplifier on member moments; B_2 amplifier on lateral-load effects[e], [f]
Story gravity load[g]	Included in the analysis	Included in the determination of the geometric stiffness	Included in the calculation of the B_2 amplifier
Superposition of analysis results	Not applicable	Applicable with appropriate vertical load combination groupings	
AISC *Specification* reference	C2.1		C2.1; Appendix 8
Amplification of gravity-induced sway	Directly addressed in the analysis		Addressed by separate no-translation and translation analyses[h]
P-Δ effect on system	Directly addressed in the second-order analysis		Addressed through B_2 amplifier on lateral-translation forces
Second-order drift Δ_2	Directly determined in the second-order analysis		Approximated as the first-order drift amplified by B_2[a]
Factor for ASD (α)	1.6 for all loads	1.6 (gravity loads for determination of geometric stiffness reduction and axial forces for determination of B_1)	1.6 (gravity loads [αP_{story}] for determination of B_2 and axial forces for determination of B_1)

[a] $\Delta_{2nd}/\Delta_{1st}$ is the ratio of maximum second-order story drift to maximum first-order story drift, which can be taken equal to B_2 per AISC *Specification* Appendix 8. (The B_2 factor may be determined using Table 4 or Table 5.) $\Delta_{2nd}/\Delta_{1st}$ is determined using LRFD load combinations or a multiple of 1.6 times ASD load combinations.

[b] The limit of $\Delta_{2nd}/\Delta_{1st} \le 1.5$ for an analysis using full stiffness properties corresponds to $\Delta_{2nd}/\Delta_{1st} \le 1.7$ for a reduced-stiffness analysis as required for the direct analysis method.

[c] P_{mf}/P_{story} is the ratio of gravity load supported by columns that are part of moment-resisting frames in the direction of translation being considered to the total gravity load on the story.

[d] See AISC *Specification* Commentary Section C2.1, "Effect of Neglecting *P*-δ" and commentary to Appendix 8.

[e] Note that incremental iterative analysis and amplified first-order analysis can be utilized in a *P*-Δ-only second-order analysis. A *P*-Δ-only second-order analysis is often performed using the geometric-stiffness matrix method

[f] The elastic critical buckling strength may be determined from AISC *Specification* Equation A-8-7 or from a sidesway buckling analysis. B_2 factors may be obtained directly from Table 4 or Table 5.

[g] Story gravity load includes loading from levels above and on nonframe columns and walls, and the weight of wall panels laterally supported by the lateral force-resisting system. It need not include the vertical component of the seismic load.

[h] Separate no-translation and translation analyses are not required for the simplified method discussed later in this section.

need not be included.) Computer models of the lateral system should account for leaning columns to capture the P-Δ effects of gravity load not on the frame columns. For iterative second-order analysis, these leaning-columns deform laterally with the lateral force-resisting system, and their thrust adds to the lateral load at the equilibrium condition. For noniterative geometric-stiffness second-order analysis, the full-story gravity load must be included in the determination of the geometric stiffness matrix; P-Δ effects from the gravity loads on leaning columns are adequately represented in that method. For the approximate second-order analysis, the full story gravity load must be included in the calculation of the B_2 amplifier.

Typically, large areas of the building are considered in calculating P_{story}, and live-load reduction is permitted based on the tributary area. These reductions may be implemented relatively easily in a geometric-stiffness-matrix analysis or in computing a B_2 amplifier. For incremental second-order analysis, Ziemian and McGuire (1992) provide a method of using compensating forces at columns to achieve the appropriate reductions at the system level without affecting member-level forces.

In general, representing the gravity load using a single mass with a single displacement is adequate for two-dimensional analyses but will not capture amplification of plan torsion or the deformation of a nonrigid diaphragm. For iterative second-order analysis, distributed leaning columns corresponding to the actual column locations is preferred for buildings in which torsional movement (plan rotation) or diaphragm deformation may be significant (White and Hajjar, 1991). For the geometric stiffness method, the effects of plan torsion and diaphragm flexibility are captured if the stiffness modifications are based on the entire story mass and mass moment of inertia, not merely on the mass supported by the lateral frames; it is not necessary to model a column or set of columns to represent the leaning columns as long as the total gravity load and spatial gravity load distribution are accurately modeled. For approximate second-order analysis, amplification of plan torsion or the deformation of a nonrigid diaphragm can be bounded by using the maximum value of drift or by adjustments to the drift [Flores et al., 2018; ASCE, 2022 (Commentary to section 12.8.7)].

Both P-Δ effects and P-δ effects are nonlinear with respect to loading and thus cannot be scaled directly between LRFD and ASD. In the AISC *Specification*, adequate reliability is based on LRFD-level loading, with ASD providing similar reliability by adjustment of the action with nonlinear effect. As P-Δ effects are nonlinear with respect to vertical loads on the system, ASD vertical loads must be amplified with the load-adjustment factor α, to which the AISC *Specification* assigns a value of 1.6 for ASD [Section C2.1(d) and Appendix 8, Section 8.1.2]. Similarly, P-δ effects in members subject to flexure are nonlinear with respect to axial compressive force, which are amplified by this same factor for ASD design. Engineers using ASD should be attuned to having these effects properly captured with the application of α where required. Commentary to Section B3 discusses the differences between ASD and LRFD required strength under lateral load combinations.

When using an iterative second-order analysis for ASD design, AISC *Specification* Section C2.1(d) requires amplification of all loads (gravity, lateral, etc.) by α, prior to performing the second-order analysis. (Notional loads, which are already amplified by α in Equation C2-1, should not be amplified a second time.) Subsequent to the iterative second-order analysis, the member forces determined using this method are divided by α to be at ASD level.

Amplification of all ASD loads by α is unnecessary (and generally cumbersome) for the geometric-stiffness method or the approximate second-order analysis method. Instead, for these methods, α is typically only applied in the determination of the second-order effect; the loads used in the analysis are not amplified by α, nor are the member forces from that analysis subsequently divided by α. (The factor is applied for certain checks; see Table 2.) For ASD design using the geometric-stiffness method, the vertical loads used in the calculation of the stiffness reduction must be amplified by α; the resulting reduced stiffness is used with ASD-level forces. Similarly, P_{story} must be amplified by α for calculation of the B_2 amplification factor for approximate second-order analysis; this factor is applied to ASD-level load effects. For both the methods, in determining the B_1 amplification factor for P-δ magnification of member moment when using ASD, Equation A-8-3 amplifies axial compressive forces by α, resulting in the appropriate magnification of the ASD moment, which is combined with ASD-level axial forces using Chapter H of the AISC *Specification*.

The drift is determined directly in second-order analysis. For the amplified first-order method, the second-order drift may be approximated as the drift from a first-order analysis amplified by B_2 from Equation A-8-7 for the load combination being considered per AISC *Specification* Appendix 7, Section 7.2.1. See also LeMessurier (1977), Griffis and White (2013), and Sabelli and Griffis (2021) for drift amplification.

B_2 Amplifier for P-Δ Effects for Approximate Second-Order Analysis

As discussed earlier, approximate second-order analysis may be performed by amplifying forces from a first-order analysis for P-Δ and P-δ effects using amplifiers B_1 and B_2. Such an approximate second-order analysis may be used with the direct analysis method or the effective length method (including the simplified method discussed later in

this section); it may also be used to confirm the applicability of the first-order-analysis method.

In such an analysis, the B_2 amplifier addresses P-Δ effects on the system, including the P-δ influence on structure P-Δ. The system stiffness is integral to the B_2 amplifier, and thus, the calculated drift or the drift limit may be used in its determination.

Determination of the $\mathbf{B_2}$ *Amplifier Using First-Order Drift*

The B_2 amplifier can be defined in terms of first-order system lateral stiffness (H/Δ_H), P-Δ stiffness reduction ($\alpha P_{story}/L$), and P-δ influence on structure P-Δ (R_M) by combining AISC *Specification* Equations A-8-6 and A-8-7:

$$B_2 = \frac{1}{1-\left(\frac{\alpha P_{story}}{R_M H}\right)\left(\frac{\Delta_H}{L}\right)} \tag{1}$$

where

H = total story shear, kips (N)

L = height of story, in. (mm)

P_{story} = total vertical load supported or braced by the story, kips (N)

R_M = stiffness-reduction coefficient to account for member P-δ influence on structure P-Δ

α = ASD/LRFD force level adjustment factor, equal to 1.0 (LRFD) or 1.6 (ASD)

Δ_H = first-order interstory drift, in. (mm)

The first-order interstory drift, Δ_H, is equivalent to Δ_{1st} in Tables 2 and 3. The stiffness-reduction coefficient R_M is defined by AISC *Specification* Equation A-8-8 in terms of P_{mf}/P_{story}, where P_{mf} is the total vertical load in moment frames columns.

Note that the ratio Δ_H/L is the so-called drift ratio for the lateral load H. The drift Δ_H should be determined from an analysis consistent with the stability design method used: reduced stiffness for the direct analysis method and nominal properties for the effective length method (and for verifying applicability of the first-order method). The value of B_2 so determined is appropriate for that stability-design method.

AISC *Specification* Section C2.1(b) states that P-δ influence on P-Δ amplification may be neglected for systems with second-order story-drift amplification less than 1.5 (1.7 for reduced stiffness) and in which no more than one-third of the gravity load is supported on moment frame columns. In such cases, taking R_M equal to 1.0 gives the same result as performing a P-Δ-only second-order analysis. Note that AISC *Specification* Equation A-8-8 for R_M gives a conservative, lower-bound value; see Sabelli and Griffis (2021) for a more precise formulation.

Determination of the $\mathbf{B_2}$ *Amplifier Using Drift Limit*

Sabelli et al. (2021) present a method for using the drift limit to bound the second-order effect, permitting determination of second-order amplification prior to design and analysis. This method can be used to obtain values of the second-order amplifier, B_2, based on the second-order drift ratio Δ_2/L adapting Equation 3 in Sabelli and Griffis (2021):

$$B_2 = 1 + \frac{\alpha P_{story}\Delta_2}{HL} \tag{2}$$

The second-order drift, Δ_2, must not exceed the drift limit, Δ_{all}, and thus may conservatively be taken as equal to it. For seismic design, the drift is amplified by the deflection-amplification factor, C_d. (This factor may be taken as 1.0 for wind design.) Thus:

$$C_d\Delta_2 = \Delta_{all} \tag{3}$$

and

$$B_2 = 1 + \left(\frac{\alpha P_{story}}{C_d H}\right)\left(\frac{\Delta_{all}}{L}\right) \tag{4}$$

Values so determined are the upper bound of second-order amplification for structures meeting the drift limit. These values are generally reasonable for drift-governed systems but may be excessively conservative for systems with drift significantly below the limit.

The vertical force, αP_{story}, used in Equation 4 should be consistent with analysis used for determining drift-limit compliance. For seismic design, the strength evaluation and drift evaluation typically utilize the same vertical load. For wind design, the serviceability drift evaluation typically utilizes a lower vertical load than the strength evaluation, and thus the amplifiers for the two evaluations may be significantly different. (Note that serviceability loads are not identical to Allowable Strength Design load combinations, and the factor α does not apply. For guidance on serviceability loads and drift limits, see Griffis, 1993.)

Inherent in this method is the assumption that second-order analysis is used to determine drift. Use of unamplified first-order analysis to determine drift is unconservative generally (LeMessurier, 1977) and incompatible with this method. That is, Equation 2 utilizes the second-order drift, and thus, values of the amplifier B_2 obtained using Equation 4 (which is derived from Equation 2) correspond to systems stiff enough such that the second-order drift meets the drift limit. A system in which the first-order drift is at the drift limit is more flexible than assumed in Equation 4 and thus the amplifier values will not be correct. To ensure the validity of this method (and of the design), the first-order drifts must be amplified to capture second-order effects when determining conformance to the drift limits. Amplification by the B_2 factor is typically sufficient to capture these effects.

Tables for Determination of the $\mathbf{B}_2$ *Amplifier for Approximate Second-Order Analysis*

Tables 4 and 5 provide values for the B_2 amplifier based on first-order drift (Table 4) and the drift limit (Table 5). Table 5 may be used as an upper bound; once a drift value is determined by analysis, Table 4 may provide a lower value for systems stiffer than required to meet the drift limit.

The values in Table 4 are calculated for pairs of load ratio modified by the P-δ stiffness-reduction coefficient ($\alpha P_{story}/R_M H$) versus drift index (Δ_H/L), based on Equation 1. The values in Table 5 are calculated for pairs of load ratio modified by the deflection-amplification factor ($\alpha P_{story}/C_d H$) versus drift-limit ratio (Δ_{all}/L), based on Equation 4. The drift values and limits provided in Tables 4 and 5 include those for seismic design per ASCE/SEI 7 (2022), Table 12.12-1, as well as drift limits commonly used for wind serviceability design. The vertical loads, αP_{story}, used in the modified load ratios are effectively at LRFD level. Both tables require that the lateral load H be the load used for determination of drift or drift-limit compliance. The resulting value of B_2 is based on the system stiffness (Table 4) or the minimum required effective (second-order) system stiffness (Table 5) and is, therefore, applicable to the strength design for any level of lateral load (ASD or LRFD). In Table 4, the load ratio is modified by the P-δ stiffness-reduction R_M. In Table 5, it is modified by the seismic deflection-amplification factor C_d.

In Tables 4 and 5, values of B_2 that are less than or equal to 1.1 are indicated in the white region of the table; in this region, an effective length factor of 1.0 may be used, regardless of the method of stability design. The light gray portions of the table represent the regions where B_2 is greater than 1.1 and no greater than 1.5; in this region, the effective length method may require an effective length factor that is greater than 1.0. The dark gray represents the regions where B_2 is greater than 1.5 and no greater than 2.5; in this region, the direct analysis method is permitted but the first-order and effective-length methods are not. The black-shaded region is where B_2 is greater than 2.5; it is recommended that the structure be stiffened when B_2 is greater than this limit.

The reduced-stiffness model used in the direct analysis method is not intended to amplify the calculated drift; the engineer may account for this by increasing the drift limit when using a reduced-stiffness model. However, the recommended limit of 2.5 for the direct analysis method applies to determination of B_2 using the reduced-stiffness model.

Interpolation may be used with both Tables 4 and 5. In Table 4, interpolation is conservative between values of $\alpha P_{story}/R_M H$ and between values of Δ_H/L (or between values of Δ_H), resulting in a value of B_2 larger than would be determined by direct calculation. In Table 5, linear interpolation between, and extrapolation beyond, values of Δ_{all}/L and $\alpha P_{story}/C_d H$ are valid due to the simplicity of Equation 4.

Simplified Method for Determination of Required Strength

When a quick, conservative stability-design solution is desired, the following "simplified method" presented by Carter and Geschwindner (2008) can be used. This method is based on the effective length method for stability design, utilizing the approximate second-order analysis method in AISC *Specification* Appendix 8 and is, therefore, subject to the limitations on those two methods as presented in Tables 1 and 2.

Additionally, to permit the use of a single amplifier, the method is limited to systems in which the value of the amplifier B_1 does not exceed that of B_2. This is typically true for members that are not subject to significant transverse loading between their ends (a condition that makes it unlikely that B_1 is greater than 1.0); this is generally the case for columns. Additionally, even though the beams in a frame may be subject to transverse loads, they tend to have low values of B_1 due to the low ratio of αP_r to P_{e1} (used in AISC *Specification* Equation A-8-3). While these two general conditions apply to many (or even most) buildings, the engineer is nevertheless responsible for ensuring that their design is within the limitations for this method.

If B_1 does not exceed B_2, it is conservative to amplify the total moment from a first-order analysis ($M_{nt} + M_{lt}$) by B_2 to determine the required strength, M_r, effectively setting B_1 equal to B_2. Thus, AISC *Specification* Equation A-8-1 becomes:

$$M_r = B_1 M_{nt} + B_2 M_{lt} \le B_2 (M_{nt} + M_{lt}) \tag{5}$$

where

B_1 = multiplier to account for P-δ effects

M_{lt} = first-order moment due to lateral translation of the structure only, kip-in. (N-mm)

M_{nt} = first-order moment with the structure restrained against lateral translation, kip-in. (N-mm)

Similarly, for convenience, the other total forces from a first-order analysis, such as total axial force ($P_{nt} + P_{lt}$), can be amplified conservatively by B_2 to determine the required strength, P_r, and AISC *Specification* Equation A-8-2 becomes:

$$P_r = P_{nt} + B_2 P_{lt} \le B_2 (P_{nt} + P_{lt}) \tag{6}$$

where

P_{lt} = first-order axial force due to lateral translation of the structure only, kips (N)

P_{nt} = first-order axial force with the structure restrained against lateral translation, kips (N)

Table 4. B_2 Amplifier for Approximate Second-Order Analysis for P-Δ Effects Using First-Order Drift

		$\alpha P_{story}/R_M H$							
Δ_H/L	Δ_H	10	20	40	60	80	100	160	200
0.0005	L/2000	1.01	1.01	1.02	1.03	1.04	1.05	1.09	1.11
0.0010	L/1000	1.01	1.02	1.04	1.06	1.09	1.11	1.19	1.25
0.0020	L/500	1.02	1.04	1.09	1.14	1.19	1.25	1.47	1.67
0.0025	L/400	1.03	1.05	1.11	1.18	1.25	1.33	1.67	2.00
0.0040	L/250	1.04	1.09	1.19	1.32	1.47	1.67		
0.0050	L/200	1.05	1.11	1.25	1.43	1.67	2.00		
0.0067	L/150	1.07	1.15	1.36	1.67	2.14			
0.0100	L/100	1.11	1.25	1.67	2.50				
0.0150	L/67	1.18	1.43	2.50					
0.0200	L/50	1.25	1.67						
0.0250	L/40	1.33	2.00						

$B_2 > 2.50$; stiffen structure

Notes:
1. White region: $1.0 < B_2 \le 1.1$
2. Light gray region: $1.1 < B_2 \le 1.5$
3. Dark gray region: $1.5 < B_2 \le 2.5$
4. Black region: $B_2 > 2.5$

Table 5. B_2 Amplifier for Approximate Second-Order Analysis for P-Δ Effects Using Drift Limit (Second-Order Drift)

		$\alpha P_{story}/C_d H$							
Δ_{all}/L	Δ_{all}	10	20	40	60	80	100	160	200
0.0005	L/2000	1.01	1.01	1.02	1.03	1.04	1.05	1.08	1.10
0.0010	L/1000	1.01	1.02	1.04	1.06	1.08	1.10	1.16	1.20
0.0020	L/500	1.02	1.04	1.08	1.12	1.16	1.20	1.32	1.40
0.0025	L/400	1.03	1.05	1.10	1.15	1.20	1.25	1.40	1.50
0.0040	L/250	1.04	1.08	1.16	1.24	1.32	1.40	1.64	1.80
0.0050	L/200	1.05	1.10	1.20	1.30	1.40	1.50	1.80	2.00
0.0067	L/150	1.07	1.13	1.27	1.40	1.53	1.67	2.07	2.33
0.0100	L/100	1.10	1.20	1.40	1.60	1.80	2.00		
0.0150	L/67	1.15	1.30	1.60	1.90	2.20	2.50		
0.0200	L/50	1.20	1.40	1.80	2.20				
0.0250	L/40	1.25	1.50	2.00	2.50				

$B_2 > 2.50$; stiffen structure

Notes:
1. White region: $1.0 < B_2 \le 1.1$
2. Light gray region: $1.1 < B_2 \le 1.5$
3. Dark gray region: $1.5 < B_2 \le 2.5$
4. Black region: $B_2 > 2.5$

By applying the factor B_2 to all forces, the simplified method amplifies both lateral-load and gravity-sway effects, obviating the need for separate translation and no-translation analyses otherwise required for systems with significant gravity sway using the amplified first-order analysis method. To permit such an approach, the gravity load causing lateral sway must be amplified by the factor B_2 in determining the lateral drift Δ_H such that the gravity-load effect on the lateral load-resisting system is captured in the B_2 amplifier selected. Application of the factor B_2 is not required for axial forces on members that do not have forces resulting from or inducing lateral translation, such as vertical leaning columns designed as pin ended. As discussed in the Methods of Second-Order Analysis section, the B_2 amplification applies to all lateral-load effects, including member shear and connection forces. B_2 amplification factors may be obtained from Table 4 or Table 5, as discussed in the following.

The simplified method consists of six steps:

Step 1: Establish story drift limit and the corresponding lateral load. Together these represent the minimum required lateral stiffness of the structure.

Step 2: Perform a first-order elastic analysis. Gravity load cases must include a minimum lateral load at each story equal to 0.002 times the story gravity load, where the story gravity load is the load introduced at that story, independent of any loads from above.

Step 3: Determine the ratio of the total story gravity load to the lateral load determined in Step 2. For an ASD design, this ratio must be multiplied by 1.6. If Table 4 is used, this ratio is divided by the coefficient R_M for moment-frame structures. If Table 5 is used, this ratio is divided by the factor C_d for seismic design.

Step 4: Multiply all of the forces and moments from the first-order analysis by the value of B_2 obtained from Table 4 or Table 5. (Axial forces in leaning columns need not be amplified.) Use the resulting forces and moments as the required strengths for the designs of all members and connections. Note that B_2 must be computed for each story and in each principal direction.

Step 5: For all cases where the B_2 amplifier is 1.1 or less, the effective length may be taken as the unbraced length (i.e., $K = 1.0$). For cases where the B_2 amplifier is greater than 1.1 but does not exceed 1.5, determine the effective length factor as described in the Design for Stability section for the effective-length method. For cases where the value exceeds 1.5, the structure is too flexible to permit use of this method; either the direct analysis method should be used, or the structure must be stiffened.

Step 6: Compute the approximate second-order drifts by amplifying first-order drifts from Step 2 using the amplifier B_2 (and the factor C_d for seismic design). Compare to the drift limit set in Step 1. Revise the design as needed.

Note that using the drift limit (rather than the calculated first-order drift) in Table 4 is a conservative simplification. Using Table 5 removes this simplification but conservatively assumes the (second-order) drift is equal to the drift limit. Regardless of which table is used in the first iteration prior to analysis, iteration using the calculated first-order drift (with Table 4) can reduce the B_2 amplifier (Sabelli et al., 2021). For more information on this simplified method, see Carter and Geschwindner (2008).

CONCLUSION

Proper analysis and design include consideration of stability and the conditions that affect stability. The AISC *Specification* provides several practical approaches, each one valid within the limitations specified. The individual stability effects can be handled either by determining a more accurate (usually greater) value of required strength (demand) through more detailed modeling and analysis, or by imposing reductions to the available strength (capacity). Practical simplifications can often acceptably be made without unduly affecting the economy of the design; some such methodologies and approaches are described in this paper.

APPENDIX A

Diagram of Three Methods of Second-Order Analysis

Second-order effects increase deflection, and P-Δ effects (including P-δ influence on P-Δ) make the structure more flexible. Each of the three methods of second-order analysis discussed in this paper can be considered to address structure-level second-order stiffness reduction in a different way.

Figure A-1 shows first-order and second-order forces and displacements for the three methods of second-order analysis discussed earlier. For all three methods, the vertical load, P_{story}, and the external lateral load, H, are the same, but the second-order displacements and internal forces vary between methods. [To highlight differences, high values of P_{mf}/P_{story} (1.0) and B_2 (1.8) are used.]

For general second-order analysis (point 1), the stiffness is reduced by both the P-Δ and the P-δ effects. The external force H causes a displacement, Δ_2, determined by second-order analysis. The internal forces correspond to this lateral deformation and the internal second-order stiffness, which includes P-δ softening. In the figure, the second-order effects are represented by the displacement amplification factor, D_{AF}, and the force amplification factor, F_{AF}, based on LeMessurier's work (1977) and discussed in Griffis and White (2013).

For P-Δ-only second-order analysis (point 2), the P-δ effects on P-Δ are not included, and thus both the second-order displacement and the second-order forces are underestimated. (The condition in Figure A.1 with P_{mf}/P_{story} = 1.0 is well outside the range permitted for P-Δ-only second-order analysis, and thus, the degree of underestimation exceeds that permitted by the AISC *Specification*.) The internal forces correspond to the second-order lateral deformation and the lateral stiffness without P-δ softening. Both displacements and forces are amplified by $1/(1-\theta)$, with θ determined using the appropriate vertical forces for strength design. (This is identical to B_2 computed with R_M = 1.0.)

For approximate second-order analysis, a first-order analysis is performed (point 3), and first-order forces are amplified by the factor B_2, which may also be used to approximate second-order displacements (point 4). Note that the force amplification is overestimated due to the simplified equation for R_M in AISC *Specification* Appendix 8. Displacement is slightly underestimated.

If there are no P-δ effects on P-Δ, the differences between the three methods disappear, and points 1 and 4 move to point 2. Similarly, the differences between methods are much less significant for cases with smaller second-order effects.

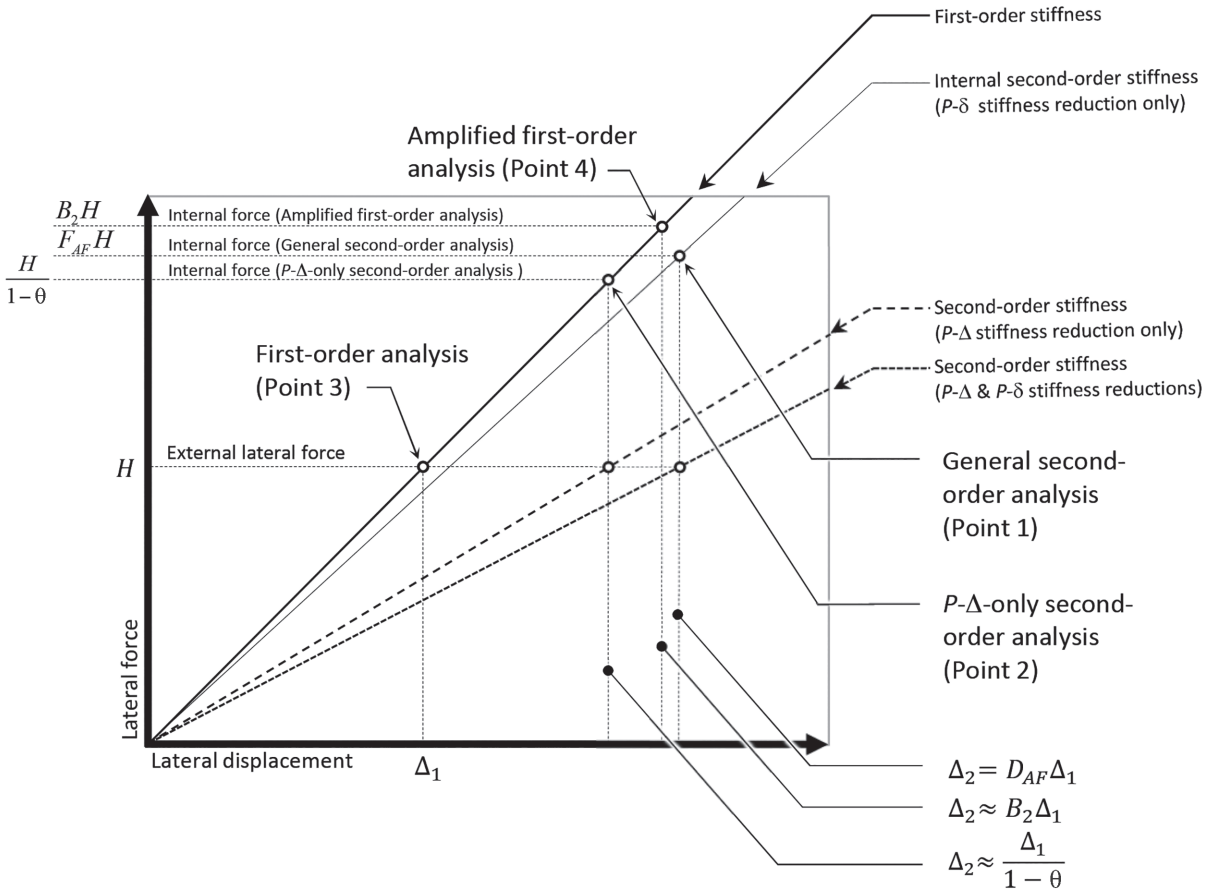

Fig. A-1. Diagram of methods of second-order analysis.

APPENDIX B

Design Example

Application of stability-design and second-order-analysis requirements are illustrated in the following example. The example utilizes amplified first-order analysis in combination with tables and equations in the paper to determine second-order forces and displacements (i.e., approximate second-order analysis) using the direct analysis method. For comparison purposes, results from a true second-order analysis are presented as well.

While it is not typical to perform direct analysis using tables and hand methods, this design example also demonstrates how these methods can give the engineer higher confidence in the results of a computer second-order analysis by confirmation with simpler methods. Results from computer analysis programs that have been validated using benchmark problems may nevertheless be incorrect due to missing gravity loads or other implementation errors.

The example is adapted from AISC Design Guide 28, Example 3.2 (Griffis and White, 2013). For brevity, the reader is referred to the original example for certain portions of the design not relevant to the illustration of the methods presented in this paper. The example consists of the following steps:

1. Determination of loads (see Griffis and White, 2013).
2. Determination of second-order amplification for service-level loads.
3. Selection of members to meet serviceability drift limit.
4. Determination of second-order amplification for strength-level loads.
5. Determination of member design forces.
6. Member strength checks (see Griffis and White, 2013).

Figure B-1 shows the building plan.

For brevity, the design example presented here is only for the north-south moment frames and is limited to two load combinations: a serviceability load combination used for a drift check and a strength load combination used to determine a member force. Similarly, for simplicity only, uniform loading is considered; this obviates the need to amplify gravity-sway moments.

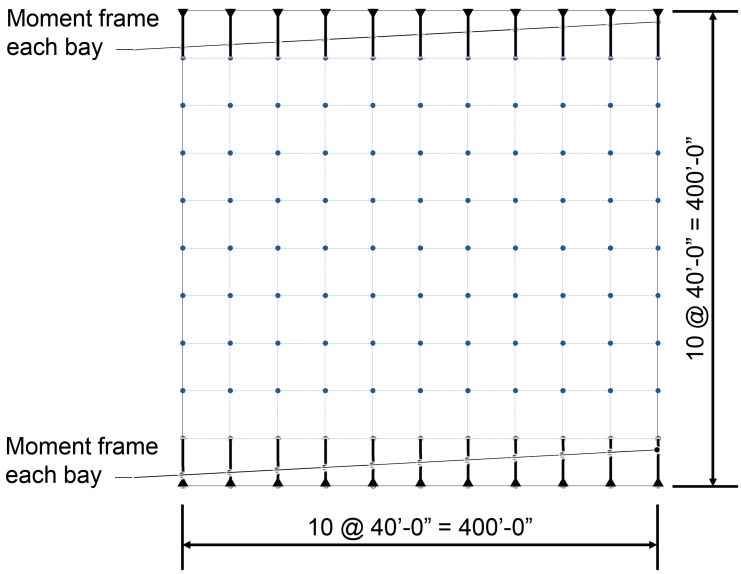

Fig. B-1. Plan of example building (from Griffis and White, 2013).

Table B.1. Load Combinations		
Designation	**Description**	**Combination**
Combination S	Service	$1.0D + 0.5S + 1.0W_y$
Combination 12	Strength	$1.2D + 0.5S - 1.6W_y - N_y$

Table B.2. Loads on Example Building			
Designation	**Symbol**	**Value (kips)**	**Comment**
Dead	D	5120	Uniformly distributed
Snow	S	4800	Nonuniform loading is not considered
Wind	W_y	120	50-year wind in building y-axis (north–south) direction
Notional	N_y	17.1	Notional load for Combination 12 in building y-axis direction $N_y = 0.002[1.2(5{,}120 \text{ kips}) + 0.5(4{,}800 \text{ kips})]$

Note that the original example utilizes ASCE/SEI 7-10 (ASCE, 2010) and thus the wind-load factors differ from those used in ASCE/SEI 7-22. Load combinations are presented in Table B.1 and loads in Table B.2.

Figure B-2 shows an elevation of the typical two-member frame.

Additionally, for purposes of illustration of drift-governed conditions, the example assumes a serviceability drift limit that differs from the original example:

$$\Delta_{service} \le \Delta_{all}$$
$$= 2.50 \text{ in.}$$
$$\frac{\Delta_{all}}{L} = \frac{2.50 \text{ in.}}{360 \text{ in.}}$$
$$= 0.00694$$

Determination of Second-Order Amplification for Service-Level Loads

To begin, Table 5 is used to determine the second-order amplification for the serviceability condition.

For wind serviceability, $C_d = 1.0$ and $\alpha = 1.0$.

$$\frac{\alpha P_{story}}{C_d H} = \frac{(1.0)(7{,}520 \text{ kips})}{(1.0)(120 \text{ kips})}$$
$$= 62.7$$

From Table 5 (or Equation 4), the estimated value of the amplifier is determined as B_2(service) = 1.43. Using this amplifier, members are selected such that the second-order drift meets the drift limit.

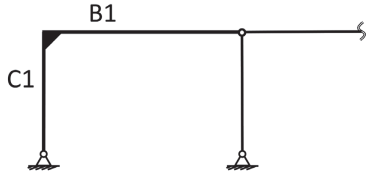

Fig. B-2. Elevation of typical frame (from Griffis and White, 2013).

Table B.3. Beam and Column Sizes		
Member	**Edge Frames**	**Interior Frames**
C1	W24×117	W24×117
B1	W24×131	W24×146

For service-level loading the maximum first-order drift can be estimated by:

$$\Delta_1 \le \frac{\Delta_{all}}{B_{2(service)}}$$
$$= \frac{2.50 \text{ in.}}{1.43}$$
$$= 1.75$$

Use of B_2 as a displacement amplifier is reasonable for low values of P_{mf}/P_{story}. For larger values of P_{mf}/P_{story} a second-order analysis may be more appropriate, especially for larger values of B_2. See Sabelli and Griffis (2021) for numerical comparisons.

Selection of Members to Meet Serviceability Drift Limit

Column and beam sizes are selected such that the first-order drift does not exceed this value. Sizes are given in Table B.3. (These sizes differ from the service evaluation in the Design Guide but are used in the subsequent strength evaluation.)

With the moment frame column and girder sizes listed in Table B-3, the first-order story drift from the first-order analysis is:

$$\Delta_1 = 1.72 \text{ in.}$$

For comparison and validation purposes, this first-order drift from analysis can be used to calculate B_2 more accurately:

$$R_M = 1 - 0.15(P_{mf}/P_{story}) \quad \text{(}Spec\text{. Eq. A-8-8)}$$
$$= 1 - 0.15(848 \text{ kips}/7{,}520 \text{ kips})$$
$$= 0.983$$

Using Table 4:

$$\frac{\alpha P_{story}}{R_M H} = \frac{1.0(7{,}520 \text{ kips})}{0.983(120 \text{ kips})}$$
$$= 63.8$$
$$\frac{\Delta_H}{L} = \frac{1.72 \text{ in.}}{360 \text{ in.}}$$
$$= 0.00477$$
$$B_2 = 1.46$$

This value is determined conservatively using $\Delta/L = 0.005$ and between $\alpha P_{story}/R_M H = 60$ and 80.

Alternatively, using Equation B-1:

$$B_2 = \frac{1}{1 - \left(\frac{\alpha P_{story}}{R_M H}\right)\left(\frac{\Delta_H}{L}\right)} \quad \text{(B-1)}$$
$$= \frac{1}{1 - \left[\frac{1.0(7{,}520 \text{ kips})}{0.983(120 \text{ kips})}\right]\left(\frac{1.72 \text{ in.}}{360 \text{ in.}}\right)}$$
$$= 1.44$$

Table B.4. Column and Beam End Moments from First-Order Analysis		
		Column C1 and Beam B1 End Moments (kip-ft)
Dead	M_D	130
Snow	M_S	122
Wind	M_W	166
Notional	M_N	23.6

Both the estimated first-order drift and the estimated second-order amplification for service-level loading are close to the values based on analysis. Because AISC *Specification* Equation A-8-8 for determining R_M is somewhat conservative, Equation 4, which conservatively uses the drift limit but does not use R_M, gives a slightly lower result than Equation B-1, which uses the actual first-order drift but requires R_M, for this drift-controlled example.

Determination of Second-Order Amplification for Strength-Level Loads

Next, the B_2 amplifier is calculated for member strength design for Combination 12. (Note that Combination 12 does not have the maximum vertical load. The B_2 amplifier for this combination is not appropriate for strength design using load combinations with higher vertical load.) For strength-level loading using the direct analysis method, there are two differences that affect the B_2 amplifier. First, the vertical load corresponds to the strength-level load combinations. Second, the lateral stiffness of the frame is reduced by a factor 0.8, and thus for the lateral load H, Δ_H = 1.72 in./0.8. For conditions in which the additional flexural stiffness reduction factor τ_b applies, use of Equation B-1 to capture the total direct-analysis stiffness reduction is not appropriate. The value of τ_b = 1.0 is typically confirmed after analysis, but in this case, it is obvious by inspection.

$$B_2 = \frac{1}{1-\left(\frac{\alpha P_{story}}{R_M H}\right)\left(\frac{\Delta_H}{L}\right)} \tag{B-2}$$

$$= \frac{1}{1-\left[\frac{1.0(8{,}544 \text{ kips})}{0.983(120 \text{ kips})}\right]\left(\frac{1.72 \text{ in.}/0.8}{360 \text{ in.}}\right)}$$

$$= 1.76$$

Determination of Member Design Forces

A first-order analysis is performed. The frame is modelled with reduced stiffness for the direct analysis method, with τ_b = 1.0. End moments for column C1 and beam B1 for an interior frame are presented in Table B.4.

The amplified first-order analysis results for Combination 12 are:

$$M_u = 1.2M_D + 0.5M_S + B_2(1.6M_W + M_N)$$

$$= 1.2(130 \text{ kip-ft}) + 0.5(122 \text{ kip-ft}) + (1.76)\left[1.6(166 \text{ kip-ft}) + (23.6 \text{ kip-ft})\right]$$

$$= 726 \text{ kip-ft}$$

For comparison, an iterative, incremental second-order analysis using Combination 12 is also performed, with appropriate column meshing to capture P-δ influence on structure P-Δ. The second-order analysis for Combination 12 gives:

$$M_u = 719 \text{ kip-ft}$$

From this second-order analysis, the second-order amplification using the direct analysis reduced-stiffness strength model for Combination 12 is:

$$\frac{\Delta_2}{\Delta_1} = \frac{6.53 \text{ in.}}{3.74 \text{ in.}} = 1.75$$

This value compares well with the value of 1.76 determined for B_2. The slight overestimation of forces using the B_2 amplifier (approximately 1%) can be attributed to the conservatism of AISC *Specification* Equation A-8-8 for determining R_M.

GLOSSARY

Amplifier. Factor applied to load effect from first-order analysis to approximate load effect from second-order analysis.

Approximate second-order analysis. Amplified first-order analysis approximating second-order effects by amplifiers B_1 (for member P-δ effects) and B_2 (for P-Δ effects).

Braced frame. Essentially, a vertical truss system that provides resistance to lateral forces and provides stability for the structural system.

Buckling. Limit state of sudden change in the geometry of a structure or any of its elements under a critical loading condition.

Buckling strength. Strength for instability limit states.

Drift. Lateral deflection of structure.

Drift ratio. Interstory drift divided by story height, taken at a representative location.

Effective length factor, K. Ratio between the effective length and the unbraced length of the member.

Effective length. Length of an otherwise identical compression member with the same strength when analyzed with simple end conditions.

Elastic analysis. Structural analysis based on the assumption that the structure returns to its original geometry on removal of the load.

First-order analysis. Structural analysis in which equilibrium conditions are formulated on the undeformed structure; second-order effects are neglected.

First-order stiffness. Lateral stiffness of the structure neglecting second-order effects.

Geometric imperfections:

Member imperfection. Initial displacement of points along the length of individual members (between points of intersection of members) from their nominal locations, such as the out-of-straightness of members due to manufacturing and fabrication.

System imperfection. Initial displacement of member intersections from their nominal locations, such as the out-of-plumbness of columns due to erection tolerances.

Gravity sway. Lateral drift caused by vertical gravity loads on the undeformed structure (i.e., considered without imperfections or notional loads).

Inelastic analysis. Structural analysis that takes into account inelastic material behavior, including plastic analysis.

Internal second-order stiffness. Lateral stiffness of the structure relating displacements to internal (member) forces, modified considering the reduced flexural stiffness of members with compressive axial force (P-δ stiffness-reduction).

Interstory drift. Drift at a given story relative to the drift at the story below taken at vertically aligned points.

Instability. Limit state reached in the loading of a structural component, frame or structure in which a slight disturbance in the loads or geometry produces large displacements.

Lateral force-resisting system. Structural system designed to resist lateral loads and provide stability for the structure as a whole.

Lateral load. Load acting in a lateral direction, such as wind or earthquake effects.

Leaning column. Column designed to carry gravity loads only, with connections that are not intended to provide resistance to lateral loads.

Moment frame. Framing system that provides resistance to lateral loads and provides stability to the structural system, primarily by shear and flexure of the framing members and their connections.

Notional load. Virtual load applied in a structural analysis to account for destabilizing effects that are not otherwise accounted for in the design provisions.

P-Δ effect. Effect of loads acting on the displaced location of joints or nodes in a structure. In tiered building structures, this is the effect of loads acting on the laterally displaced location of floors and roofs

P-δ effect. Effect of loads acting on the deflected shape of a member between joints or nodes.

P-δ stiffness-reduction. Reduction of flexural stiffness of members due to the presence of axial compression, affecting system lateral stiffness and increasing the *P-Δ* effect.

Second-order analysis. A structural analysis that solves for equilibrium between internal and external forces in the deformed state.

General second-order analysis. A second-order analysis in which *P-δ* effects *P-Δ* effects are directly analyzed.

P-Δ only second-order analysis. A second-order analysis in which *P-Δ* effects are directly analyzed and *P-δ* effects are addressed by means of application of B_1 amplifiers.

Rigorous second-order analysis. A general second-order analysis that includes consideration of additional second-order effects related to member twist. (See AISC *Specification* Appendix 1 Section 1.2a.)

Second-order effect. Effect of loads acting on the deformed configuration of a structure; includes *P-Δ* effect, *P-δ* effect, and *P-δ* stiffness reduction.

Second-order stiffness. Lateral stiffness of the structure relating displacements to external loads, modified considering the *P-Δ* effect.

Stability. Condition in the loading of a structural component, frame, or structure in which a slight disturbance in the loads or geometry does not produce large displacements.

Stability design. Structural design that addresses the five general considerations in AISC *Specification* Section C1.

Stiffness reductions. Modifications in axial and flexural stiffness in the direct analysis method to capture destabilizing effects of member imperfections and inelasticity as well as uncertainties in strength and stiffness.

Story stiffness. Story shear divided by interstory drift. Story stiffness is sensitive to the loading profile; use of the design load profile to determine story stiffness is recommended.

SYMBOLS

A	Cross-sectional area of member, in.^{2} (mm^2)
B_1	Multiplier to account for *P-δ* effects
B_2	Multiplier to account for *P-Δ* effects
C_d	Deflection amplification coefficient for seismic analysis
D_{AF}	Displacement amplification factor
E	Modulus of elasticity of steel, ksi (MPa)
F_{AF}	Force amplification factor, similar to B_2
H	Total story shear, in the direction of translation being considered, produced by the lateral forces used to compute Δ_H, kips (N)
I	Moment of inertia in the plane of bending, in.^{4} (mm^4)
K	Effective length factor
K_2	Effective length factor modified for effect of leaning columns
L	Height of story, in. (mm)
M_{lt}	First-order moment due to lateral translation of the structure only, kip-in. (N-mm)
M_{nt}	First-order moment with the structure restrained against lateral translation, kip-in. (N-mm)
P_e	Elastic critical buckling strength of member kips (N)
P_{ns}	Member compressive strength, kips (N)
P_r	Member required strength, kips (N)
P_{lt}	First-order axial force due to lateral translation of the structure only, kips (N)
P_{mf}	Total vertical load in columns in the story that are part of moment frames, if any, in the direction of translation being considered (= 0 for braced-frame systems), kips (N)
P_{nt}	First-order axial force with the structure restrained against lateral translation, kips (N)
P_{story}	Total vertical load supported by the story using LRFD or ASD load combinations, as applicable, including loads in columns that are not part of the lateral-force-resisting system, kips (N)
R_M	Stiffness-reduction coefficient to account for member *P-δ* influence on structure *P-Δ*
α	ASD/LRFD force level adjustment factor, equal to 1.0 (LRFD) or 1.6 (ASD)
Δ_{all}	Allowable interstory drift, in. (mm)
Δ_H	First-order interstory drift, in the direction of translation being considered, due to lateral forces, in. (mm)
Δ_{1st}, Δ_1	First-order interstory drift, equal to Δ_H, in. (mm)
Δ_{2nd}, Δ_2	Second-order interstory drift, in. (mm)
τ_b	Flexural stiffness reduction factor for direct analysis method
θ	Stability coefficient from ASCE 7, Section 12.8.7

REFERENCES

AISC (2023), *Steel Construction Manual*, 16th Ed., American Institute of Steel Construction, Chicago, Ill.

AISC (2022), *Specification for Structural Steel Buildings*, ANSI/AISC 360-22, American Institute of Steel Construction, Chicago, Ill.

ASCE (2010), *Minimum Design Loads for Buildings and Other Structures*, ASCE/SEI 7-10, American Society of Civil Engineers, Reston, Va.

ASCE (2022), *Minimum Design Loads and Associated Criteria for Buildings and Other Structures*, ASCE/SEI 7-22, American Society of Civil Engineers, Reston, Va.

Carter, C.J. and Geschwindner, L.F. (2008), "A Comparison of Frame Stability Analysis Methods in ANSI AISC 360-05," *Engineering Journal*, AISC, Vol. 45, No. 3, pp. 159–170.

Flores, F., Charney, F.A., and Lopez-Garcia, D. (2018), "The Influence of Accidental Torsion on the Inelastic Dynamic Response of Buildings During Earthquakes," *Earthquake Spectra*, Vol. 34, No. 1, pp. 21–53.

Geschwindner, L.F. (2002), "A Practical Approach to Frame Analysis, Stability and Leaning Columns," *Engineering Journal*, AISC, Vol. 39, No. 4, pp. 167–181.

Griffis, L.G. (1993), "Serviceability Limit States under Wind Loads," *Engineering Journal*, AISC, Vol. 30, No.1, pp 1–16.

Griffis, L.G. and White, D.W. (2013), *Stability Design of Steel Buildings,* Design Guide 28, AISC, Chicago, Ill.

LeMessurier, W.J. (1977), "A Practical Method of Second Order Analysis Part 2; Rigid Frames," *Engineering Journal*, AISC, Vol. 14, No. 2, pp. 49–67.

Sabelli, R. and Griffis, L.G. (2021), "Internal Second-Order Stiffness: A Refined Approach to the R_M Coefficient to Account for the Influence of P-δ on P-Δ," *Engineering Journal*, AISC. Vol. 58, No. 2, pp. 139–146.

Sabelli, R., Griffis, L.G., and Geschwindner, L.F. (2021), "Determination of Second-Order Effects and Stability Effects Using the Drift Limit," *Engineering Journal*, AISC. Vol. 58, No. 3, pp. 185–196.

White, D.W. and Hajjar, J.F. (1991), "Application of Second-Order Elastic Analysis in LRFD: Research to Practice," *Engineering Journal*, AISC. Vol. 28, No.4, pp. 133–148.

White, D.W., Jeong, W.Y., and Slein, R. (2021), *Frame Design Using Nonprismatic Members,* Design Guide 25, AISC, Chicago, Ill.

Ziemian, C.W. and Ziemian, R.D. (2021), "Steel Benchmark Frames for Structural Analysis and Validation Studies: Finite Element Models and Numerical Simulation Data," *Data Brief*, Vol. 39, 107564.

Ziemian, R.D. and McGuire, W. (1992), "A Method for Incorporating Live Load Reduction Provisions in Frame Analysis," *Engineering Journal*, AISC, Vol. 29, No. 1, pp. 1–3.

Construction Cost Premiums for Risk Category IV Special Moment Frame Buildings

Paul W. Richards and Amy J. McCall

ABSTRACT

The International Building Code uses risk categories to reduce the probability of damage and collapse for certain buildings. One proposal for improving post-earthquake functional recovery is to design more buildings as Risk Category IV. The purpose of this study was to investigate the construction cost premiums for Risk Category IV buildings with steel special moment frames (SMF). Mathematical derivations were used to bound the stiffness and strength amplifications required for Risk Category IV design, accounting for period effects (as buildings are strengthened/stiffened, design loads increase). To complement this mathematical approach, 12 case study SMF buildings were designed with heights ranging from 2 to 16 stories. The primary conclusion of the study is that construction cost premiums for drift-governed SMF buildings are an order-of-magnitude greater than for strength-governed buildings. For many strength-governed buildings, the cost premium for Risk Category IV design is around 1% of the total building cost. For drift-governed SMF buildings, the cost premiums for Risk Category IV design are 6 to 16% of the total building cost, with the greatest premiums for buildings around eight stories. These cost premiums should be considered when evaluating Risk Category IV design as a strategy for improving post-earthquake functional recovery.

Keywords: functional recovery, special moment frames, construction cost, risk category, drift limit.

INTRODUCTION

The International Building Code (IBC) (ICC, 2021) uses risk categories to reduce the probability of damage and collapse of certain buildings under earthquake loading. Buildings with Risk Category IV are designed with a 1.5 multiplier in the base shear equation and about half the allowable drift as compared to Risk Category II (ASCE, 2016). The actual increases in strength and stiffness for structures designed as Risk Category IV may be greater than 1.5 and 2.0, respectively, because as a building is strengthened/stiffened its natural period decreases and the design loads may increase.

Broader use of Risk Category IV design is being discussed as an interim measure to improve the post-earthquake functional recovery of buildings. This discussion is important for steel special moment frames (SMF) because functional recovery is expected to be poor for code-minimum SMF that form plastic hinges in the beams (Erochko et al., 2011; Harris and Speicher, 2018; Richards et al., 2023). Methods for improving functional recovery for SMF include designing to a lower drift limit, providing better post-yield stiffness, and/or using replaceable fuses. Recommendations from NIST for improving post-earthquake functional recovery (NIST, 2021) suggest that, as an interim measure, requiring Risk Category IV for a broader class of buildings could substantially increase the number of buildings that are able to recover quickly.

To evaluate this approach to functional recovery (more Risk Category IV design) against other options, it is important to know the construction cost premium for Risk Category IV buildings, relative to Risk Category II buildings. NIST (2021) notes that in the code development process, certain industry groups oppose proposals that include even modest increases in initial construction costs.

Some studies have explored the cost of improved seismic design, but most results have limited application to SMF buildings. NIST (2013) investigated the cost of six buildings designed for the Memphis metropolitan area. The buildings were a three-story apartment (wood frame), a four-story office (steel braced frame), a one-story retail (tilt-up), a one-story warehouse (tilt-up), a six-story hospital (steel braced frame), and a two-story elementary school (masonry walls). The comparisons were between no seismic design, seismic design per local code [2003 IBC (ICC, 2003)], and seismic design per national seismic code [2012 IBC (ICC 2012), ASCE/SEI 7-10 (ASCE, 2010)]. The conclusion was that the cost premium for designing per 2012 IBC, as compared to 2003 IBC, was 1% or less. None of the buildings considered in the study were drift-governed. For the braced-frame hospital, the importance factor was 1.5 for both the 2003 IBC and 2012 IBC designs, so the impact of importance factor on design was not investigated. The 2012

Paul W. Richards, Vice President of Research and Development, DuraFuse Frames, West Jordan, Utah. Email: paul.richards@durafuseframes.com (corresponding)

Amy J. McCall, Development Engineer, DuraFuse Frames, West Jordan, Utah. Email:amy.mccall@durafuseframes.com

Paper No. 2022-09

IBC braced-frame hospital design had a 2.5% cost premium over a wind-only design.

Yu et al. (2015) investigated the cost of designing two school buildings in Oregon as Risk Category IV rather than Risk Category III so the buildings could serve as emergency shelters. Yu et al. estimated that the increase in structural construction costs would be less than 1%. The lateral force resisting system in both buildings was presumably strength-governed masonry walls.

Richards et al. (2022) mentioned the construction cost of three steel SMF buildings (4-, 6-, and 8-story) designed as both Risk Category II and Risk Category IV. The Risk Category IV buildings were designed with deeper columns and lower clear-heights between stories to help mitigate the cost impacts. Still, the cost premiums for the Risk Category IV designs were estimated as 4 to 14% of the total building costs, much higher than the premiums reported in the other studies.

The limited studies that have been cited suggest that drift-governed SMF buildings may have a substantially higher cost premium for Risk Category IV design than strength-governed buildings. As broader use of Risk Category IV design is being discussed, it would be helpful to have a more accurate sense of what the construction cost premiums are for Risk Category IV SMF buildings and a better theoretical basis for understanding the cost premiums.

The purpose of the present study was to quantify the impact of Risk Category IV design on the stiffness, strength, and weight of SMF buildings and determine the construction cost premiums for Risk Category IV SMF buildings.

METHODS

Two complementary methods were used for the study. The first method was to mathematically derive the difference in strength and stiffness for Risk Category II and Risk Category IV designs, accounting for period effects. Closed-form solutions were possible for single-degree-of-freedom (SDOF) systems. The derived stiffness and strength ratios (IV/II) were used with a cost index to bound the range of expected cost premiums.

The second method was to use case study buildings to compute cost premiums. Twelve SMF buildings with varying height (2-, 4-, 6-, 8-, 12-, and 16-story) and varying Risk Category (II and IV) were designed. The steel weights from the case study buildings were used with a cost index to estimate the Risk Category IV construction cost premium in terms of the total building cost.

Cost Index

A total building cost index was used in both approaches to estimate the cost premium for Risk Category IV designs. The cost of structural steel frames is influenced by labor more than material, but for estimating purposes, both labor and material costs were assumed to scale in proportion to the total steel weight. This approach indirectly accounts for added labor costs to make the heavier connections in the Risk Category IV designs. The index was based on the following assumptions:

- The total steel cost (gravity + lateral) was 10% of the total building cost for Risk Category II buildings.
- The total foundation cost (gravity + lateral) was another 10% of the total building cost for Risk Category II buildings.
- The total steel cost was proportional to the total steel weight.
- The foundation costs would rise in proportion to the increased steel weight for Risk Category IV buildings (only the foundation costs associated with the increased lateral frames would increase).

Restated, the cost index assumed that 80% of the total building cost was unrelated to the structure, and scaled the other 20%, associated with the steel and foundations, based on the ratio of the steel weights.

$$\text{Cost Index} = 0.8 + 0.2\left(\frac{W_{t,IV}}{W_{t,II}}\right) \tag{1}$$

where $W_{t,IV}$ is the total steel weight of a particular Risk Category IV building, and $W_{t,II}$ is the total steel weight of a comparison Risk Category II building.

Case Study Building Geometry, Loads, and Site Parameters

Various building plans and SMF layouts were used for the 12 case study buildings. The 2-, 4-, 6-, and 8-story buildings were 180 ft × 120 ft in plan and had SMF as indicated in Figure 1(a, b). The 12- and 16-story buildings were 100 ft × 100 ft in plan and had SMF as indicated in Figure 1(c). The floors extended 12 in. past the frame lines. The required clear height for the stories was 12 ft. Because most of the buildings had 3-ft-deep SMF beams, most of the story heights were 15 ft to achieve the clear height in the lower levels. However, for some of the buildings, shallower beams could be used, and the required story height to achieve the clear height was reduced (Table 1).

The loading used for design was:

- Floors: 45 psf (6.25 in. lightweight concrete on 3 in. metal deck)
- Steel framing: as designed (this turned out to be 5–15 psf, see Table 6)
- MEP: 7 psf

- Ceiling/lights/flooring: 3 psf
- Partitions: 20 psf (10 psf included for seismic weight)
- Floor live load: 50 psf (reducible)
- Roof live load: 20 psf (reducible)
- Exterior walls: 25 psf

The roof dead loads were assumed to be the same as the floors, roughly accounting for permanent equipment.

A Los Angeles site with $S_{DS} = 1.4$ and $S_{D1} = 0.75$ was used for the study.

Case Study Building Designs

The 12 case study buildings were designed using ASCE/SEI 7-16, *Minimum Design Loads and Associated Criteria for Buildings and Other Structures* (ASCE, 2016), hereafter referred to as ASCE/SEI 7; the AISC *Seismic Provisions for Structural Steel Buildings* (AISC, 2016b), hereafter referred to as the AISC *Seismic Provisions*; and the AISC *Prequalified Connections for Special and Intermediate Steel Moment Frames for Seismic Applications* (AISC, 2016a). The drift limit was 2.5% or 2.0% for the Risk Category II buildings, with the higher limit for the two- and four-story designs. For the Risk Category IV buildings, the drift limit was 1.5% or 1.0%. Linear modal response spectrum analysis was used for the designs, typical of U.S. practice in high seismic areas.

A welded beam-to-column connection with no reduced or reinforced beam sections was used for the SMF buildings so that no modifications to the element properties were necessary to represent the elastic stiffness of the beams or connections in the analysis model. The maximum beam depth permitted in the designs was W36, but shallower beams were used when they were the lightest options. All the designs used W27 columns for consistency.

RAM Structural System (Bentley, 2021) was used to perform all design checks, although other tools were used for initial member sizing. The SMF beam and column sizes were optimized for drift outside of RAM using a genetic algorithm (McCall and Richards, 2022). Within RAM, all final drift and strength checks were performed using linear modal response spectrum analysis. For strength checks, the period was limited to $C_u T_a$, but for drift checks, the actual building period from the model was used, per ASCE/SEI 7. The AISC *Seismic Provisions* seismic checks (e.g., strong-column weak-beam, doubler plates) were performed within RAM. The flexibility of the panel zones was represented in the RAM models by limiting the rigid end offsets to 25% of the theoretical length. Preliminary work had found that centerline modeling was too flexible when W27 columns were used, but rigid offsets over the entire theoretical length were too stiff.

Table 1 summarizes the seismic response coefficients, C_s, used for the strength and drift checks for each building. C_s was the value used for strength checks, which,

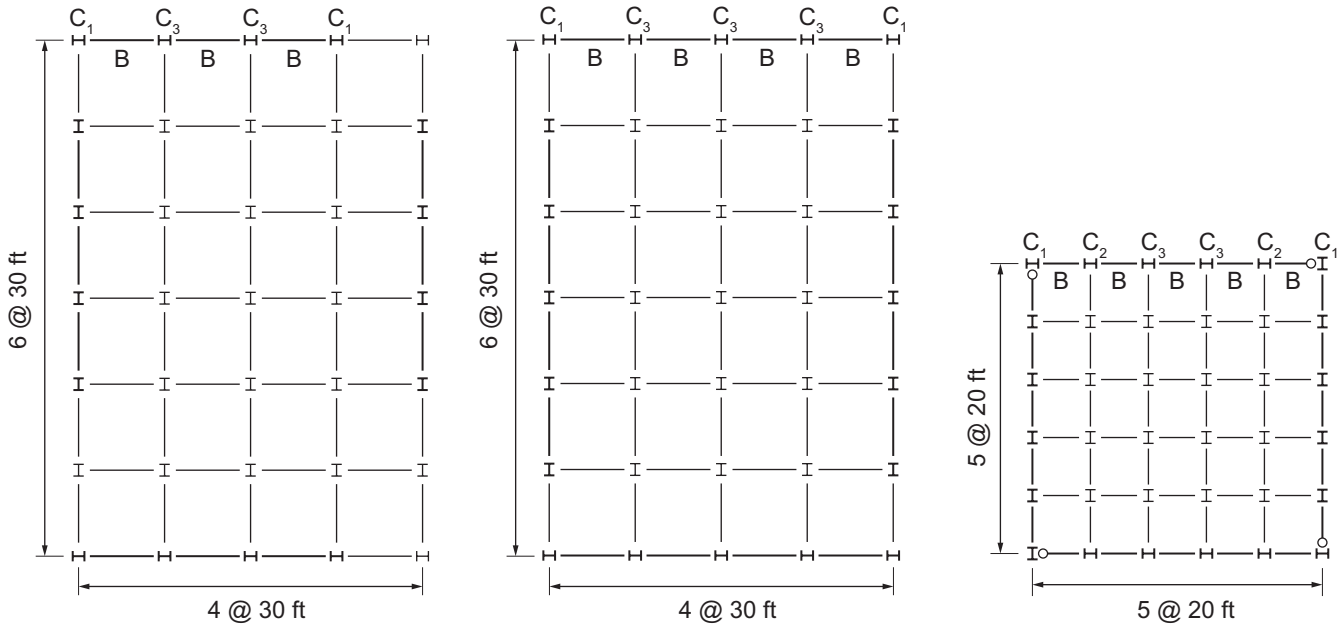

(a) 2- and 4-story buildings *(b) 6- and 8-story buildings* *(c) 12- and 16-story buildings*

Fig. 1. Plan views of the case study buildings.

Table 1. Seismic Response Coefficients Used for Case Study Buildings								
Stories	Risk	Story Height (ft)	C_uT_a (sec)	T_{RAM} (sec)	C_s	Governing ASCE/SEI 7 Equation for C_s	$C_{s,drift}$	$C_s/C_{s,drift}$
2	II	14.0	0.56	1.02	0.166	12.8-3	0.092	1.81
	IV	14.5	0.58	0.66	0.243	12.8-3	0.213	1.14
4	II	14.0	0.98	1.83	0.096	12.8-3	0.051	1.86
	IV	15.0	1.04	1.26	0.136	12.8-3	0.112	1.21
6	II	14.5	1.40	2.20	0.067	12.8-3	0.043	1.58
	IV	15.0	1.43	1.22	0.115	12.8-3	0.115	1.00
8	II	14.5	1.76	2.93	0.062	12.8-5	0.032	1.93
	IV	15.0	1.81	1.57	0.092	12.8-5	0.090	1.03
12	II	14.0	2.36	3.75	0.062	12.8-5	0.025	2.46
	IV	14.5	2.43	2.25	0.092	12.8-5	0.063	1.48
16	II	14.0	2.97	3.92	0.062	12.8-5	0.024	2.58
	IV	15.0	3.14	2.90	0.092	12.8-5	0.048	1.91

for the shorter buildings, was governed by ASCE/SEI 7, Equation 12.8-3, with the upper-limit period C_uT_a (Equation 12.8.2) used for the design period, T. For eight-story and taller buildings, C_s was governed by the minimum given by ASCE/SEI 7, Equation 12.8-5, which was period independent. $C_{s,drift}$ was the effective value used for drift checks, for which the upper limit on period did not apply (ASCE/SEI 7, Section 12.8.6.2). For drift checks, Equation 12.8-5 did not apply (ASCE/SEI 7, Section 12.8.6.1).

The frame designs are summarized in the Appendix.

Case Study Building Outputs

The primary outputs from each case study building were the steel weight (gravity and lateral), lateral stiffness, and lateral strength. The steel weights were obtained from the RAM weight take-offs. Beam and column weights were determined based on the assigned beam and column sizes and the centerline dimensions in the model. The steel weights obtained from RAM were used with the cost index (Equation 1) to determine cost premiums for Risk Category IV buildings. Steel weights did not include continuity plates, doubler plates, or column base plates.

The elastic lateral stiffness of each building was computed using an equivalent lateral force (ELF) load combination. The ELF base shear was divided by the center-of-mass drift at the roof (in rad) under ELF loading to obtain an effective building stiffness.

The first-yield strength of each case study building, V_y, was computed based on the demand/capacity (D/C) ratios under the ELF load combinations. The ELF base shear was divided by the highest beam D/C to estimate the base shear associated with first yielding (a phi factor of 1.0 was used for the beam capacity for this calculation).

RESULTS FROM MATHEMATICAL DERIVATIONS

The results from the study are presented in two parts. This first part presents the results from the mathematical derivations and has four subsections. The first subsection presents the mathematical derivation of the IV/II stiffness ratio for drift-governed designs. The second subsection presents the derivation of the IV/II strength ratio for strength-governed designs. The third subsection presents upper and lower bounds for the cost premium for strength-governed Risk Category IV design, based on the mathematical derivations, additional assumptions, and the total building cost index (Equation 1). The final subsection presents upper and lower bounds of the cost premium for drift-governed Risk Category IV design, which is pertinent for most steel SMF.

Derivation of Stiffness Ratio

The following derivation is for a single-degree-of-freedom system on the descending branch of the design spectra. A later section will discuss the results in the context of multi-degree-of-freedom systems. The derivation establishes the relationship between the required stiffness for Risk Category II and Risk Category IV designs when the designs are drift-governed.

Figure 2 defines the terms used in the derivation. The points on the spectra represent two designs. The Risk Category II design has a design base shear, V_2, and a period,

T_2. The Risk Category IV design has a design base shear, V_4, and a period, T_4. Both designs are assumed to be on the descending branch of the spectra, where S_{D1} is the design spectral response acceleration parameter at a period of 1.0 second, W is the seismic weight of the system, and I_e is the importance factor (ASCE, 2016).

Equations 2 and 3 relate the base shears and periods, according to the design spectra (Figure 2).

$$V_2 = \frac{S_{D1}}{T_2\left(\frac{R}{1.0}\right)}W \tag{2}$$

$$V_4 = \frac{S_{D1}}{T_4\left(\frac{R}{1.0}\right)}W \tag{3}$$

Note that the importance factor is taken as 1.0 for convenience in both drift-governed cases because the importance factor gets canceled out later in the drift calculation [I_e is in the denominator of ASCE/SEI 7, Equation 12.8-15, when computing the drift (ASCE, 2016)].

Combining Equations 2 and 3 and rearranging relates the periods and base shears of the Risk Category II and IV designs to each other, as shown in Equation 4.

$$\frac{T_4}{T_2} = \frac{V_2}{V_4} \tag{4}$$

Assuming the designs are drift-governed, the elastic displacement of each system under the design base shear (design base shear divided by the stiffness, k) will be equal to the elastic drift limit (δ_2 for the Risk Category II design and δ_4 for the Risk Category IV design).

$$\frac{V_2}{k_2} = \delta_2 \tag{5}$$

$$\frac{V_4}{k_4} = \delta_4 \tag{6}$$

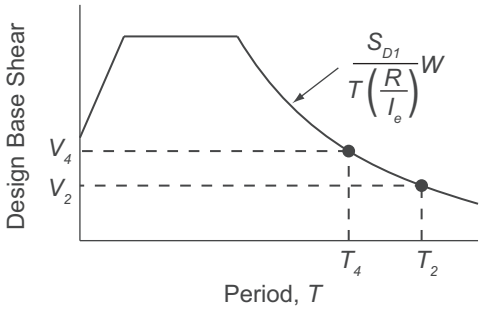

Fig. 2. Terms used for stiffness ratio derivation for drift-governed systems.

Combining Equations 5 and 6 and rearranging relates the drift ratio of the Risk Category II and IV designs to the design base shears and system stiffnesses.

$$\frac{\delta_2}{\delta_4} = \left(\frac{V_2}{V_4}\right)\left(\frac{k_4}{k_2}\right) \tag{7}$$

To combine Equations 4 and 7, the relationship between the system periods, T, and stiffnesses, k, is needed. The natural periods for the SDOF systems are:

$$T_2 = 2\pi\sqrt{\frac{m}{k_2}} \tag{8}$$

$$T_4 = 2\pi\sqrt{\frac{m}{k_4}} \tag{9}$$

where m is the mass (the same for both systems).

Combining Equations 8 and 9 and rearranging terms gives Equation 10.

$$\left(\frac{T_4}{T_2}\right)^2 = \frac{k_2}{k_4} \tag{10}$$

Combining Equations 10 and 4 and rearranging terms gives the relationship between the system stiffnesses and the design base shears, shown in Equation 11.

$$\frac{k_2}{k_4} = \left(\frac{V_2}{V_4}\right)^2 \tag{11}$$

And finally, combining Equations 11 and 7 and rearranging terms gives the relationship for the stiffness ratio in terms of the elastic drift limit ratio, shown in Equation 12.

$$\frac{k_4}{k_2} = \left(\frac{\delta_2}{\delta_4}\right)^2 \tag{12}$$

This result shows that if the elastic drift limit is decreased by a ratio of (δ_2/δ_4), then the stiffness of the design must increase by a factor of $(\delta_2/\delta_4)^2$ to meet the drift limit. This squared amplification of the drift limit ratio is the result of the period effect (as the system is stiffened the design force increases). For the common case where the drift limit for a Risk Category II design is twice that of a Risk Category IV design, the Risk Category IV design will require a stiffness that is four times that of the Risk Category II design.

For reference, a different substitution and rearrangement of Equations 11 and 7 gives the relationship between the design base shears for the two systems, shown in Equation 13.

$$\frac{V_4}{V_2} = \frac{\delta_2}{\delta_4} \tag{13}$$

Derivation of Strength Ratio

The following derivation is for a single-degree-of-freedom system on the descending branch of the design spectra. Later sections will discuss the result in the context of multi-degree-of-freedom systems. The derivation shows the relationship between the required strength for Risk Category II and Risk Category IV systems when the designs are strength-governed and based on the actual building period.

Figure 3 defines the terms used in the derivation. The points on the spectra represent two designs. The Risk Category II design has a design base shear, V_2, and a period, T_2. The Risk Category IV design has a design base shear, V_4, and a period, T_4. The Risk Category IV design is on the upper curve corresponding to the 1.5 importance factor.

Equations 14 and 15 relate the base shears and periods, according to the respective spectra.

$$V_2 = \frac{S_{D1}}{T_2\left(\frac{R}{1.0}\right)}W \tag{14}$$

$$V_4 = \frac{S_{D1}}{T_4\left(\frac{R}{1.5}\right)}W \tag{15}$$

Combining Equations 14 and 15 and rearranging relates the periods and base shears of the Risk Category II and IV systems to each other, shown in Equation 16.

$$V_4T_4 = 1.5V_2T_2 \tag{16}$$

Rearranging Equation 16 gives:

$$\left(\frac{T_4}{T_2}\right)^2 = 1.5^2\left(\frac{V_2}{V_4}\right)^2 \tag{17}$$

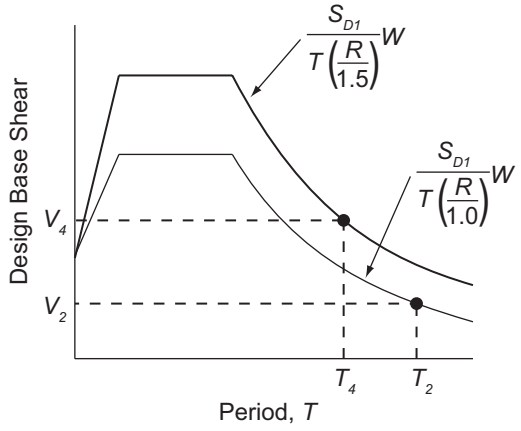

Fig. 3. Terms used for strength ratio derivation for strength-governed system.

The natural periods for the SDOF systems are:

$$T_2 = 2\pi\sqrt{\frac{m}{k_2}} \tag{18}$$

$$T_4 = 2\pi\sqrt{\frac{m}{k_4}} \tag{19}$$

where m is the mass (the same for both systems), and k_2 and k_4 are the respective stiffnesses.

Combining Equations 18 and 19 and rearranging terms gives Equation 20.

$$\left(\frac{T_4}{T_2}\right)^2 = \frac{k_2}{k_4} \tag{20}$$

Combining Equations 20 and 17 results in Equation 21.

$$\frac{k_2}{k_4} = 1.5^2\left(\frac{V_2}{V_4}\right)^2 \tag{21}$$

Assuming that the strength and stiffness ratios of the systems are similar results in Equation 22.

$$\frac{k_2}{k_4} \approx \frac{V_2}{V_4} \tag{22}$$

Combining Equations 22 and 21 gives the result shown in Equation 23.

$$\frac{V_4}{V_2} \approx 1.5^2 \approx 2.25 \tag{23}$$

This shows that using an importance factor of 1.5 to increase strength demands results in Risk Category IV designs that can be about 2.25 times stronger than a Risk Category II design. The squared amplification of the importance factor is the result of the period effect (as the system is strengthened the force demands increase).

The result in Equation 23 is based on the assumption that the actual building period is being used in determining the design base shear. For strength-governed design, the design period is limited to C_uT_a (ASCE, 2016), which affects the validity of Equation 22. As such, Equation 22 should be viewed as an upper bound. If C_uT_a governed the design period for the Risk Category II design, then the strength ratio would be lower. If C_uT_a governed the design period for both the Risk Category II and Risk Category IV design, then the required strength ratio would simply be 1.5 because there would be no period effect.

As a final consideration, for some strength-governed systems, the elastic overstrength of a Risk Category II design approaches 1.5 so that even if the design base shear were 1.5 times greater, the structural design could remain mostly unchanged for a Risk Category IV design. This is not pertinent for steel SMF design but will be discussed for broader applications. For example, in a Risk Category II steel braced

Table 2. Cost Estimates for Stiffness-Governed Risk IV Design Scenarios					
Scenario	**Example**	**Stiffness Ratio (IV/II)**	W_{SMF}/W_t[a]	$W_{t,IV}/W_{t,II}$[b]	**Cost Index**[c]
Upper bound	Over four stories and high percentage of lateral frame weight	4.0	0.60	2.08	1.22
Middle	Over four stories	4.0	0.40	1.72	1.14
Lower bound	Under four stories	2.78	0.35	1.33	1.07

[a] This is the assumed ratio of the weight of the SMF steel to the total steel weight.
[b] This ratio was estimated as: $(1 - W_{SMF}/W_t) + (W_{SMF}/W_t)$(Stiffness ratio)(0.7). The 0.7 is a multiplier that accounts for higher efficiency in the Risk IV frame due to more efficient shapes and was based on previous design experience.
[c] See Equation 1.

Table 3. Cost Estimates for Strength-Governed Risk IV Design Scenarios					
Scenario	**Example**	**Strength Ratio (IV/II)**	W_{SMF}/W_t[a]	$W_{t,IV}/W_{t,II}$[b]	**Cost Index**[c]
Upper bound	Actual building periods used for designs	2.25	0.40	1.5	1.10
Middle	C_uT_a used for designs	1.5	0.30	1.15	1.03
Lower bound	C_uT_a used for designs and natural elastic overstrength	1.2	0.20	1.04	1.01

[a] This is the assumed ratio of the weight of the SMF steel to the total steel weight.
[b] This ratio was estimated as: $(1 - W_{SMF}/W_t) + (W_{SMF}/W_t)$(Stiffness ratio).
[c] See Equation 1.

frame, the braces may be oversized to meet width-thickness requirements, and the same frame may be almost adequate for the Risk Category IV design. For some systems, then, the actual IV/II strength ratio will be less than even 1.5. For discussion purposes, we will pick 1.2 as an estimated lower bound.

Cost Premiums for Drift-Governed Designs (Mathematical Bounds)

For stiffness governed designs, the stiffness ratio is estimated from Equation 12. The upper-bound stiffness ratio for buildings four stories or less is $(2.5/1.5)^2 = 2.78$. For buildings greater than four stories, it is $(2.0/1.0)^2 = 4.0$. Table 2 shows cost estimates for upper-bound, lower-bound, and middle cases based on this range of possible stiffness ratios (IV/II), assumptions about the SMF weight relative to the total steel weight, W_{SMF}/W_t, and estimates of corresponding weight ratios, $W_{t,IV}/W_{t,II}$.

Table 2 indicates a range of cost premiums for stiffness-governed designs of 1.07 to 1.22. Because the cost premiums in Table 2 are based on estimates for $W_{t,IV}/W_{t,II}$, they are less reliable than those obtained from the case studies, which will be discussed later.

Cost Premiums for Strength-Governed Designs (Mathematical Bounds)

For strength-governed designs, the expected strength ratio based on the mathematical derivation ranged from about 1.2 to 2.25. Table 3 shows cost estimates for upper-bound, lower-bound, and middle cases, based on this range of possible strength ratios (IV/II), assumptions about the SMF weight relative to the total steel weight, W_{SMF}/W_t, and estimates of corresponding weight ratios, $W_{t,IV}/W_{t,II}$.

The cost index values in Table 3 indicate a range of cost premiums from 1 to 10% for strength-governed designs. The lower-bound premium of about 1% is consistent with the strength-governed studies previously cited (NIST, 2013; Yu et al., 2015). The characteristics of buildings that will be near the lower-bound premium are as follows:

- Design is strength-governed.
- C_uT_a is used for the design period.
- There is some elastic overstrength.
- The weight of the lateral force-resisting system is a small percentage of the total structural weight.

Table 4. Summary of Stiffness Results from the Case Study Buildings				
	Stiffness			
Stories	II (kips/rad)[a]	IV (kips/rad)[a]	IV/II	Equation 12 Stiffness Ratio
2	83476	194515	2.33	2.78
4	82884	197741	2.39	2.78
6	129247	459756	3.56	4.00
8	137112	471614	3.44	4.00
12	76406	232186	3.04	4.00
16	123299	247306	2.01	4.00

[a] Because the Risk Category II and Risk Category IV designs have slightly different building heights (Table 1), the stiffness is defined as lateral force over drift ratio, so that the IV/II ratio will not be distorted by the varying heights.

Many buildings have these characteristics and would have Risk Category IV cost premiums around 1 to 2%, but steel SMF generally do not have these characteristics. The results from the mathematical derivations demonstrate how drift-governed buildings can have a much greater construction cost premium for Risk Category IV design than strength-governed buildings.

RESULTS FROM CASE STUDY BUILDINGS

This second part of the results focuses on the case study buildings and has four subsections. The first subsection presents results on the stiffness of the case study buildings and discusses them relative to Equation 12. The second subsection discusses the strength of the case study buildings. The third subsection presents the weights and weight ratios for the case study buildings. The final subsection presents the cost premiums calculated for case study buildings and discusses them in the context of the theoretical ranges established in the previous sections.

Stiffness of Case Study Buildings

The elastic stiffness of each of the case study buildings (lateral force/roof drift) was obtained from the corresponding RAM model. Table 4 summarizes the stiffness results, including IV/II stiffness ratios. Also shown in the Table 4 is the upper-bound stiffness ratio from Equation 12, which differs depending on the ratio of the allowable drifts (different for buildings four stories and less).

The stiffness ratios from the case study buildings were lower than those from Equation 12. For the 2- and 4-story buildings, the stiffness ratios (IV/II) were 14 to 16% less than those from Equation 12 (Table 4). For the 6- and 8-story buildings, the case study stiffness ratios were 11 to 14% less than those from Equation 12, with the best match for the six-story buildings. For the 12- and 16-story buildings, the designs were not governed by the equations assumed in the derivation of Equation 12 (they were governed by minimum base shear equations, Table 1), so the stiffness ratios were farther from Equation 12.

The case study values of the stiffness ratio are valuable for understanding the stiffness ratios of as-designed buildings, while Equation 12 (the derivation) is helpful for understanding why the stiffness ratio is substantially higher than the ratio of the drift limits for designs on the descending branch of the design spectra. The case studies confirm that Risk Category IV SMF buildings on the descending branch of the design spectra can approach four times the stiffness of Risk Category II SMF buildings.

Strength of Case Study Buildings

The strengths, V_y, of the case study buildings are summarized in Table 5, including the IV/II strength ratios. Strength ratios for the case study SMF buildings (Table 5) were often higher than the range that was developed for strength-governed systems (Table 2) because most of the case study buildings were drift-governed. For the 6- to 12-story buildings, the IV/II strength ratios exceeded 3.0 (Table 5). This observation has implications for foundation design and may be surprising for designers that expect a Risk Category IV building to only be 1.5 to 2.0 times stronger than a Risk Category II building.

Weight of Case Study Buildings

The weight of each case study building was obtained from the RAM takeoffs. Table 6 summarizes the weight results for the individual buildings as well as various IV/II weight ratios. Figures 4 and 5 illustrate some relationships of interest.

Figure 4 shows the steel weights (gravity, SMF, and total) for the different buildings, expressed in pounds per square foot (psf). The gravity steel weights were similar for all the buildings (around 3 psf, a little higher for the taller

Table 5. Summary of Strength Results from the Case Study Buildings							
	Seismic Weight, W (kips)		Strength, V_y			V_y/W	
Stories	II	IV	II (kips)	IV (kips)	IV/II	II	IV
2	3506	3583	653	1597	2.45	0.19	0.45
4	7084	7293	741	1586	2.14	0.10	0.22
6	10849	11470	1059	3374	3.18	0.10	0.29
8	14466	15432	1015	3206	3.16	0.07	0.21
12	10847	11451	568	1721	3.03	0.05	0.15
16	14736	15696	989	1730	1.75	0.07	0.11

Table 6. Weight Summaries for the Case Study Buildings										
	SMF Steel Weight, W_{SMF}			Gravity Steel Weight, W_{grav} (psf)		Total Steel Weight, W_t			W_{SMF}/W_t	
Stories	II (psf)	IV (psf)	IV/II	II	IV	II (psf)	IV (psf)	IV/II	II	IV
2	1.75	3.31	1.89	3.08	3.10	4.83	6.40	1.32	0.36	0.52
4	2.17	3.74	1.72	3.35	3.59	5.52	7.33	1.33	0.39	0.51
6	3.43	8.15	2.37	3.44	3.35	6.87	11.5	1.67	0.50	0.71
8	3.40	8.72	2.56	3.44	3.46	6.84	12.2	1.78	0.50	0.72
12	4.96	8.91	1.79	3.68	3.74	8.65	12.6	1.46	0.57	0.70
16	6.44	11.3	1.76	3.85	3.97	10.3	15.3	1.49	0.63	0.74

buildings). For the 2- and 4-story Risk Category II buildings [Figure 4(a)], the SMF steel weight was less than the gravity, but for other buildings, SMF steel weight was greater than the gravity. Figure 4(b) shows that for the 6-story and taller Risk Category IV buildings, the SMF weight was several times the gravity steel weight.

The "jumps" in SMF weight in Figure 4(b) between the 4- and 6-story designs and between the 12- and 16-story designs were due to changes in the design criteria. The allowable drifts were different for the 4-story-and-under designs [ASCE/SEI 7, Table 12.12-1 (ASCE, 2016)], which explained the weight jump at 6 stories. The 16-story

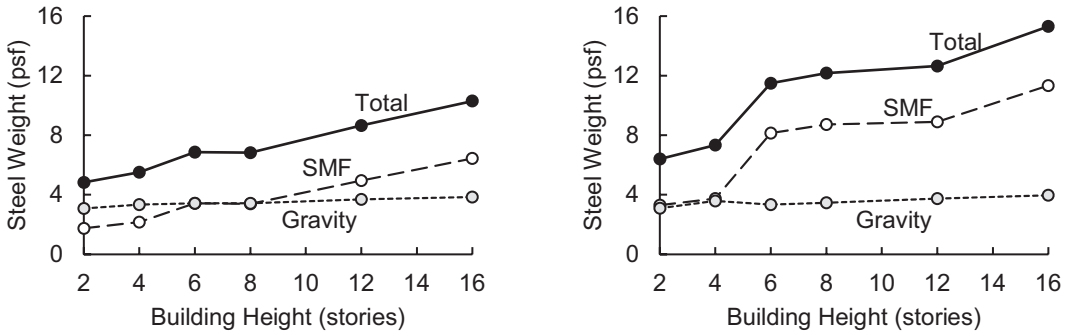

(a) Risk Category II designs *(b) Risk Category IV designs*

Fig. 4. Steel weights for the case study buildings.

Table 7. Cost Index for Case Study Buildings		
Stories	$W_{t,IV}/W_{t,II}$	Cost Index
2	1.32	1.06
4	1.33	1.07
6	1.67	1.13
8	1.78	1.16
12	1.46	1.09
16	1.49	1.10

buildings had higher $C_s/C_{s,drift}$ ratios in design than the 12-story buildings (Table 1), making the 16-story buildings more strength-controlled.

Figure 5 shows two weight ratios (total and SMF) along with two other IV/II ratios of interest from the study. The SMF weight ratio (long dash) is as high as 2.6, indicating the substantial increase in SMF steel required for Risk Category IV designs on the descending branch of the spectra. The total weight ratio is lower, with a maximum of 1.7, because the relatively constant gravity steel dilutes the SMF steel increase. The total weight ratio in Figure 5 is of particular interest since it is the parameter in the cost index (Equation 1). Figure 5 shows that the total steel weight ratio increases for buildings over 4 stories, peaks around 8 stories, and decreases for taller buildings when minimum base shear equations start to govern both the Risk Category II and IV designs.

The SMF weight ratios were 12 to 40% lower than the stiffness ratios (comparing dashed lines Figure 5), reflecting better lateral weight efficiency for the Risk Category IV buildings. The primary source of that efficiency was the deeper heavier beams. For example, the 8-story Category Risk Category II buildings used W27×94 beams at the bottom (because they were sufficient) while the Risk Category IV buildings used W36×231. One measure of stiffness efficiency of a flexural member is I/w, where I is the moment of inertia and w is the weight in pounds per foot. For a W36×231, I/w was 68 in.^{4}/lb, whereas for a W27×94, I/w was 35 in.^{4}/lb. The more efficient sections in the Risk Category IV buildings allowed the SMF weight increase to be less than the stiffness increase.

Also note in Figure 5 that the stiffness and strength IV/II ratios track each other quite closely. This was expected for the steel buildings, where both strength and stiffness were directly related to the cross-sectional properties of the steel members.

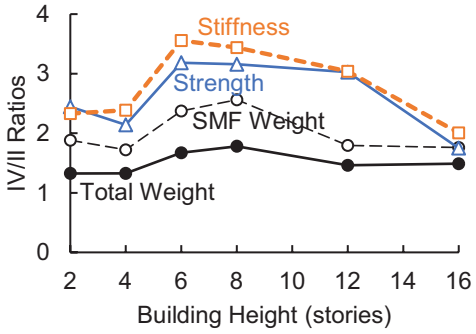

Fig. 5. Various ratios comparing the Risk Category IV and II buildings.

Cost Premium of Case Study Buildings

The total weight ratio, $W_{t,IV}/W_{t,II}$, was used with Equation 1 to determine cost premiums for the case study buildings. Table 7 repeats the IV/II weight ratio from Table 6 and shows the associated cost index. Table 7 indicates a range of 1.07 to 1.17 for the cost index, which corresponds to cost premiums of 7 to 17% for the Risk IV SMF buildings. The premiums increased for buildings over 4 stories, peaked at 8 stories, and decreased for taller buildings when minimum base shear equations start to govern both the Risk Category II and IV designs.

The 6 to 16% cost premium range for the SMF buildings in this study was a little higher than the 4 to 14% range mentioned in Richards et al. (2023). The shift was due to the following differences in the SMF design criteria of the two studies:

- In the previous study, a constant story height of 12 ft was assumed for all the buildings to match the buildings of an earlier study. As a result, the clear-heights varied and were unrealistically low (9 ft) for modern steel buildings. In the present study, a consistent clear-height (at least 12 ft) was used for all the buildings.
- In the previous study, the column depths were different for the Risk Category II (W24) and IV (W27) buildings. In the present study, the column depths were constrained to be the same for all (W27).

- In the previous study, a constant conservative steel weight was assumed for dead loads and seismic weight. In the present study, the actual steel weight based on member sizes was used so the seismic weight was different for the Risk Category II and IV buildings.

All things considered, both studies had similar findings, and the 6 to 16% construction cost premium range from the present study is more accurate for current practice. These cost premiums can be compared with the cost of other alternatives for post-earthquake functional recovery. Other studies have demonstrated much more economical approaches for the functional recovery of steel SMF buildings rather than using Risk Category IV design [see Richards et al. (2023)].

Mitigating Cost Premiums

Even deeper columns may be used to help mitigate construction cost premiums for Risk Category IV design but can only bring prices down a little. In the study buildings, the column depth was kept consistent (W27) for the Risk Category II and IV designs to allow a comparison of architecturally equivalent systems. To investigate the potential savings from deeper columns, an alternative design for the Risk Category IV 8-story building was generated with W33 columns. The member sizes are shown in the Appendix (Table 9). The design with W33 columns saved 7% on the total weight, but the cost index for the Risk Category IV design with W33 columns was still 1.13 (13% total building cost premium as compared to Risk Category II design).

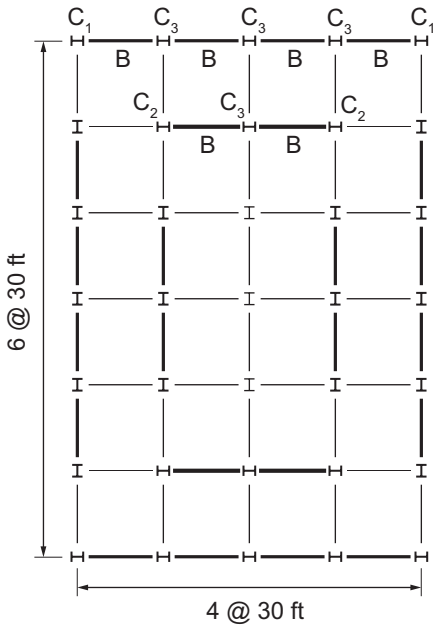

Fig. 6. SMF layout for an alternative design for a Risk Category IV 8-story building that did not reduce overall steel weight.

Adding additional moment frames was not helpful in reducing the construction cost premiums much. To investigate the effect of additional moment frames bays on cost, an alternative design for the Risk Category IV 8-story building was generated with the frame layout shown in Figure 6. The number of moment frame bays in each direction was increased from 8 to 12. The member sizes for this design are shown in the Appendix (Table 10). Adding additional frames was helpful for reducing the weights of individual members (beams and columns) but not for significantly reducing the overall building weight. The total steel weight (beams and columns) for the design with extra frames (11.9 psf) was 2% less than the baseline Risk Category IV design (Table 6), but the added moment connections would increase fabrication and erection costs, and the W27 columns in the interior spaces would be architecturally intrusive. The observations from this comparison are consistent with another study (McCall and Richards, 2022), and professional practice that generally uses SMF with deep columns on the perimeters and minimizes the number of SMF connections as long as the beam and column sizes are prequalified and architecturally acceptable.

SUMMARY AND CONCLUSIONS

As engineers contemplate the use of Risk Category IV design to address post-earthquake functional recovery, it is helpful to quantify the cost of Risk Category IV design for strength-governed and drift-governed buildings. Limited studies have suggested that cost premiums are higher for drift-governed SMF buildings.

Two complementary methods were used in this study. The first method was to mathematically derive the difference in strength and stiffness for Risk Category II and IV designs, accounting for period effects. Closed-form solutions were possible for single-degree-of-freedom (SDOF) systems. The second method was to use case study buildings to compute cost premiums. Twelve SMF buildings with varying height (2-, 4-, 6-, 8-, 12-, and 16-story) and varying Risk Category (II and IV) were designed. The steel weights from the case study buildings were used with a cost index to estimate the construction cost premiums in terms of total building cost.

Conclusions from the mathematical derivations included the following:

- For drift-governed buildings, the upper bound for the stiffness multiplier for Risk Category IV design was the square of the allowable drift ratio. For buildings over four-stories, it was a factor of four.
- For strength-governed buildings, the upper bound for the required strength multiplier for Risk Category IV design was the square of the importance factor. For an importance factor of 1.5, the upper bound on the strength

Table 8. Case Study SMF Designs									
		Risk Category II				Risk Category IV			
Stories	Story	C1	C2	C3	B	C1	C2	C3	B
2	1	W27×94	—	W27×94	W24×55	W27×217	—	W27×102	W30×108
	2	W27×94	—	W27×94	W21×44	W27×217	—	W27×102	W27×94
4	1	W27×114	—	W27×114	W24×76	W27×258	—	W27×146	W33×130
	2	W27×114	—	W27×114	W24×76	W27×258	—	W27×146	W33×130
	3	W27×94	—	W27×94	W24×62	W27×217	—	W27×114	W30×108
	4	W27×94	—	W27×94	W21×44	W27×217	—	W27×114	W24×62
6	1	W27×178	—	W27×114	W27×94	W27×539	—	W27×235	W36×194
	2	W27×178	—	W27×114	W27×94	W27×539	—	W27×235	W36×182
	3	W27×161	—	W27×114	W24×84	W27×539	—	W27×194	W36×182
	4	W27×161	—	W27×114	W24×84	W27×539	—	W27×194	W36×150
	5	W27×114	—	W27×94	W24×76	W27×307	—	W27×178	W33×130
	6	W27×114	—	W27×94	W18×35	W27×307	—	W27×178	W24×76
8	1	W27×178	—	W27×146	W27×94	W27×539	—	W27×307	W36×231
	2	W27×178	—	W27×146	W27×94	W27×539	—	W27×307	W36×231
	3	W27×161	—	W27×114	W27×94	W27×539	—	W27×235	W36×194
	4	W27×161	—	W27×114	W27×94	W27×539	—	W27×235	W36×170
	5	W27×129	—	W27×114	W24×76	W27×539	—	W27×178	W36×160
	6	W27×129	—	W27×114	W24×76	W27×539	—	W27×178	W33×141
	7	W27×94	—	W27×94	W24×55	W27×281	—	W27×161	W33×141
	8	W27×94	—	W27×94	W18×40	W27×281	—	W27×161	W24×84

multiplier was 2.25. This upper bound would rarely be reached in practice because of the C_uT_a limit on the design period.

Conclusions from the case study buildings included the following:

- Risk Category IV SMF buildings had 2.0 to 3.6 times the stiffness of Risk Category II buildings. The stiffness ratios for buildings on the descending branch of the design spectra were 11 to 16% lower than the upper bound found from the closed-form solution (SDOF).
- Risk Category IV SMF buildings had 1.8 to 3.2 times the strength of Risk Category II buildings.
- Risk Category IV SMF buildings had 1.8 to 2.6 times the SMF weight of Risk II buildings, but when gravity steel weight was included, the Risk Category IV buildings only had 1.3 to 1.9 times the total steel weight.
- The cost premiums for Risk Category IV SMF buildings were 6 to 16% of the total building cost, with the greatest premiums for the eight-story building. These premiums were substantially greater than the 1% cost premiums that have been reported in studies with strength-governed buildings.

Some limitations of the study were that only steel SMF buildings were included in the case studies, and only one SMF connection type was considered. However, results were similar to another SMF study (Richards et al., 2023) that considered three different types of connections.

APPENDIX

The designs for the case study buildings are summarized in Table 8. See Figure 1 for the definitions of the column and beam tags.

Table 8. Case Study SMF Designs (continued)									
		Risk Category II				Risk Category IV			
Stories	Story	C1	C2	C3	B	C1	C2	C3	B
12	1	W27×129	W27×161	W27×146	W24×55	W27×217	W27×281	W27×217	W30×124
	2	W27×129	W27×161	W27×146	W24×55	W27×217	W27×281	W27×217	W30×124
	3	W27×129	W27×146	W27×129	W24×55	W27×194	W27×258	W27×178	W30×116
	4	W27×129	W27×146	W27×129	W24×55	W27×194	W27×258	W27×178	W30×108
	5	W27×129	W27×146	W27×114	W21×50	W27×194	W27×258	W27×146	W30×108
	6	W27×129	W27×146	W27×114	W21×50	W27×194	W27×258	W27×146	W30×108
	7	W27×94	W27×114	W27×102	W21×50	W27×178	W27×194	W27×114	W27×102
	8	W27×94	W27×114	W27×102	W21×44	W27×178	W27×194	W27×114	W27×94
	9	W27×94	W27×94	W27×94	W18×40	W27×161	W27×178	W27×102	W27×94
	10	W27×94	W27×94	W27×94	W18×35	W27×161	W27×178	W27×102	W24×76
	11	W27×94	W27×94	W27×94	W18×35	W27×102	W27×129	W27×194	W24×76
	12	W27×94	W27×94	W27×94	W18×35	W27×102	W27×129	W27×194	W18×40
16	1	W27×146	W27×235	W27×217	W24×84	W27×336	W27×539	W27×307	W33×130
	2	W27×146	W27×235	W27×217	W24×84	W27×336	W27×539	W27×307	W33×130
	3	W27×146	W27×217	W27×217	W24×84	W27×336	W27×368	W27×258	W33×130
	4	W27×146	W27×217	W27×217	W24×84	W27×336	W27×368	W27×258	W30×116
	5	W27×146	W27×194	W27×161	W24×84	W27×307	W27×307	W27×235	W30×116
	6	W27×146	W27×194	W27×161	W24×76	W27×307	W27×307	W27×235	W30×116
	7	W27×129	W27×178	W27×146	W24×76	W27×258	W27×281	W27×161	W30×108
	8	W27×129	W27×178	W27×146	W24×76	W27×258	W27×281	W27×161	W30×108
	9	W27×129	W27×161	W27×129	W24×76	W27×258	W27×258	W27×146	W30×108
	10	W27×129	W27×161	W27×129	W24×62	W27×258	W27×258	W27×146	W27×102
	11	W27×94	W27×114	W27×114	W24×62	W27×235	W27×235	W27×114	W27×102
	12	W27×94	W27×114	W27×114	W24×55	W27×235	W27×235	W27×114	W27×94
	13	W27×94	W27×102	W27×102	W24×55	W27×194	W27×194	W27×114	W27×94
	14	W27×94	W27×102	W27×102	W21×44	W27×194	W27×194	W27×114	W24×76
	15	W27×94	W27×94	W27×94	W18×35	W27×161	W27×161	W27×94	W24×55
	16	W27×94	W27×94	W27×94	W18×35	W27×161	W27×161	W27×94	W18×35

Table 9. Eight-Story Comparison Design with Deeper Columns									
		Risk Category II				Risk Category IV			
Stories	Story	C1	C2	C3	B	C1	C2	C3	B
8	1	W27×178	—	W27×146	W27×94	W33×263	—	W33×387	W36×232
	2	W27×178	—	W27×146	W27×94	W33×263	—	W33×387	W36×232
	3	W27×161	—	W27×114	W27×94	W33×263	—	W33×354	W36×194
	4	W27×161	—	W27×114	W27×94	W33×263	—	W33×354	W36×194
	5	W27×129	—	W27×114	W24×76	W33×221	—	W33×354	W36×160
	6	W27×129	—	W27×114	W24×76	W33×221	—	W33×354	W36×150
	7	W27×94	—	W27×94	W24×55	W33×169	—	W33×354	W36×150
	8	W27×94	—	W27×94	W18×40	W33×169	—	W33×354	W21×44

Table 10. Eight-Story Comparison Design with Additional Moment Frames									
Stories	Story	Risk Category II				Risk Category IV			
		C1	C2	C3	B	C1	C2	C3	B
8	1	W27×178	—	W27×146	W27×94	W27×217	W27×235	W27×368	W36×160
	2	W27×178	—	W27×146	W27×94	W27×217	W27×235	W27×368	W36×160
	3	W27×161	—	W27×114	W27×94	W27×194	W27×194	W27×368	W36×150
	4	W27×161	—	W27×114	W27×94	W27×194	W27×194	W27×368	W36×150
	5	W27×129	—	W27×114	W24×76	W27×161	W27×146	W27×258	W33×141
	6	W27×129	—	W27×114	W24×76	W27×161	W27×146	W27×258	W33×130
	7	W27×94	—	W27×94	W24×55	W27×102	W27×102	W27×194	W30×116
	8	W27×94	—	W27×94	W18×40	W27×102	W27×102	W27×194	W24×55

REFERENCES

AISC (2016a), *Prequalified Connections for Special and Intermediate Steel Moment Frames for Seismic Applications*, ANSI/AISC 358-16, American Institute of Steel Construction, Chicago, Ill.

AISC (2016b), *Seismic Provisions for Structural Steel Buildings*, ANSI/AISC 341-16, American Institute of Steel Construction, Chicago, Ill.

ASCE (2010), *Minimum Design Loads for Buildings and Other Structures*, ASCE/SEI 7-10, American Society of Civil Engineers, Reston, Va.

ASCE (2016), *Minimum Design Loads and Associated Criteria for Buildings and Other Structures*, ASCE/SEI 7-16, American Society of Civil Engineers, Reston, Va.

Bentley (2021), RAM Frame Users Manual, Version 19.

Erochko, J., Christopoulos, C., Tremblay, R., and Choi, H. (2011), "Residual Drift Response of SMRFs and BRB Frames in Steel Buildings Designed According to ASCE 7-05," *Journal of Structural Engineering*, Vol. 137, No. 5, pp. 589–599.

Harris, J. and Speicher, M. (2018), "Assessment of Performance-Based Seismic Design Methods in ASCE 41 for New Steel Buildings: Special Moment Frames," *Earthquake Spectra*, Vol. 34, No. 3, pp. 977–999.

ICC (2003), *International Building Code*, International Code Council, Falls Church, Va.

ICC (2012), *International Building Code*, International Code Council, Falls Church, Va.

ICC (2021), *International Building Code*, International Code Council, Falls Church, Va.

McCall, A.J. and Richards, P.W. (2022), "Using Genetic Algorithms to Optimize Steel Special Moment Frames," 12th National Conference on Earthquake Engineering, Earthquake Engineering Research Institute, Salt Lake City, Utah.

NIST (2013), "Cost Analyses and Benefit Studies for Earthquake-Resistant Construction in Memphis Tennesee," NIST GCR 14-917-26, National Institute of Standards and Technology, Gaithersburg, Md.

NIST (2021), "Recommended Options for Improving the Built Environment for Post-Earthquake Reoccupancy and Functional Recovery Time," National Institute of Standards and Technology, Gaithersburgh, Md.

Richards, P.W., McCall, A.J., and Marshall, J.D. (2023), "Functional Recovery of Steel Special Moment Frames," *Journal of Structural Engineering*, Vol. 149, No. 3, 0402261.

Yu, K., Newell, J., Beyer, D., Poland, C., and Raskin, J. (2015), "Beaverton School District Resilience Planning for High School at South Cooper Mountain and Middle School at Timberland," SEFT Consulting Group, Beaverton, Ore.

Guide for Authors

Scope

Engineering Journal is dedicated to the improvement and advancement of steel construction. Its pages are open to all who wish to report on new developments or techniques in steel design, research, the design and/or construction of new projects, steel fabrication methods, or new products of significance to the uses of steel in construction. Only original papers should be submitted.

General

Papers intended for publication should be submitted by email Margaret Matthew, editor, at **matthew@aisc.org**.

The articles published in the *Engineering Journal* undergo peer review before publication for (1) originality of contribution; (2) technical value to the steel construction community; (3) proper credit to others working in the same area; (4) prior publication of the material; and (5) justification of the conclusion based on the report.

All papers within the scope outlined above will be reviewed by engineers selected from among AISC, industry, design firms, and universities. The standard review process includes outside review by an average of three reviewers, who are experts in their respective technical area, and volunteers in the program. Papers not accepted will not be returned to the author. Published papers become the property of the American Institute of Steel Construction and are protected by appropriate copyrights. No proofs will be sent to authors.

Manuscripts

Manuscripts must be provided in Microsoft Word format. Include a PDF with your submittal so we may verify fonts, equations and figures. View our complete author guidelines at **aisc.org/ej**.

Smarter. Stronger. Steel.

American Institute of Steel Construction
130 E Randolph St, Ste 2000, Chicago, IL 60601
312.670.2400 | aisc.org/ej